

AD-A148 435

MANUFACTURING METHODS FOR THE PRODUCTION OF FIELD  
EFFECT ELECTRON EMITTERS FROM OXIDE-METAL COMPOSITES  
(U) GEORGIA INST OF TECH ATLANTA A T CHAPMAN DEC 77

1/3

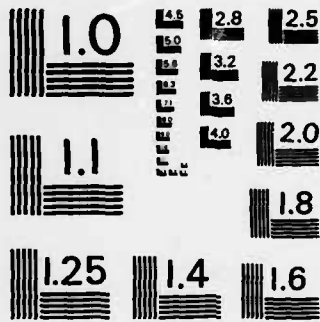
UNCLASSIFIED

DAAH01-75-C-0852

F/G 9/1

NL





MICROCOPY RESOLUTION TEST CHART  
NATIONAL BUREAU OF STANDARDS-1963-A

AD-A148 435

2

MANUFACTURING METHODS FOR THE PRODUCTION OF  
FIELD EFFECT ELECTRON EMITTERS FROM  
OXIDE-METAL COMPOSITES

FINAL TECHNICAL REPORT

(Period: 16 May 1975 - 15 November 1977)

from

THE SCHOOLS OF CERAMIC AND ELECTRICAL ENGINEERING  
GEORGIA INSTITUTE OF TECHNOLOGY

PROJECT DIRECTOR: A.T. CHAPMAN

December 1977

Sponsored by:

U.S. ARMY MISSILE COMMAND  
REDSTONE ARSENAL, AL 35809

CONTRACT NUMBER : DAAH01-75-C-0852

Distribution of this document is unlimited.

DISTRIBUTION STATEMENT A  
Approved for public release  
Distribution Unlimited

DTIC  
FLECTE  
DEC 11 1984  
B

84 11 29 040

DTIC FILE COPY

Unclassified

SECURITY CLASSIFICATION OF THIS PAGE (When Data Entered)

REPORT DOCUMENTATION PAGE		READ INSTRUCTIONS BEFORE COMPLETING FORM	
1. REPORT NUMBER Final Technical Report MM&T Project 3753134	2. GOVT ACCESSION NO. AD-A148435	3. RECIPIENT'S CATALOG NUMBER	
4. TITLE (and Subtitle) Manufacturing Methods for the Production of Field Effect Electron Emitters from Oxide-Metal Composites		5. TYPE OF REPORT & PERIOD COVERED Final Report for 16 May 1975-15 Nov. 1977	
		6. PERFORMING ORG. REPORT NUMBER	
7. AUTHOR(s) A.T. Chapman, J.K. Cochran R.K. Feeney, and D.N. Hill		8. CONTRACT OR GRANT NUMBER(s) DAAH01-75-C-0852	
9. PERFORMING ORGANIZATION NAME AND ADDRESS Georgia Institute of Technology Schools of Ceramic and Electrical Engineering Atlanta, GA 30332		10. PROGRAM ELEMENT, PROJECT, TASK AREA & WORK UNIT NUMBERS	
11. CONTROLLING OFFICE NAME AND ADDRESS		12. REPORT DATE December 1977	
		13. NUMBER OF PAGES 232	
14. MONITORING AGENCY NAME & ADDRESS (if different from Controlling Office) U.S. Army Missile Research and Development Command Redstone Arsenal, Alabama 35809		15. SECURITY CLASS. (of this report)  Unclassified	
		15a. DECLASSIFICATION DOWNGRADING SCHEDULE	
16. DISTRIBUTION STATEMENT (of this Report)  Approved for public release; distribution unlimited.			
17. DISTRIBUTION STATEMENT (of the abstract entered in Block 20, if different from Report)  Distribution unlimited			
18. SUPPLEMENTARY NOTES  1,000,000      50,000,000			
19. KEY WORDS (Continue on reverse side if necessary and identify by block number) Oxide-metal Composites, Field Emission, Tungsten Pin Arrays, Unidirectional Solidification of UO <sub>2</sub> -W, Field Effect Electron Emitters, Cold Cathodes, Internal Zone Melting, Oxide-Metal Eutectic Structures  59. CM      Micrometer			
20. ABSTRACT (Continue on reverse side if necessary and identify by block number) This report describes the procedures for the routine growth and fabrication of production quantities of field emitters from oxide-metal composites grown by unidirectional solidification. The composites consist of 10 <sup>6</sup> to 5 x 10 <sup>7</sup> ordered 0.5 μm diameter tungsten fibers per cm <sup>2</sup> aligned in an UO <sub>2</sub> matrix. Urania powders from four vendors were characterized according to initial O/U ratio, sinterability, and applicability for growth of well ordered			

Sqcm

SECURITY CLASSIFICATION OF THIS PAGE(When Data Entered)

20. Abstract (continued)

composites. Parameters controlling successful growth of the UO<sub>2</sub>-W composites were investigated and optimized for solidifying ingots weighing up to 500 grams. To fabricate these materials into cathodes, machining, brazing, and chemical etching techniques were developed with compatible thermal expansion characteristics being a major consideration. Lastly, the field emission performance of a variety of prototype emitters were tested and current densities of over 1 A/cm<sup>2</sup> were obtained. Mechanisms leading to pin failures during emission were analyzed.

DTIC  
ELECTE  
S DEC 11 1984 J  
B



Accession For	
NTIS GRA&I	<input checked="" type="checkbox"/>
DTIC TAB	<input type="checkbox"/>
Unannounced	<input type="checkbox"/>
Justification	
By	
Distribution/	
Availability Codes	
Dist	Avall and/or Special
A-1	

## FOREWORD

The Schools of Ceramic and Electrical Engineering of the Georgia Institute of Technology, Atlanta, Georgia, prepared this report on the Manufacturing Methods for the Production of Field Effect Electron Emitters from Oxide-Metal Composites under contract number DAAH01-75-C-0852. This report is the final technical report for the MM&T project 3753134.

The program was sponsored by the U.S. Army Missile Research and Development Command, Redstone Arsenal, Alabama. Dr. A.T. Chapman was the project director with co-principle investigators J.K. Cochran, R.K. Feeney, and D.N. Hill.

Approved for Public Release; Distribution Unlimited

Disposition Instructions: Destroy this document when it is no longer needed. Do not return it to originator.

Disclaimer: The findings in this report are not to be construed as an official Department of the Army position unless so designated by other authorized documents.

Trade Names: Use of trade names or manufacturers names in this report does not constitute an official endorsement or approval of the use of such commercial hardware or software.

PERSONNEL PARTICIPATING IN PROJECT

Principal Investigators

A.T. Chapman

J.K. Cochran

R.K. Feeney

Graduate Students

R.B. Barkalow

S. Frasier

D.N. Hill

W.L. Ohlinger

L. Prosser

M.D. Watson

## TABLE OF CONTENTS

<u>Section</u>	<u>Title</u>	<u>Page</u>
I	INTRODUCTION	1
	A. Procurement and Characterization of Urania Tungsten Powders	4
	B. The Development of Optimum Composite Growth Procedures	5
	C. The Development of Machining, Brazing, and Etching Techniques for the Production of Field Effect Electron Emitters	5
	D. Evaluation of Field Emission Performance of Prototype Emitters	5
II	PROCUREMENT AND CHARACTERIZATION OF UO <sub>2</sub> AND W POWDERS	7
	A. Determination of the Oxygen-To-Uranium (O/U) Ratio	9
	B. Storage of "As-Received" Powders	11
	C. Moisture Content	13
	D. Oxidation Properties	14
	E. Sintering Properties	16
	F. Particle Size Measurement	16
	G. Spectrographic Analysis	18
	H. Summary of Urania Powder Characteristics	18
III	DEVELOPMENT OF OPTIMUM COMPOSITE GROWTH PROCEDURES	21
	A. Sample Size and Fiber Array Uniformity	23
	B. Oxide-Metal Composition	29
	C. Solidification Atmosphere	30
	D. Pre-Melt Ingot Stoichiometry and Density	31
	E. Solidification Rate	44
	F. Molten Zone Control	49
	G. Cracking Characteristics	56
	H. Summary of Composite Growth Procedures	59

TABLE OF CONTENTS (continued)

<u>Section</u>	<u>Title</u>	<u>Page</u>
IV	MACHINING, BRAZING, AND ETCHING TECHNIQUES FOR EMITTERS	65
A.	Machining	65
B.	Brazing	68
1.	Braze Materials	69
2.	Substrate Materials	72
3.	Braze-Substrate Combinations	75
3.1	Copper-Titanium	75
3.2	Copper-Vanadium and Nickel-Vanadium	78
3.3	Nickel-Al <sub>2</sub> O <sub>3</sub>	79
3.4	Nickel-Tungsten	81
3.5	Copper-410 Stainless Steel	85
C.	Etching	87
1.	Chemical Etching	87
2.	Thermal Annealing	88
3.	Ion Milling	91
V	TESTING OF PROTOTYPE FIELD EMISSION CATHODES	97
A.	Background Theory	98
1.	Single Pin Geometry	100
2.	Multi-Pin Emitters	104
B.	Test Fixtures and Cathode Installation Procedures	106
1.	Water-Cooled, Fixed-Spacing Diode	106
2.	Semicon Vacuum Tube	109
3.	RCA Electron Gun	111
4.	Vacuum Systems	114
5.	Electronics	119
C.	Cathode Activation	124
D.	Collection and Analysis of V-I Data	126
E.	Tests with the Uniform Field Anode	129
F.	Analysis of UF Anode Test Results	163
1.	Pin Tip Shape	167
2.	Pin Height	167
3.	Array Density	168
4.	Interelectrode Spacing	169
5.	Platinum Coating	170
G.	Tests of Stylus-Shaped Cathodes	171
1.	Diode Geometry	172
2.	Gun Geometry	181
H.	Tests in the Semicon Vacuum Tube	193
I.	Pin Failure Mechanism	199
VI	SUMMARY	205

TABLE OF CONTENTS (continued)

	<u>Title</u>	<u>Page</u>
APPENDIX A		213
REFERENCES		217

LIST OF ILLUSTRATIONS

<u>Figure</u>	<u>Title</u>	<u>Page</u>
I-1	Diagram of the Induction Heating Facilities Showing the Position of the Molybdenum Susceptor When Used as a Preheater	3
II-1	Oxidation of $UO_{2+x}$ Samples at $80^{\circ}C$	15
III-1	Transverse Sections of 16, 25, and 32, Millimeter Diameter $UO_2$ -W Samples	24
2	Uniform Tungsten Fiber Geometry in $UO_2$ -W Composite, SEM X500	27
3	Photomicrograph of $UO_2$ -W Sample Sintered in a Reducing Atmosphere ( $H_2/N_2$ ) Showing Elemental Metal and Orientated Oxide Grains X196	34
4	Post-Run Longitudinal Section of $UO_2$ -W Sample Sintered in a Reducing Atmosphere, (LBH-16)	35
5	Sample Pellet Sintered in a Neutral Atmosphere ( $N_2$ ) Showing Rounded Metal Particles Surrounded by "Blue Phase", X542	36
6	Sample Pellet Sintered in an Oxidizing Atmosphere ( $CO_2$ ) Showing Extreme Porosity, X196	38
7	Sample LBH-19 After Growth Run Showing Area of Good Growth at Top of Solidified Zone	39
8	Post-Run Longitudinal Section of LBH-5 Showing the Irregular Unstable Molten Zone	41
9	Sample LBH-8B, Showing Double Void	43
10	Photomicrograph of Transverse Section of Sample LBH-20 Showing Tungsten Fiber Array, X542	47

LIST OF ILLUSTRATIONS

<u>Figure</u>	<u>Title</u>	<u>Page</u>
III-11	Transverse Section of (a) Sample LBH-21, Showing High Degree of Uniformity and Extremely Low Fiber Density ( $1.6 \times 10^6$ pins/cm <sup>2</sup> ), and (b) Sample LBH-10A for Comparison ( $31 \times 10^6$ pins/cm <sup>2</sup> ), X945	48
12	Longitudinal Sections of (a) LBH-4, and (b) LBH-15A, Showing Variation of Cell Size with Position in Sample	51
13	Typical Area of "Fan-Banding", Apparently Involving the Repeated Nucleation and Extinction of Fiber Growth. Sample LBH-14; Dark field, X542	53
14	Typical Area of "Fan-Banding" From LBH-17 Showing General Improvement in Fiber Lengths, Dark field, X542	55
15	Transverse View of Sample LBH-6, Showing Stress-Relief Gaps and Distorted Solidified Zone	58
16	Sample LBH-21 Showing "Crack-Free" Central Solidified Zone and Part of the Separated "Skin" Material	60
17	Flow Sheet for the Fabrication of UO <sub>2</sub> -W Composites	61
IV-1	Machined UO <sub>2</sub> -W Composite Stylus with 90° Cone Angle and 5 μm Apex Radius, Etched to Expose Tungsten Fibers; (a) X575 and (b) X1200, 90° From Cone Axis.	66
2	Machined UO <sub>2</sub> -W Composite Stylus with 72° Cone Angle and 25 μm Apex Radius, Etched to Expose Tungsten Fibers; (a) X62 and (b) X1200, 90° From Cone Axis.	67
3	Reflected Light Micrographs of (a) Mo-Ni and (b) Ni Sessiles Drops on UO <sub>2</sub> -W Composites Showing 100° and 60° Contact Angles Respectively, X200.	70

LIST OF ILLUSTRATIONS

<u>Figure</u>	<u>Title</u>	<u>Page</u>
IV-4	Reflected Light Micrograph of Ni Braze-UO <sub>2</sub> -W Composite Interface Showing a Continuous Void Free Join, X200.	73
5	Thermal Expansions for Various Candidate Substrate Metals Compared to UO <sub>2</sub> -W Composites	74
6	Comparative Thermal Expansion of Materials for Braze-Substrate Combinations with UO <sub>2</sub> -W Composites	77
7	Reflected Light Micrographs of (a) Al <sub>2</sub> O <sub>3</sub> -Ni Interface and (b) Ni-UO <sub>2</sub> -W Composite Interface, X545.	80
8	UO <sub>2</sub> -W Composite Wafer Brazed to an Al <sub>2</sub> O <sub>3</sub> Substrate with a 0.056 cm Thick Ni Braze, X8.	82
9	Jig Used to Ni Braze Field Emitter to Tungsten Rod	84
10	Scanning Electron Micrograph of Ion Milled Exposed Fibers. (a) 40 $\mu$ A-min, X28,000; (b) 100 $\mu$ A-min, X14,000; and (c) 230 $\mu$ A-min, X28,000.	92
11	Scanning Electron Micrograph of Ion Milled Exposed Fibers. (a) 750 $\mu$ A-min, X29,500; (b) 4250 $\mu$ A-min, X30,000; and (c) 8500 $\mu$ A-min, X16,800.	93
12	Relation Between Increased Fiber Diameter Due to Sputtered Deposits and Relative Thickness of Matrix Removed, for UO <sub>2</sub> -W Composites, Ion Milled with Exposed Fibers.	95
V-1	Example of A Typical Fowler-Nordheim Plot	102
2	Fixed-Spacing Water-Cooled Diode Test Fixture	107

## LIST OF ILLUSTRATIONS

<u>Figure</u>	<u>Title</u>	<u>Page</u>
V-3	Glass Manifold With Semicon Tubes Mounted, Ready for Testing, X0.3	110
4	RCA Gun Mounted on 20 liter/s Vacuum System	112
5	Schematic Diagram of RCA Gun Showing Position of FE Cathode	113
6	Diffusion-Pumped Vacuum System Used in the Tests with the Fixed-Spacing Water-Cooled Diode	115
7	Ion-Pumped Vacuum System Used in Test MM-32.	118
8	Schematic Diagram of CW Test Circuitry	122
9	Schematic Diagram of Pulse Test Circuitry	123
10	Examples of Waveforms Observed in the Pulse Test, MM-31	125
11	Array Current Density Versus Elapsed Time for Test MM-6	131
12	Array Current Density Versus Elapsed Time for Test MM-10	132
13	Diode Voltage Versus Array Current Density for Four Tests, Illustrating the Effect of Anode Heating on Voltage	133
14	Typical Pin Tip Shape on Cathodes MM-3 and MM-4 Prior to Testing. (a) MM-3, X21500, (b) MM-4, X11700	135
15	Typical Pin Tip Shape on Cathodes MM-5 and MM-6 Prior to Testing. (a) MM-5, X22500, (b) MM-6, X1400	136
16	Post-Emission View of the Cathode Used in Test MM-3; Illustrating the Damage Caused by Vacuum Arcs. (a) X70, (b) X610	137

LIST OF ILLUSTRATIONS

<u>Figure</u>	<u>Title</u>	<u>Page</u>
V-17	Post-Emission Appearance of the Cathode Used in Test MM-4, (a) X590, (b) X2400	138
18	Post-Emission Appearance of the Undamaged Pins on Cathode MM-6, X7900	140
19	Typical Area of Pin Damage on Cathode MM-6 Subsequent to Emission Testing, X1600	140
20	Appearance of the Exposed Pins on Cathodes MM-7 and MM-8 Prior to Testing, (a) MM-7, X5200, (b) MM-8, X1200	143
21	Typical View of the "Pothole" Structure After Etching to Expose the Pins, (a) X220, (b) X1060	144
22	Pin Damage on Cathode Observed After Testing MM-10, (a) X500, (b) X400	146
23	View of Cathode After Test MM-10, Showing Outline of Active Emitting Area Under UF Anode	147
24	Appearance of Exposed Pins on Cathode MM-19 Prior to Emission Testing, X3000	149
25	Post-Emission Damage on Cathode MM-19B, Near Center of Active Emitting Area, X1500	151
26	Typical Pin Damage Observed Near Edge of Active Emitting Area on Cathode MM-19B, (a) X6500, (b) X15000	153
27	Exposed Pins of Cathode MM-31 Prior to High-Temperature Anneal, X5000	155
28	Appearance of Tungsten Pins on MM-31 After Annealing in H <sub>2</sub> for 15 Minutes @ 1400°C, (a) X1500, (b) X20000	156
29	Exposed Pins on Cathode MM-32 Prior to Coating with Platinum, (a) X2000, (b) X6000	160

LIST OF ILLUSTRATIONS

<u>Figure</u>	<u>Title</u>	<u>Page</u>
V-30	Pin Tips on Cathode MM-32 After Applications of Platinum Coating, (a) X7000, (b) X50,000	161
31	Appearance of Cathode MM-32 After Emission Testing, (a) Near Center of Emitting Area, X600, (b) Near Edge of Emitting Area, X6500	164
32	View of Exposed Pins at the Tip of the Stylus Cathode Used in Test MM-20, (a) X1500 (b) X11000	174
33	Appearance of Pin Tips on Cathode MM-20 Prior to Emission Testing, (a) Pin c, X20000, (b) Pin a, X66000	175
34	Damage Produced at Tip of Stylus Cathode in Test MM-20 When Pin c was Destroyed by an Arc, (a) X1500, (b) X6000	176
35	Post-Emission Appearance of Anode in Test MM-20, (a) X70, (b) X945	178
36	View of the Exposed Pin at the Tip of the Stylus Cathode Used in Test MM-21, X4000	180
37	Post-Emission Appearance of the Pins on Cathode MM-21, X4250	180
38	Schematic Diagram of the Anode/Cathode Geometry Used in the Gun Test, MM-24	182
39	View of the Exposed Pins at the Tip of the Stylus Cathode Used in Test MM-24, X1100	183
40	Post-Emission Appearance of the Stylus Tip at the Conclusion of Test MM-24, X1000	185
41	View of the Exposed Pins at the Tip of the Stylus Cathode Used in Test MM-29, (a) X450, (b) X3250	188

LIST OF ILLUSTRATIONS

<u>Figure</u>	<u>Title</u>	<u>Page</u>
V-42	Image of the Defocused Electron Beam on the Phosphor Screen of the RCA Gun Used in Tests MM-28 and MM-29	189
43	Post-Emission Damage on the Stylus Tip Used in Test MM-39, X1800	191
44	Photograph of One of the Semicon Tubes in Operation, Illustrating the Degree of Anode Heating Produced by a Total Emission Current on One Milliampere at 2 kV	195

LIST OF TABLES

<u>Table</u>	<u>Title</u>	<u>Page</u>
II-I	Uranium Dioxide Powders Used in Characterization Studies	8
II	Effect of Moisture on the Calculation of the Oxygen-to-Uranium Ratio	12
III	Room Temperature Oxidation Characteristics of "As-Received" Urania Powders	13
IV	Sintering Tests on "As-Received" Urania Powders	17
V	Spectrographic Analysis of Uranium Dioxide Powders*, Microgram of Element per Gram of Uranium Metal	19
III-I	Parameters Controlling the Melt-Growth of $UO_2$ -W Composites	21
II	Analysis of W Fiber Densities and Diameters From Selected Locations in Sample Number LBH-5A.	26
III	Atmospheres Used, and Resulting Properties of Samples Used in Sintering Study	32
IV	Pellet Fabrication Data for $UO_2$ -W Samples LBH-8A, B, and C.	42
V	Growth Parameters of Composite Samples LBH-20, and LBH-21	45
IV-I	Melting Temperatures and $UO_2$ Contact Angles for Various Braze Materials	71
II	Summary of Braze-Substrate Combinations Investigated for Joining to $UO_2$ -W Composites	76
III	Composition of Chemical Etches for Pointing and Lengthening Tungsten Fibers in $UO_2$ -W Composites	89
IV	Milling Time, Ion Current, and Tungsten Fiber Diameter for Ion Milled $UO_2$ -W Composites with Exposed Fibers	95

LIST OF TABLES

<u>Table</u>	<u>Title</u>	<u>Page</u>
V-I	Values of the Functions $f(y)$ , $t(y)$ , and $s(y)$	101
II	High Voltage dc Power Supplies Used	120
III	Summary of Cathode Geometries Used and Results of the Emission Tests with the UF Anode	165
IV	Summary of Stylus Cathode Tests	173
VII-I	Results of $UO_2$ -W Solidification Experiments <sup>2</sup>	215

SECTION I  
INTRODUCTION

This is the Final Report describing research performed on the "Manufacturing Methods for Production of Field Effect Electron Emitters from Oxide-Metal Composite Materials," contract number DAAH01-75-C-0852, covering the period from 16 May 1975 through 15 November 1977. The conclusion section of this Report (Section VI) reviews and summarizes the significant accomplishments of the entire contract period. This program was divided into four tasks and the major objectives of these areas are outlined in this section. However, prior to considering the objectives, a brief review of the internal floating zone technique employed in the growth of the oxide-metal composites is presented. This description provides valuable background information for interpreting and evaluating the results of the various sections of this report.

A modified floating zone technique was used to grow oxide-metal composites.<sup>1,2</sup> These materials typically contain many millions of metallic fibers per cm<sup>2</sup>, each less than 1  $\mu$ m in diameter, uniformly embedded in an oxide (insulating or semi-conducting) matrix. In this

technique pressed rods of the oxide-metal mixture were sintered inside rf-heated molybdenum tubes, in an inert atmosphere, to densify and preheat the material. A schematic diagram of the growth facility is shown in Figure I-1. After the initial heating, which also served to increase the electrical conductivity of the oxides, the molybdenum tube heaters were separated to expose approximately 2 cm of the rod to an rf field normally between 3 to 5 megahertz (Mhz). Often only a single Mo preheater was used, and in this configuration the Mo tube was simply lowered out of the coil to expose the sample to the rf field. The concurrent increase of temperature, electrical conductivity and resistance heating continued until the interior of the rod melted at temperatures up to 3000°C. The high radiant heat loss from the surface and the inherent low thermal conductivity of the oxides maintained the skin of the rod well below the eutectic temperature of the mixture. The solid skin acted as a crucible to contain the molten zone. Composite growth was obtained by moving the molten zone up through the rod. In practice a cavity was generated in the molten zone because of the difference in density between the initial polycrystalline rod and solidified composite. During growth the oxide and metal melted from the roof of this cavity and solidified at

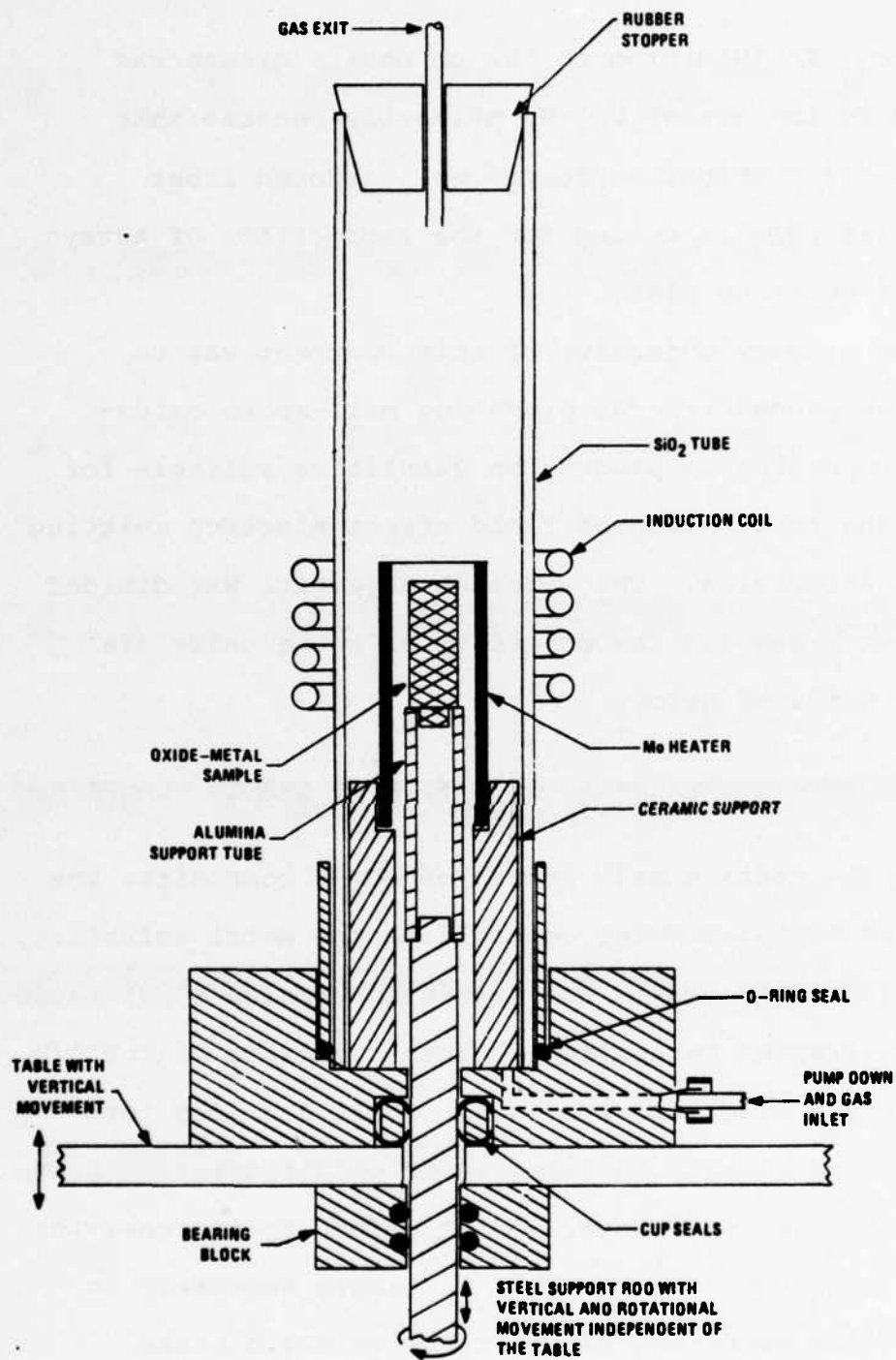


**Figure I-1.** Diagram of the Induction Heating Facilities Showing The Position of The Molybdenum Susceptor when used as a Preheater

the base. In this program the composite growth was limited to the system  $UO_2$ -W, primarily because this oxide-metal combination formed well ordered fiber geometries ideally suited for the fabrication of arrays of field emitting pins.

The primary objective of this contract was to establish procedures for producing melt-grown oxide-metal composites in production quantities suitable for use in the fabrication of field effect electron emitting cathode structures. The research objective was divided into four areas and the objective of these tasks are briefly outlined below.

A. PROCUREMENT AND CHARACTERIZATION OF URANIA TUNGSTEN POWDERS

In the routine melt growth of  $UO_2$ -W composites the most important parameter controlling the metal solubility in the liquid urania is the oxygen-to-uranium (O/U) ratio. This requirement necessitated premelt control of the O/U ratio of the starting materials. Short and long term oxidation rates were measured under conditions simulating powder storage conditions. In an effort to increase the size of the composite samples, it became necessary to prefabricate dense  $UO_2$ -W pellets using solid state sintering. Particle characterization of urania powders received from four vendors was correlated with their densification behavior.

## B. THE DEVELOPMENT OF OPTIMUM COMPOSITE GROWTH PROCEDURES

The following parameters were considered in establishing optimum growth procedures for the  $\text{UO}_2$ -W composites: Sample size, starting oxide-metal compositions, solidification atmosphere, influence of premelting ingot density, sintering atmosphere, solidification rate and the control of the molten zone. As a result of these studies a procedure for the routine growth of  $\text{UO}_2$ -W composite ingots weighing up to 500 grams was established.

## C. THE DEVELOPMENT OF MACHINING, BRAZING, AND ETCHING TECHNIQUES FOR THE PRODUCTION OF FIELD EFFECT ELECTRON EMITTERS

In order to utilize the composite materials as an array of field emitting pins, the fabrication of a cathode structure suitable for emission testing was necessary. The potential need to condition the pins by "in-situ" heating resulted in the screening of a number of high temperature braze materials. Finding a suitable metallic support compatible with the expansion characteristics of the  $\text{UO}_2$ -W emitters was a difficult task. Standard diamond grinding was employed to machine the different cathode geometries. Chemical etchants developed previously were used to expose the W fibers.

## D. EVALUATION OF FIELD EMISSION PERFORMANCE OF PROTOTYPE EMITTERS

Testing of prototype field emission cathodes was accomplished during this research program. These tests

included determination of the emission current capacity of individual pins in an array; the comparative emission performance of different array and pin tip geometries; and an investigation into the problems associated with operating a field emitter in a vacuum environment similar to that required by conventional thermionic cathodes. Based on the experimental results, array current densities over  $1 \text{ A/cm}^2$  are achievable. Some of the possible mechanisms leading to pin failures are reviewed and compared with pertinent experimental results.

## SECTION II

### PROCUREMENT AND CHARACTERIZATION OF UO<sub>2</sub> AND W POWDERS

In the unidirectional solidification of UO<sub>2</sub>-W composites the oxygen-to-uranium (O/U) ratio of the oxide is the most important parameter controlling the successful production of these materials. As a result, samples of urania were obtained from four different vendors for powder characterization, with emphasis on the measurement and control of the O/U ratio. The sample identification and the supplier are tabulated in Table II-I. In this section a description of the O/U ratio determination and associated errors in this measurement are described. The O/U ratio of the "as-received" powders was measured. The oxidation and storage behavior of these oxides was evaluated along with comparative moisture contents. The long-term oxidation characteristics of hydrogen-reduced powder was also studied since this treatment was necessary to obtain a reproducible O/U ratio in the starting UO<sub>2</sub>-W pellets. Sintering properties also became an important parameter because of the need to predensify the UO<sub>2</sub>-W pellets, especially for the successful solidification of the larger diameter samples. Scanning electron microscopy of the powders and spectrographic analysis for the metallic impurities are also reported.

Table II-I. Uranium Dioxide Powders Used in Characterization Studies

Sample	Supplier	Assay Date**
A*	Numec	8/23/73
B	Exxon Nuclear	10/2/75
C	Babcock & Wilcox	8/21/75
D	Nuclear Fuel Services	10/29/75

\*Sample A was from the  $UO_2$  supply that has been at Georgia Tech for several years.

\*\*The assay date is the date on which the radioactivity of the powder was last determined by the supplier.

Finally, the urania powder characteristics necessary for the successful growth of the  $UO_2$ -W composite structures are discussed.

No comprehensive characterization of the tungsten powders relative to their solidification behavior in the composites was undertaken. Tungsten powders from two vendors (Teledyne Wah Chang and Fairmount Chemical Company) were utilized in the growth experiments and both produced excellent tungsten fiber geometries. During melting, the tungsten was completely dissolved in the molten urania and lost all remnants of the original particle characteristics. All impurities, except perhaps for other refractory metals, were vaporized at the extremely high  $UO_2$ -W eutectic temperatures and deposited in the cooler regions of the sample. It was also established that small additions of tungsten, typically 6 weight percent (w/o), had very little influence on the sintering characteristics of the urania powders.

#### A. DETERMINATION OF THE OXYGEN-TO-URANIUM (O/U) RATIO

Uranium dioxide is a nonstoichiometric solid that will slowly oxidize to  $U_3O_8$  in air at room temperature. The determination of the O/U ratio was done by the standard gravimetric method. The  $UO_{2+x}$  was weighed in a platinum crucible, oxidized to  $U_3O_8$  in air at  $800^\circ C$ ,

and reweighed. The weight gain was assumed to be entirely from oxidation so the O/U ratio could be calculated using the atomic weights. There are two main sources of error in this measurement: 1) weighing errors, and 2) moisture on the powder.

Weighing errors, e.g., zero drift of the analytical balance, etc., was assumed to be  $\pm 0.0004$  grams. A typical error analysis calculation gave an O/U ratio accuracy of  $\pm 0.002$  for a powder with an O/U ratio of 2.050. This error was much less than that caused by absorbed moisture on the powder.

Calculation of the error due to moisture on the powder was much more complicated due to the inability to determine the exact amount of adsorbed water. Standard drying methods involving heating caused a change in the O/U ratio, so any weight change could not be attributed solely to the water. Since the water content of some of the "as-received" powder was undoubtedly at least 0.1 w/o, this parameter had a significant effect on the O/U ratio determination. Any moisture increased the calculated O/U ratio when the weight gain was assumed to be solely caused by oxidation, because the loss of moisture reduced the total weight gain resulting from oxidation. Hence, the reduced weight gain indicated the O/U ratio was larger than the "true" value. Table II-II

shows the effect of various moisture contents on the apparent O/U ratio for five different starting values. The moisture content is expressed as a weight percent (on a dry basis)

$$\frac{\text{Weight H}_2\text{O}}{\text{Weight Dry UO}_{2+x}} \times 100\%$$

The table shows, for example, that a powder containing 0.2 w/o moisture with a "true" O/U value of 2.0508 will yield an apparent O/U value of 2.0685. The error in O/U ratio from this source was about +0.01 to +0.03 for most "moist" UO<sub>2</sub> powders.

The O/U ratios given in this report were calculated without any attempt to correct for the expected increase in O/U ratio due to moisture. When interpreting the O/U data, for the "as-received" and "H<sub>2</sub>-reduced" powders, this uncertainty exists. The sintered bulk UO<sub>2</sub> pellets were essentially dry and not subject to this error.

#### B. STORAGE OF "AS-RECEIVED" POWDERS

Three hundred-gram batches of the four "as-received" UO<sub>2</sub> powders were stored in screw top glass jars in order to establish a uniform treatment procedure. Two gram samples were taken from each jar for O/U ratio determinations. Three weeks and eight months later, similar groups of samples were tested in order to detect any change in stoichiometry during storage. Table II-III gives these results.

Table II-II. Effect of Moisture on the Calculation of the Oxygen-to-Uranium Ratio.

		O/U Ratios									
TRUE (dry)		APPARENT VALUES BECAUSE OF MOISTURE CONTENT									
Moisture Content w/o,	0.00	0.1	0.2	0.3	0.4	0.5	1.0	1.5	2.0		
	1.9998	2.0174	2.0333	2.0509	2.0668	2.0845	2.1691	2.2520	2.3368		
	2.0508	2.0685	2.0845	2.1022	2.1181	2.1358	2.2207	2.3039	2.3889		
	2.1005	2.1182	2.1342	2.1520	2.1679	2.1857	2.2709	2.3543	2.4395		
	2.1504	2.1682	2.1843	2.2021	2.2181	2.2359	2.3213	2.4050	2.4904		
	2.1990	2.2168	2.2329	2.2508	2.6680	2.2847	2.3704	2.5442	2.5400		

Table II-III. Room Temperature Oxidation Characteristics of "As-Received" Urania Powders.

Power Supplier	11/14/75	O/U Ratio 12/6/75	7/12/76	% Increase for 8 mos.
A-Numec	2.270	2.283	2.289	0.837
B-Exxon Nuclear	2.111	2.122	2.128	0.805
C-Babcock & Wilcox (Numec)	2.104	2.111	2.135	1.473
D-Nuclear Fuel Services	2.160	2.156	2.165	0.231

Samples A, B, and C showed a slight increase in O/U ratio as expected due to the slow, natural oxidation processes occurring at room temperature. Sample D displayed an unexplained decrease in O/U ratio after the first three weeks.

#### C. MOISTURE CONTENT

In order to determine the moisture content of the "as-received"  $UO_{2+x}$  powders, a two-gram sample of each was placed in a porcelain ignition crucible and stored in a desiccator with Drierite desiccant. An empty crucible was used as a control. Sample A showed a weight loss of 0.16% which can be attributed to the drying of the powder. The rest of the samples showed only very small weight changes, all within the weighing error.

#### D. OXIDATION PROPERTIES

Oxidation characteristics of the "as-received" powders (with different starting O/U ratios) were studied by placing powders in a dryer held at 80°C and measuring the O/U ratio at intervals up to 100 hours. The oxidation behavior for the different powders is shown in Figure II-I. Sample A showed a significant decrease in the apparent O/U ratio during the first 24 hours, undoubtedly due to the drying of the powder. Samples B, C, and D showed only the slow rise in O/U ratio due to oxidation with no weight decrease, because they were essentially dry at the beginning of testing. The comparison of powder oxidation behavior agreed with the moisture content evaluation reported in the previous section.

For most  $UO_2$ -W composite growth experiments, however, it was necessary to have urania with an intermediate O/U ratio, ideally between 2.04 and 2.07. Accordingly, a sample of the Exxon powder was reduced in  $H_2$  at 600°C to an O/U ratio of 2.00. It was then quenched in dry ice and exposed to room temperature air until all of the dry ice had sublimed. The powder was then stored in a desiccator to limit moisture absorption. The O/U ratio after reduction and dry ice quench was 2.055, and after 2 months of storage the O/U ratio had increased to 2.070. Continual storage for an additional 11 months

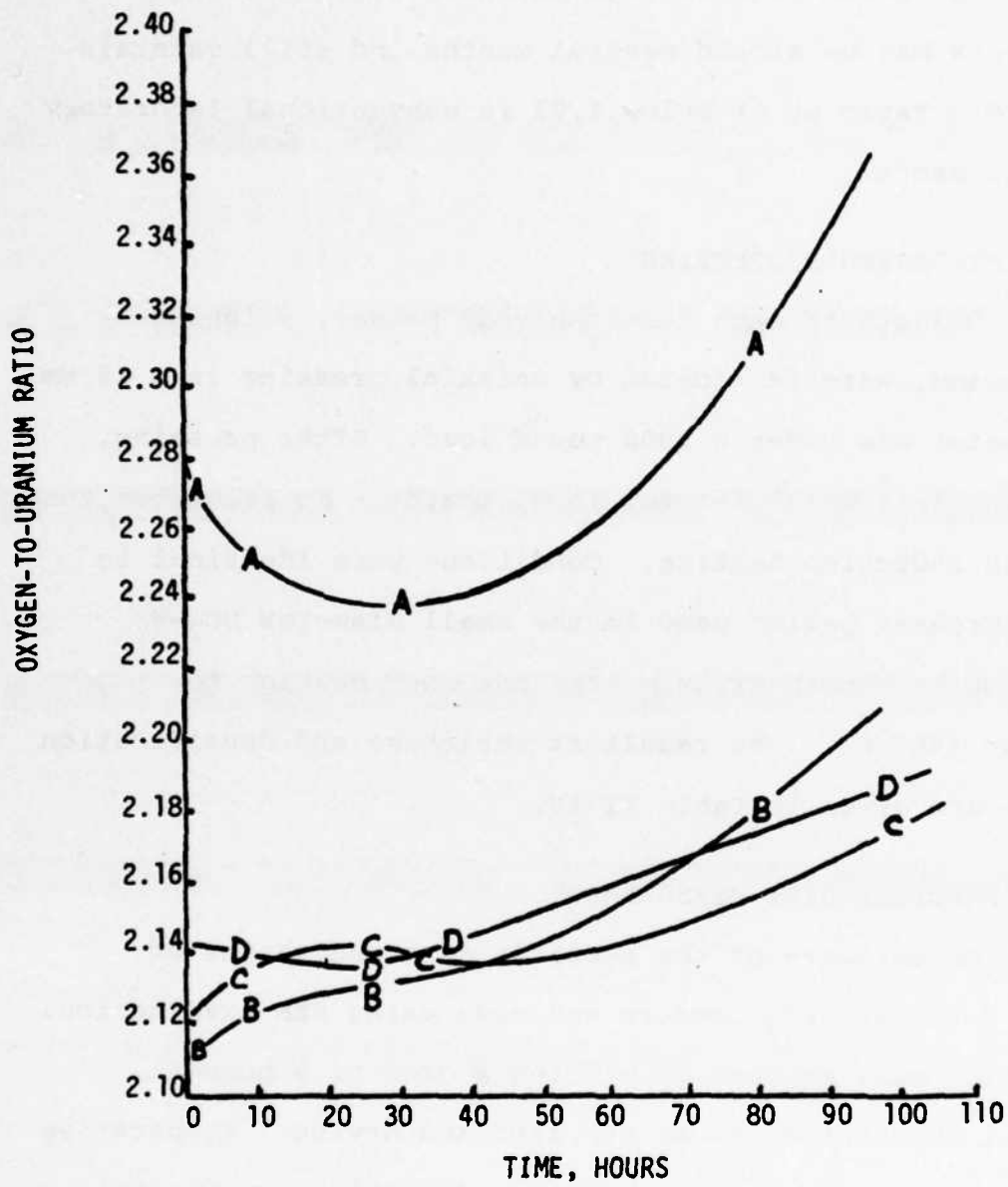


Figure II-1. Oxidation of  $UO_{2+x}$  Samples at  $80^{\circ}C$ .

(13 months from the H<sub>2</sub> reduction) resulted in an O/U ratio of 2.086. These data indicate reduced urania powders may be stored several months and still maintain the O/U ratio at or below 2.07 in conventional laboratory desiccators.

#### E. SINTERING PROPERTIES

Pellets of each "as-received" powder, weighing 50 grams, were fabricated by uniaxial pressing in a 19 mm diameter die under a 2000 pound load. After pressing, the pellets were sintered in N<sub>2</sub> inside a Mo preheater tube using induction heating. Conditions were identical to the preheat period used in the small diameter UO<sub>2</sub>-W composite growth experiments (one hour heating to about 1400°C). The resultant shrinkage and densification data are given in Table II-IV.

#### F. PARTICLE SIZE MEASUREMENT

An estimate of the particle size and shapes of the different UO<sub>2</sub> powders was made using SEM examination. Samples were mounted by placing a drop of a powder-water suspension on an SEM stub and drying. Comparative analysis of SEM micrographs provided only very general information and indicated the average particle size of all the powders was about 0.3 μm. The particles in Sample B (the Exxon powder) were more agglomerated than those in the other three powders.

Table II-IV. Sintering Tests on "As-Received" Urania Powders.

Sample	As-Received O/U	Fired O/U	Weight Loss on Firing (%)	Longitudinal Shrinkage (%)	Diameter Shrinkage (%)	Green Density (gm/cc)	Fired Density (gm/cc)
A	2.270	2.179	0.77	26.2	28.0	3.56	9.23
B	2.111	2.113	0.22	23.7	24.3	4.04	9.20
C	2.104	2.083	0.27	24.8	26.5	3.71	9.12
D	2.160	2.124	0.33	24.3	25.6	4.07	9.68

#### G. SPECTROGRAPHIC ANALYSIS

Spectrographic analysis of the four urania samples for metallic impurities was conducted at Oak Ridge National Laboratory. The results are listed in Table II-V. The impurities were similar in all powders, with Fe and Si the major contaminants. In this analysis, Samples C and E were identical and the spectrographic results agreed very well, except for the Fe content.

#### H. SUMMARY OF URANIA POWDER CHARACTERISTICS

As noted previously the most important parameter controlling the successful growth of the  $UO_2$ -W composites was the oxygen-to-uranium ratio. However, because  $UO_{2+x}$  powders are unstable at room temperature and slowly oxidize to  $U_3O_8$ , it is impractical to attempt to control the O/U ratio during long term storage. To obtain a reproducible starting O/U ratio is was necessary to periodically reduce batches of urania powder to  $UO_{2.00}$  in hydrogen, followed by a controlled oxidation to about  $UO_{2.05}$ . These powders could then be stored in desiccators for several months and still maintain an O/U ratio below 2.07. This material, after blending with tungsten powder, proved to be satisfactory for sintering to form pellets suitable for internal melting

Table II-V

Spectrographic Analysis of Uranium Dioxide Powders\*,  
Microgram of Element per Gram of Uranium Metal

Element**	Uranium Dioxide Powders				
	A	B	C	D	E
Al	< 2	8	8	10	10
B	< 0.1	< 0.1	< 0.1	< 0.1	< 0.1
Ba	< 1	< 1	< 1	< 1	< 1
Be	< 0.1	< 0.1	< 0.1	< 0.1	< 0.1
Bi	< 1	< 1	< 1	< 1	< 1
Ca	< 2	< 2	5	< 2	8
Cd	< 0.1	< 0.1	< 0.1	< 0.1	< 0.1
Co	< 1	< 1	< 1	< 1	< 1
Cr	< 2	< 2	10	5	10
Cu	< 2	< 2	< 2	< 2	< 2
Fe	10	< 5	< 5	< 5	30
Li	< 2	< 2	< 2	< 2	< 2
Mg	< 2	< 2	2	< 2	< 2
Mn	< 2	< 2	< 2	< 2	< 2
Mo	< 2	< 2	< 2	< 2	< 2
Na	10	25	7	15	7
Ni	< 2	< 2	5	10	5
P	< 40	< 40	< 40	< 40	< 40
Pb	< 2	< 2	< 2	< 2	< 2
Sb	< 5	< 5	< 5	< 5	< 5
Si	< 2	15	50	60	60
Sn	< 2	< 2	< 2	< 2	< 2
Y	< 2	< 2	< 2	< 2	< 2
Zn	< 20	< 20	< 20	< 20	< 20

\*Supplier  
 A . Numec  
 B Exxon Nuclear  
 C Babcock and Wilcox  
 D Nuclear Fuel Services  
 E Same as C for reproducibility check

\*\* < means below detection limit

(sintering and melting procedures are described in Section III). Therefore no stringent O/U ratio requirement is necessary in the procurement of urania powders. As indicated in Table II-III most available powders have ratios of 2.10 to 2.20. The only real disadvantages to powders with O/U ratios above 2.15 is the excessive amount of water liberated during the reduction treatment.

An additional requirement of these powders is the need to sinter to densities of 85 to 95 percent of theoretical. Since densification must be accomplished in a nitrogen atmosphere (for the control of the O/U ratio, as described in the next section) the enhanced sinterability of hyperstoichiometric  $UO_2$  can be utilized. Most urania powders easily meet this density requirement. In summary, the nuclear grade urania powder specifications are more than adequate for the procurement of material for use in the growth of the unidirectionally solidified  $UO_2$ -W composites.

### SECTION III

#### DEVELOPMENT OF OPTIMUM COMPOSITE GROWTH PROCEDURES

This section describes the parameters studied in an effort to optimize the routine melt-growth of  $\text{UO}_2\text{-W}$  composites using unidirectional solidification. Although an effort was made to divide these parameters into the subtopics listed in Table III-I, it should be noted that most of these parameters are interrelated and affect each other.

Table III-I. Parameters Controlling the Melt-Growth of  $\text{UO}_2\text{-W}$  Composites

- 
- A. Sample Size and Fiber Array Uniformity
  - B. Oxide-Metal Composition
  - C. Solidification Atmosphere
  - D. Pre-Melt Ingot Stoichiometry and Density
  - E. Solidification Rate
  - F. Molten Zone Control
  - G. Cracking Characteristics
- 

Prior to discussing the experimental results in detail, it would be beneficial to briefly describe the "state of the art" in the unidirectional solidification of eutectic structures in the  $\text{UO}_2\text{-W}$  system which existed before this work was begun. The basic growth technique remains the same as described in the Introduction

(Section I). Prior to initiating this study, the critical influence of oxide stoichiometry on tungsten solubility in molten urania was recognized. The major problems in the routine and optimum growth of  $UO_2$ -W composites are summarized below. For uniform fiber arrays to be grown for long lengths, it was necessary to obtain and maintain a homogeneous solution of the metal atoms in the molten oxide. It was seen, in the early work, that the solidified oxide-metal composites typically contained less metal than originally used in the starting mixture. Consequently, any reproducible and satisfactory growth scheme must contend with the continual depletion of the metal from the molten zone, predominantly through some type of vaporization or oxidation process. In the case of  $UO_2$ -W, this process was further complicated by the need to maintain the stoichiometry (O/U ratio) of the molten oxide above 2.00, since the increased oxygen potential required to satisfy this requirement aggravated the tungsten oxidation and vaporization problems. In addition, any modification of the growth scheme designed to maintain steady state and uniform conditions during solidification required that the system be maintained at temperatures in the neighborhood of  $2800^{\circ}C$ , where oxidation and vaporization reactions proceeded very

rapidly. Because of these problems, in prior work the successful oxide-metal composite growth was limited to lengths of about one centimeter. The decision was made at the outset of this program to attempt to increase the size of the starting samples, or ingots. Increased sample size would yield larger areas of uniform fiber array, and, hopefully, decrease the rate of metal loss by increasing the mass-to-surface area ratio of the molten material. Significant increases in sample size and fiber uniformity were achieved and these results are described in this section.

The growth parameters and general results of the various growth runs are tabulated in Appendix A.

#### A. SAMPLE SIZE AND FIBER ARRAY UNIFORMITY

In previous  $UO_2$ -W solidification experiments as well as in preliminary runs conducted during this investigation, sample pellets with unfired (green) diameters of 19 mm and sintered diameters of about 16 mm were employed. Since the kinetic reactions associated with the very high temperatures required to grow  $UO_2$ -W composites cannot be avoided, the decision was made to increase the diameter of the ingots. Transverse sections of the three different ingot diameters studied are shown in Figure III-I. The smallest wafer (16 mm diameter)

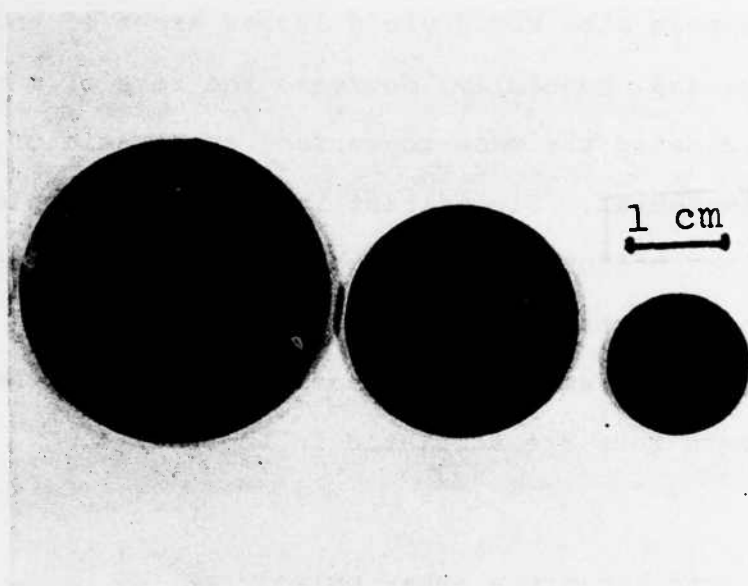


Figure III-1. Transverse Sections of 16, 25, and 32, Millimeter Diameter UO<sub>2</sub>-W Samples.

is typical of the  $UO_2$ -W samples solidified prior to this study, while the intermediate (25 mm) and large diameter (32 mm) wafers are from experiments performed during this research.

Preliminary runs indicated that with minor adjustments to existing equipment, including decreasing the rf frequency from 3.7 to 3.4 megahertz, sintered intermediate size ingots 25 mm in diameter (32 mm green) could be easily melted and solidified. An encouraging feature was the significantly larger cell sizes present in the larger diameter samples. That improvement is probably attributable to the wider and flatter liquid-solid interface present in the larger samples. Evaluation of those samples revealed that the uniformity of the fiber geometries was also greatly improved compared to the smaller samples, providing substantial areas of uniform composite for the fabrication of emitter arrays.

Evaluation of fiber geometry uniformity of the small (16 mm) diameter ingots revealed that the transverse fiber density of  $UO_2$ -W composites varied less than  $\pm 10\%$  within several millimeters of the center of the solidified zone. Density changes increased to  $\pm 20\%$  as the distance from the center increased, and at the edge, very large variations in density were observed. It was also noted that fiber density generally decreased

from the base to the top of the solidified zone.

Variations in fiber densities of the 25 mm diameter samples followed the same trends displayed by the smaller pellets, but were reduced by about one half.

A typical 25 mm diameter ingot, having a starting composition of  $UO_{2.07-6}$  weight percent (w/o) W and solidified at 2.8 cm/hr, was sectioned at three levels in the melt zone. Central and circumferential areas of each wafer were examined using a scanning electron microscope and representative pin densities and diameters were measured from SEM photographs and recorded in Table III-II. These results indicate that the fiber diameter generally increased with decreasing fiber density at both the centers and the edges of the wafers. Based on this data, there is no apparent trend in the relationship between center and edge pin diameters. A typical SEM micrograph of uniform fiber growth in the  $UO_2$ -W composites is shown in Figure III-2.

Table III-II. Analysis of W Fiber Densities and Diameters From Selected Locations in Sample Number LBH-5A.

Slice Number	Level From Bottom of Zone (mm)	Fiber Density ( $10^6$ pins/cm <sup>2</sup> )		Fiber Diameter ( $\mu$ m)	
		center	edge	center	edge
4	4	13.0	11.4	0.35	0.44
5	9	12.1	10.0	0.43	0.44
8	30	9.8	6.3	0.47	0.58

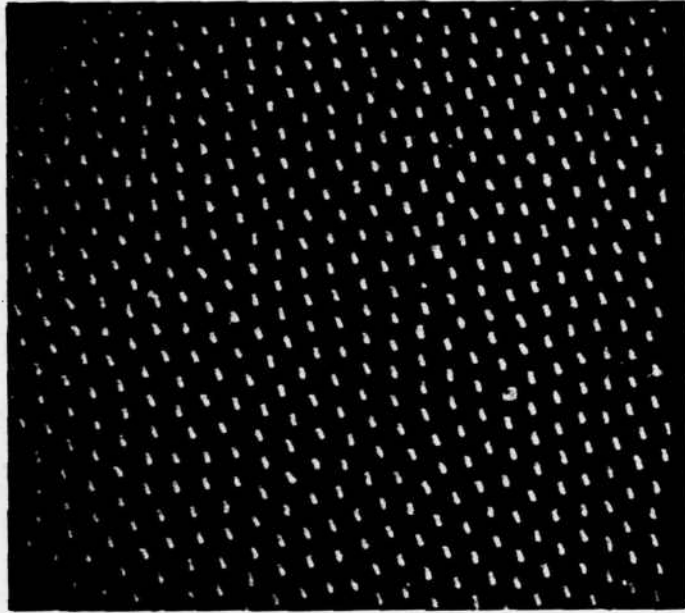


Figure III-2. Uniform Tungsten Fiber Geometry  
in  $\text{UO}_2$ -W Composite, SEM X500.

Further experiments (LBH-11, 12) designed to increase the size of the starting ingots showed that uniform fiber geometries could be grown in  $\text{UO}_2$ -W samples that are approximately 32 mm in diameter, but there were some problems associated with the unidirectional solidification of larger ingots. An analysis of the shape of the solidified zone and associated void in these samples suggested that there were substantial heat losses from the top of the sample, and that the rf power penetration depth was marginal for complete melting to the center of the ingot. In an effort to overcome those problems, the tank circuitry of the Lepel rf generator was modified to decrease the frequency and improve power penetration; but only a small change could be made (from 3.4 to 3.1 MHz) without adversely affecting the efficiency of the generator.

Because of the problems associated with the use of the large (32 mm diameter) ingots, including materials utilization (500 grams per run versus 250 grams for the 25 mm diameter pellets), the 25 mm diameter sample size was chosen for most experiments. While the utilization of the 25 mm diameter  $\text{UO}_2$ -W ingots yielded improved eutectic geometries of increased size, it also required isothermal pre-sintering of the ingots prior to internal melting and resolidification. That requirement necessitated

an investigation of stoichiometry changes and densification during sintering as a parameter controlling the growth of  $\text{UO}_2$ -W composites. These areas are covered in later parts of this section. Having selected an ingot diameter of  $\sim 25$  mm the investigation was directed toward the effect of oxide-metal composition on the eutectic structures in the  $\text{UO}_2$ -W samples.

#### B. OXIDE-METAL COMPOSITION

Past studies<sup>2</sup> indicated that the unidirectional solidification of 16 mm diameter ingots having a starting composition of urania with an O/U ratio of 2.04 and 6 w/o tungsten yielded uniform fiber geometries ranging from 10 to 30 million fibers per square centimeter. In previous work it was often noted that uniform fiber growth was obtained for only short lengths before changing into degenerate morphologies unusable for the production of emitter arrays.

During this investigation, the unidirectional solidification of 25 mm diameter samples containing  $\text{UO}_2$  + 6 w/o W also yielded fiber densities from 5 to 30 million per square centimeter but the growth lengths were substantially longer than had been achieved previously. Therefore, since this composition also appeared to be optimum for the intermediate-sized samples, no further changes in oxide-metal composition were made.

The influence of solidification (growth) atmosphere on the characteristics of  $UO_2$ -W composites is discussed in the following section.

### C. SOLIDIFICATION ATMOSPHERE

Recent studies on molten pure urania indicated that a CO-1 v/o  $CO_2$  atmosphere yielded an O/U ratio near  $2.03^3$ , and since tungsten solubility is substantial at this O/U ratio<sup>4</sup>, the atmospheres tested were designed to provide oxygen potentials that would establish O/U ratios in the molten oxide near 2.03. In  $UO_2$ -W solidification experiments where the inlet gas was monitored using a gas chromatograph and consisted of CO with 0.1 v/o  $CO_2$ , the exit gas composition showed an extremely high concentration of  $CO_2$  (8-10 v/o) during the initial melting. During the period of growth (approximately 90 minutes), the  $CO_2$  content slowly decreased and eventually stabilized at 0.3 v/o.

An experiment was run to ascertain the O/U ratio obtained when a pure  $UO_{2.04}$  sample was melted and held until the exit gas reached the CO-0.3 v/o  $CO_2$  composition. Post-melting analysis showed the O/U ratio was 2.023. In an additional test, the Mo pre-heater was run at approximately  $1400^\circ C$  without any oxide-metal mixture in the CO-0.1 v/o  $CO_2$  mixture, and again the equilibrium concentration of  $CO_2$  was about 0.3 v/o. This behavior

suggests the reaction,  $2\text{CO} \rightarrow \text{C} + \text{CO}_2$ , occurred in the system. Conclusive evidence for this reaction was the presence of carbon black found on samples and support fixtures. Similar samples, grown in a CO-1.0 v/o  $\text{CO}_2$  atmosphere, displayed a similar pattern, reaching an equilibrium  $\text{CO}_2$  concentration of about 1.2 v/o.

The atmosphere consisting of CO-1.0 v/o  $\text{CO}_2$  was selected for use in most of the  $\text{UO}_2$ -W solidification experiments because the resultant oxygen potential in the molten urania resulted in adequate tungsten solubility ( $\sim 3$  w/o). Furthermore, obtaining  $\text{CO}_2$  contents less than 1 v/o was difficult using conventional gas flow meters.

Having established the size, metal content of the  $\text{UO}_2$ -W ingots and the atmosphere used during the growth procedure, an evaluation of the effects of the O/U ratio of the oxide (as determined by sintering parameters) and of the bulk density of the pellets on eutectic structures was undertaken.

#### D. PRE-MELT INGOT STOICHIOMETRY AND DENSITY

With the efforts to increase the size of the solidified  $\text{UO}_2$ -W ingots it was discovered that a separate sintering (densification) step was necessary in order to form dense cylinders suitable for internal melting. Consequently the O/U ratio and sample density after

sintering became important parameters controlling the successful growth of the  $\text{UO}_2$ -W composites. In this evaluation a series of experiments was performed in which reducing, neutral, and oxidizing atmospheres were utilized during the sintering of samples LBH-16, -18, and -19, respectively. The starting compositions of all samples was urania with an O/U ratio of 2.07 mixed with 6 w/o tungsten metal. Included with each sample during sintering was a smaller  $\text{UO}_2$ -W pellet for the purpose of establishing the sintered, pre-growth microstructure of the pellets, and a pure  $\text{UO}_2$  pellet for evaluating the post-sintering O/U ratio. Green densities of the as-pressed oxide-metal pellets were  $4.65 \pm 0.05$  g/cc. All samples were sintered at  $1400^\circ\text{C}$  for 4 hours during a 36-hour total firing cycle. The sintering parameters and associated properties are listed in Table III-III.

The reducing atmosphere used in experiment LBH-16 consisted of  $\text{N}_2 + 30$  v/o  $\text{H}_2$ . The sample pellet had a fired density of 8.83 g/cc and an O/U ratio of 2.00, with

Table III-III. Atmospheres Used, and Resulting Properties of Samples Used in Sintering Study.

Sample	Sintering Atmosphere	Fired Density (g/cc)	Fired O/U Ratio
LBH-16	$\text{N}_2:30\text{v/o H}_2$	8.83	2.00
LBH-18	$\text{N}_2$	9.77	2.01
LBH-19	$\text{CO}_2$	9.17	2.10

the tungsten appearing as elemental metal particles in the oxide matrix (Figure III-3). After unidirectional solidification, using standard procedures in a CO-1 v/o CO<sub>2</sub> atmosphere, the pellet was longitudinally sectioned. A reasonably well-developed solidified zone was present (Figure III-4), but no metal fibers were found and most of the W appeared as metal droplets frequently associated with pores. This behavior was expected, since tungsten solubility is very limited in molten urania with an O/U ratio near 2.00.<sup>4</sup> During solidification of this sample, initial analysis of the exit gases (using the gas chromatograph) showed a decrease in CO<sub>2</sub> content from the inlet analysis of 1.0 v/o to about 0.15 v/o, indicating that the sample was extracting oxygen from the atmosphere. However, CO<sub>2</sub> content of the exit gas gradually increased and was about 0.95 v/o at the end of the run.

Nitrogen flowing at 300 cc/min was the "neutral" atmosphere used in experiment LBH-18. This atmosphere produced a sintered oxide-metal sample with a density of 9.77 g/cc, and an O/U ratio of 2.01. Microscopic examination (Figure III-5) showed that the pellet consisted of UO<sub>2</sub> with no preferred grain boundary or pore orientation. The tungsten was present as rounded metal particles often surrounded by a "blue" phase (with an approximate formula of U<sub>x</sub>WO<sub>3</sub>). This phase has been frequently seen in the cell boundaries of the UO<sub>2</sub>-W composite samples after solidification.

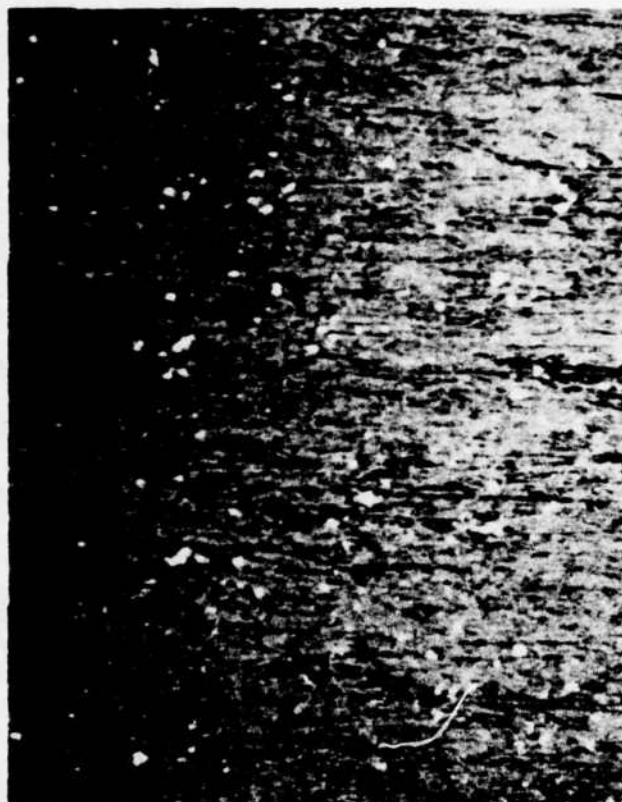


Figure III-3. Photomicrograph of  $\text{UO}_2\text{-W}$  Sample Sintered in a Reducing Atmosphere ( $\text{H}_2/\text{N}_2$ ) Showing Elemental Metal and Oriented Oxide Grains, X196.

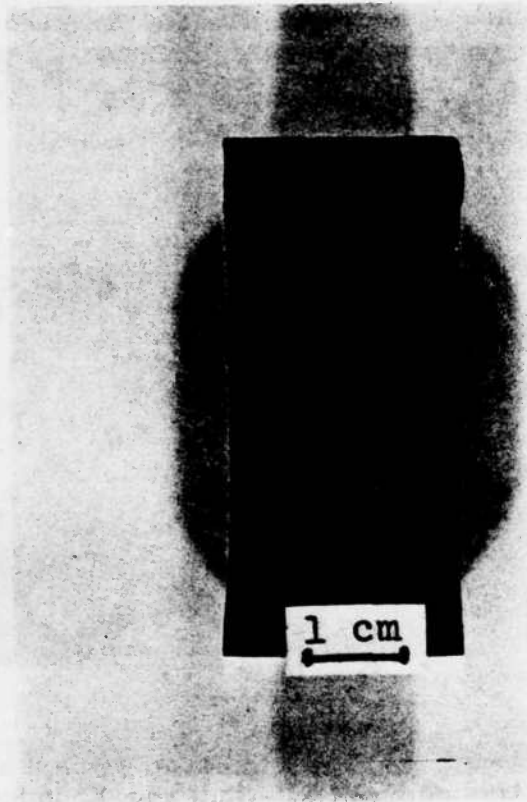


Figure III-4. Post-Run Longitudinal Section of  $\text{UO}_2$ -W Sample Sintered in a Reducing Atmosphere, (LBH-16).

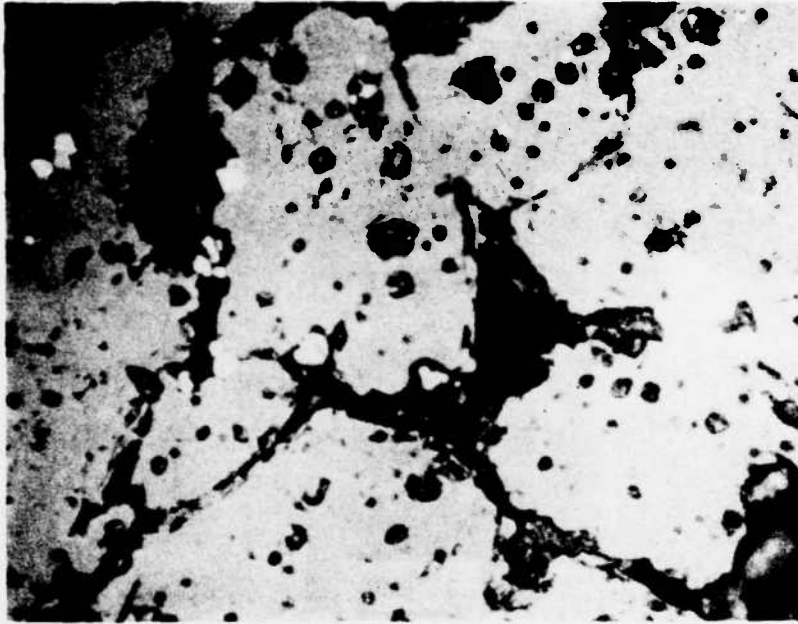


Figure III-5. Sample Pellet Sintered in a Neutral Atmosphere ( $N_2$ ) Showing Rounded Metal Particles Surrounded by "Blue Phase", X542.

After unidirectional solidification of sample LBH-18 using standard procedures, extensive areas of "good" fiber growth were observed with a few small areas of the "blue" phase in the grain (cell) boundaries. Gas chromatograph traces of the exit gas during this experiment showed a brief but large outgassing of oxygen (reflected by a high CO<sub>2</sub> content) as melting was initiated. The presence of CO<sub>2</sub> in the exit gas slowly decreased until a final value of about 1.3 v/o was reached near the end of the experiment.

An oxidizing atmosphere consisting of CO<sub>2</sub> flowing at 300 cc/min was used during the sintering of the UO<sub>2</sub>-W pellet during experiment LBH-19. After sintering, the O/U ratio was 2.10, and the pellet appeared grainy and porous (Figure III-6) and had a density of 9.17 g/cc. During solidification in the standard CO-1 v/o CO<sub>2</sub> atmosphere, extreme outgassing and vaporization from the pellet coated the atmosphere-containment tube and it was not until the end of the run that it was discovered that the pellet had expanded during internal melting and stuck in the molybdenum post-heater. Because of this difficulty, molten zone travel was limited to approximately 1 cm (Figure III-7). However, after two hours of stationary melting, there was still enough W dissolved in the molten oxide to produce aligned fibers as the



Figure III-6. Sample Pellet Sintered in an Oxidizing Atmosphere ( $\text{CO}_2$ ) Showing Extreme Porosity, X196.



Figure III-7. Sample LBH-19 After Growth Run Showing Area of Good Growth at Top of Solidified Zone.

melt solidified during cooling. This behavior suggested that higher O/U ratios may help in the effort to produce long lengths of uniform composite materials. Exit gas analysis during experiment LBH-19 showed a very high initial volume of CO<sub>2</sub>, that decreased to about 3 v/o during the two and one-half hour run. This behavior indicated a continual removal of oxygen from the sample throughout the experiment.

Experiment LBH-5, using a sample with a very high O/U ratio (2.20) and a corresponding increase in metal content to 12 w/o, was run in the CO-1 v/o CO<sub>2</sub> atmosphere in an attempt to grow long lengths of continuous fibers. During melting, a very irregular, unstable zone was formed, and post solidification examination (Figure III-8) revealed that the interior of the rod was very irregularly melted. This information indicates an upper-limit to useful O/U ratios is near 2.10.

The role of the pre-melting sample pellet density on the growth characteristics of the UO<sub>2</sub>-W composites was also studied. Three pellets were fabricated using the standard starting composition (UO<sub>2.07</sub>-6 w/o W) and the densities were controlled by varying pressing procedures to produce the sintered properties listed in Table III-IV. The pellets were pressed in a 32 mm diameter die, and sintered in a N<sub>2</sub> atmosphere at 1400°C for four hours.



Figure III-8. Post-Run Longitudinal Section of LBH-5 Showing the Irregular Unstable Molten Zone.

The three sintered samples were melted and unidirectionally solidified using the established growth procedures.

Table III-IV. Pellet Fabrication Data for  $UO_2$ -W Samples LBH-8A, B, and C.

Sample	Prepressing Load (lbs)	Final Pressing Load (lbs)	Green Density ( $g/cm^3$ )	Sintered Density ( $g/cm^3$ )
LBH-8A	4000	2500	4.16	8.01
LBH-8B	4000	5000	4.43	8.83
LBH-8C	4000	7500	4.60	8.55

Samples LBH-8A and LBH 8B displayed double voids (Figure III-9) while LBH-8C, the sample of highest density, showed an area of poorly-melted material in place of the top void. No tungsten fiber growth was present in the lowest density sample (8A) while the intermediately-dense pellet (8B) displayed irregular fiber arrays in the area between the two voids. Sample LBH-8C showed very uniform, low-fiber-density growth above, below, and on either side of the poorly melted region of the molten zone. Note, however, that the pre-melting, sintered densities of these three samples were 0.5 to 2.0 g/cc lower than that of most sample pellets utilized for composite growth (cf Appendix A). These data show that samples with sintered densities less than 75 to 80% of theoretical form unstable void-liquid configurations



Figure III-9. Sample LBH-8B, Showing Double Void.

undoubtedly because of the excessive amount of porosity that must be collected during zone travel.

#### E. SOLIDIFICATION RATE

The influence of the solidification rate on composite structures formed during unidirectional solidification has shown that a decrease in growth rate decreased the fiber density with an accompanying increase in fiber diameter. This behavior was utilized successfully to reduce the fiber density of two  $\text{UO}_2$ -W samples described in Table III-V. (Theoretical analysis of the field emission performance of multi-pin arrays suggests that lowering the pin densities of emitter samples should help to improve electron emission capability.)

Experiments LBH-20 and -21 consisted of  $\text{UO}_2.07^{-6}$  w/o W samples that were sintered in a nitrogen atmosphere to densities of 10.30 and 9.87 g/cc, respectively. The preheating of the samples prior to unidirectional solidification was conducted in the usual manner, utilizing a  $\text{N}_2$  atmosphere. Just prior to internal melting, the growth procedure was modified in experiment LBH-20 to reduce the fiber density. The growth atmosphere was changed from the "standard" CO-1 v/o  $\text{CO}_2$  to CO-0.5 v/o  $\text{CO}_2$  in order to lower the oxygen potential and the amount of W soluble in the molten urania. The growth rate was also lowered from the usual 3.0 cm/hr to 1.5 cm/hr

Table III-V. Growth Parameters of Composite Samples LBH-20, and LBH-21.

Sample	Starting O/U	W Content (w/o)	Post-sinter O/U	Post-sinter Den. (g/cc)	Solidification Rate (cm/hr)	Avg. Fiber Density (10 <sup>6</sup> pins/cm <sup>2</sup> )
LBH-20	2.07	6	2.01	10.30	1.50	5.0
LBH-21	2.07	6	2.01	9.87	0.50	1.6

to further reduce the tungsten pin density. Post-run analysis of the sample, using photomicrographs of transverse sections (Figure III-10), revealed uniform fiber geometries with densities ranging from 4 to  $5 \times 10^6$  fibers/cm<sup>2</sup>. Cracking in the center was limited to intergranular fissures, and the grains were large enough to permit the fabrication of single-cell emitter samples up to about 4 mm in diameter.

Since, compared with previous runs, it was possible to make a significant reduction in fiber density during experiment LBH-20, experiment LBH-21 was performed utilizing the CO-1 v/o CO<sub>2</sub> atmosphere and further reducing the growth rate to 0.5 cm/hr. Post-run analysis of this sample showed cracking characteristics and cell sizes similar to those in LBH-20, and the tungsten fiber densities between 1.4 and 1.7 million fibers/cm<sup>2</sup> (Figure III-11). Interestingly, the better fiber geometries were found in the upper portion of this ingot, whereas just the opposite behavior was typical in the small diameter (16 mm) ingots. It had been anticipated prior to these experiments that the loss of W through vaporization processes would restrict the solidification of uniform fiber geometries during long term, slow growth rate experiments.



Figure III-10. Photomicrograph of Transverse Section of Sample LBH-20 Showing Tungsten Fiber Array, X542.

(a)



(b)

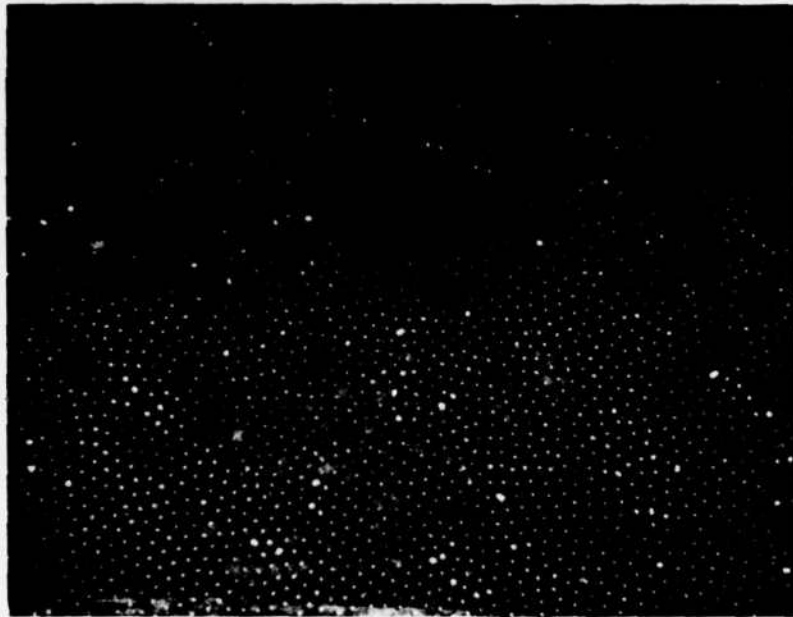


Figure III-11. Transverse Section of (a) Sample LBH-21, Showing High Degree of Uniformity and Extremely Low Fiber Density ( $1.6 \times 10^6$  pins/cm<sup>2</sup>), and (b) Sample LBH-10A for Comparison ( $31 \times 10^6$  pins/cm<sup>2</sup>), X945.

The capability of reducing the pin density of samples by almost a factor of ten was significant as it provided low density W pin arrays for testing as field emitters.

#### F. MOLTEN ZONE CONTROL

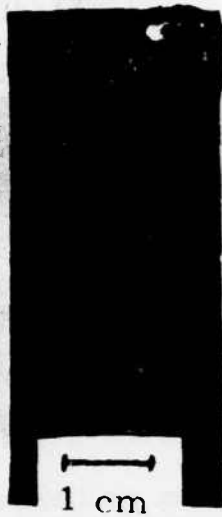
Molten zones were easily established in most of the  $UO_2$ -W solidification experiments, expanding over the entire length of the pellets as the power was increased, and the control of the size, shape and translation of the zone were key factors in achieving reproducible uniform eutectic structures. A comparison of two samples that had almost identical properties and treatments, except for an 8 to 10% difference in input rf power during melting and solidification, provided some insight into this parameter.

The two samples LBH-4 (low input power) and LBH-15A (10% greater input power) contained 6 w/o W, had approximately the same sintered densities, and were solidified at nearly the same growth rates. The increased power input in experiment LBH-15A lengthened the molten zone about 40% prior to zone travel and resulted in the homogenization of a greater mass of material prior to solidification. Post-run analysis revealed similar fiber densities,  $10 \times 10^6/cm^2$  for LBH-4 versus  $12 \times 10^6/cm^2$  for LBH-15A. The fiber array

uniformity, however, was much better in LBH-15A than in LBH-4. This, apparently, was due to the stability resulting from the increased size of the molten zone. Longitudinal sections of those samples, are presented in Figure III-12. In LBH-4, many small cells were nucleated and solidified early in the run and they gradually began to increase in size, with an associated decrease in number, until there were a few large cells at the top of the solidified zone. Sample LBH-15A, however, displayed the formation of larger cells relatively early in the solidification process, which remained more or less unaltered throughout the entire run. The enhanced stability reflected by the large continuous cells undoubtedly improved the fiber uniformity in experiment LBH-15A.

In order to produce uniform tungsten fiber geometries during the unidirectional solidification of  $UO_2$ -W ingots, it was necessary to establish a homogenous zone of liquid in the samples prior to the initiation of the solidification process. This was accomplished during the initial internal melting by increasing the input power to the sample until the molten zone size had been maximized and stabilized. However, when the lower molybdenum susceptor was raised into the bottom of the rf work coil to serve as a postheater and solidification-front cutoff point, the inductive field was drastically

(a)



(b)

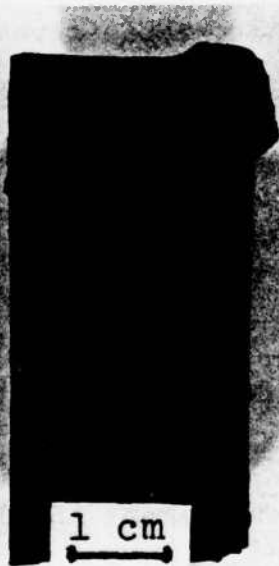


Figure III-12. Longitudinal Sections of (a) LBH-4, and (b) LBH-15A, Showing Variation of Cell Size with Position in Sample.

distorted. That apparently caused the solidification front to run upward in an uncontrolled fashion for a short distance, yielding numerous small cells and areas of primary  $UO_2$  at the bottom of the zone. The tungsten metal randomly precipitated as droplets in this region. As the solidification front slowed and stabilized, the average cell size increased to approximately 5 mm in diameter, and very uniform fiber geometries were obtained.

In an effort to eliminate this initial runaway situation, an upper molybdenum preheater was utilized in addition to the postheater to "pin" the molten zone in a 25 mm gap between the susceptors in experiment LBH-14. Post-run analysis of that sample revealed the presence of many small cells and few areas of continuous fiber growth. "Fan-banding", a situation apparently involving the repeated nucleation and extinction of fiber growth, was prominent throughout the solidified zone of this sample (Figure III-13).

The possibility that the discontinuous growth was due to a "sub-critical" size of the zone "pinned" between the susceptors led to experiment LBH-17, where the gap between the pre- and post-heaters was increased to 36 mm (from the 25 mm separation of LBH-14). Post-run analysis of LBH-17 revealed that the change had a minor effect on cell size, as the majority of cells were only

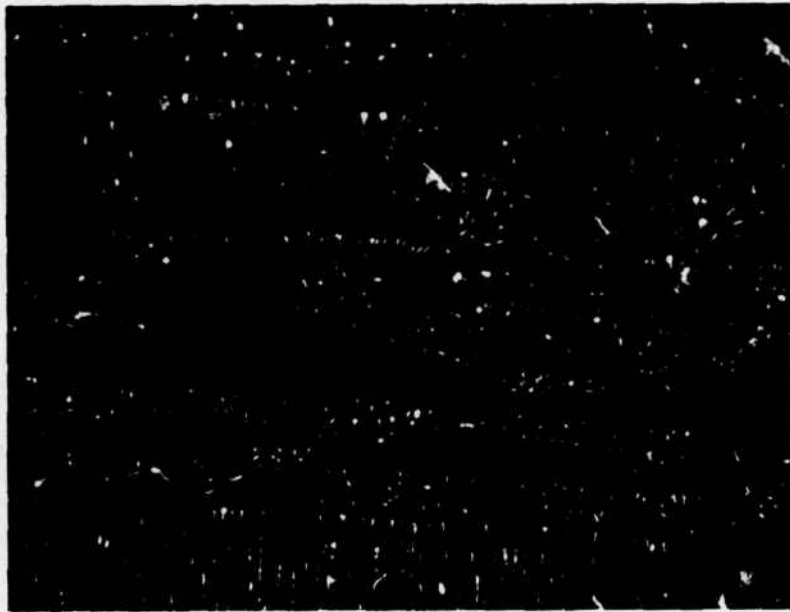


Figure III-13. Typical Area of "Fan-Banding", Apparently Involving the Repeated Nucleation and Extinction of Fiber Growth. Sample LBH-14; dark field, X542.

slightly larger than those seen in LBH-14. The previously seen "fan-banding" was also present, but the average distance between the nucleation and extinction of fiber growth was substantially increased (Figure III-14). Moreover, some cells were almost completely free of banding, and in some regions continuous fibers ran almost the entire length of the solidified zone. This general improvement in fiber growth suggests that this type of banding may be related to the size of the molten zone.

In the majority of experiments discussed in this report the growth procedure described in the Introduction (Section I) was employed. Briefly, this method consisted of heating the presintered ingot inside the Mo tube, lowering the Mo tube out of the rf coil, establishing a stable internal molten zone in the  $\text{UO}_2\text{-W}$  ingot, raising the Mo tube back up into the bottom turns of the rf coil to serve as a post-heater and slowly lowering the ingot into the stationary Mo tube to achieve unidirectional solidification. The use of this procedure established a large homogeneous molten zone, but it was plagued by the initial runaway solidification front problem as the Mo tube was raised to serve as a post-heater. Overheating of the ingot as the molten zone approaches the top of the pellet was also a problem. The double-susceptor configuration described in this section

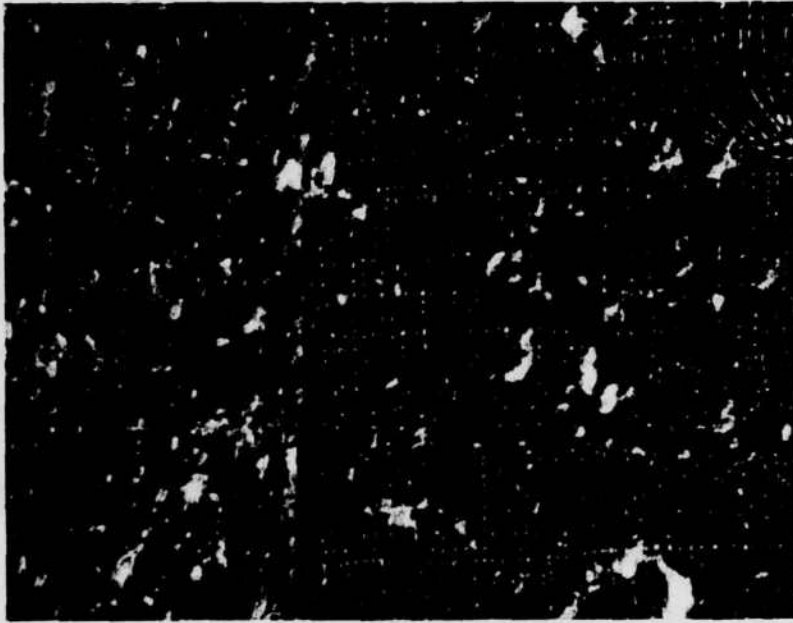


Figure III-14. Typical Area of "Fan-Banding" From LBH-17 Showing General Improvement in Fiber Lengths, dark field, X542.

offered more precise control over the translation of the molten zone, but apparently did not provide for the homogeneity necessary for continuous fiber growth.

An alternate approach was tested in conjunction with the effort to minimize composite cracking during growth (as discussed in the next section). In this procedure instead of lowering the pellet into the susceptor, the susceptor was slowly raised around the pellet, which helped alleviate the "run-away" condition. Limited testing suggests this method may offer some advantages; however, the danger of the Mo tube absorbing most of the rf power required careful control of the coil, Mo tube, and sample geometry.

#### G. CRACKING CHARACTERISTICS

Throughout the entire development of oxide-metal composite materials, cracking of the samples presented a critical problem to the utilization of these materials for many applications. For example, Sample LBH-4 (Figure III-12a), displayed a single, large crack along the right side of the solidified zone. Such fissures would hinder the fabrication of large-area cathodes, since such flaws frequently caused transverse sections to break in half. Increasing the size of the sample ingots from 16 to 25 to 32 mm in diameter provided larger usable composite areas, but did not appreciably alter the cracking characteristics. The cracking was undoubtedly due to the difference in contraction during cooling of

the internal solidified zone, and the external unmelted skin. In an attempt to overcome the problem, four 5 mm deep, 0.3 mm wide vertical grooves were made with a diamond blade at 90° intervals down the entire length of sample pellet LBH-6 before melting. It was hoped the gaps would provide room for the skin of the pellet to contract during cooling. Cracking appeared to be less severe in this sample but the shape and size of the molten zone was severely altered, especially near the gaps (Figure III-15). In a second experiment, LBH-9, the number of gaps was increased to eight. These grooves were wider (1 mm) than before, and tapered to 0.3 mm deep at the base, as cut by a dental burr. Post-solidification analysis of LBH-9 revealed that the major cracking occurred circumferentially, about two-thirds of the way from the center to the edge of the solidified zone. The circular shape of the molten zone was improved by the eight grooves, but the zone was greatly reduced in size, indicating that the loss of heat through the grooves was substantial. Extrapolation suggests that a large number of shallow grooves may improve the cracking characteristics of the UO<sub>2</sub>-W composite samples.



Figure III-15. Transverse View of Sample LBF-6, Showing Stress-Relief Gaps and Distorted Solidified Zone.

The slow growth rate, low fiber density samples, LBH-20 and -21 described in the solidification rate sub-section, displayed unique cracking properties. The central solidified zone remained intact and this zone was surrounded by a circumferential crack which permitted the easy removal of the unmelted "skin" material (Figure III-16). Evidently, the low growth rates used in these experiments (1.5 and 0.5 cm/hr) provided a very flat solidification front. In past experiments, the size of the cells decreased more or less uniformly from the center to the perimeter of the molten zone, but in LBH-20 and LBH-21 (Figure III-16) large cells were seen throughout the central core (growth region) of the sample. Apparently the reduced solidification rate and flat liquid-solid interface resulted in a stress pattern that produced the circumferential crack at the skin-central zone boundary. Obviously this behavior produced a very desirable crack pattern for the maximum utilization of the composite ingots.

#### H. SUMMARY OF COMPOSITE GROWTH PROCEDURES

In the previous sections a description of the parameters that control the successful growth of the  $UO_2$ -W composites has been presented. The processing steps for the unidirectional solidification of the  $UO_2$ -W samples is shown as a flow sheet in Figure III-17.

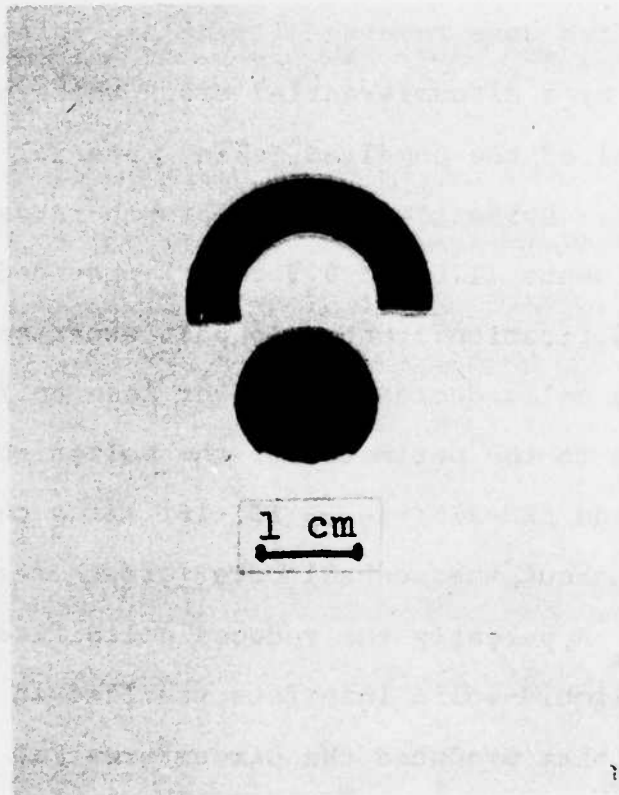


Figure III-16. Sample LBH-21 Showing "Crack-Free" Central Solidified Zone and Part of the Separated "Skin" Material.

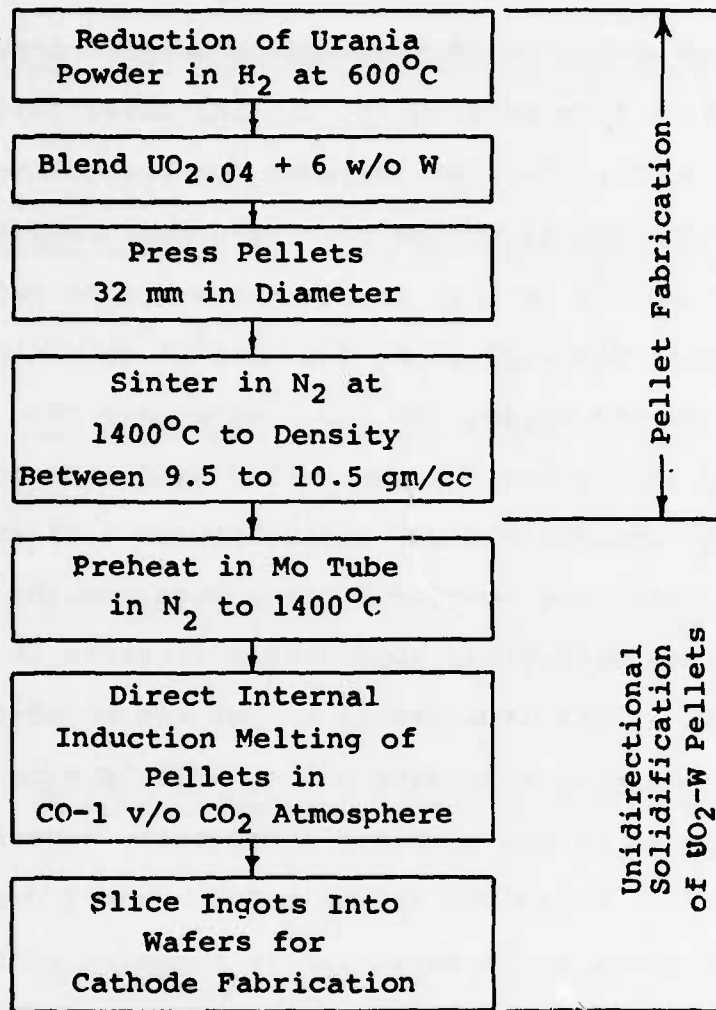


Figure III-17. Flow Sheet for the Fabrication of UO<sub>2</sub>-W Composites.

A brief description of these basic steps follows. Some information from Section II, the characterization of the  $\text{UO}_2$  powder, is also included for completeness.

Since typical urania powders possess a variety of starting O/U ratios, it was necessary to reduce all of this material in  $\text{H}_2$  (at  $\sim 600^\circ\text{C}$ ) to yield the stoichiometric oxide,  $\text{UO}_{2.00}$ . The powder then was quenched in dry ice for controlled oxidation to obtain a reproducible O/U ratio between 2.04 and 2.07. This material can be stored for several months in desiccators without an appreciable increase in the O/U ratio. Next, the urania powder was blended with 6 w/o tungsten. Excessive mixing efforts were not necessary to assure complete homogeneity because the tungsten was dissolved in the molten urania during growth and any small variation in tungsten content was completely eliminated in the process. Standard uniaxial pressing in steel dies was used to form "green" (unsintered)  $\text{UO}_2\text{-W}$  pellets (32 mm in diameter). Pellets between 7 and 8 cm tall were utilized because at lengths longer than this the void generated during the unidirectional solidification grew excessively large and hindered the melting of additional material from the roof of the cavity. Importantly, the total length can be made of 2 pellets as the internal zone will melt very smoothly through the interface between the pellets

and yield one solidified ingot after zone travel.

The pellets were sintered in  $N_2$  at  $1400^{\circ}C$  for several hours to achieve densities between 9.5 and 10.5 g/cc. During sintering the accompanying shrinkage decreased the diameter to about 25 mm. Often, non-uniform shrinkage produced some "hour-glassing" at the base of the pellet and hand grinding of the pellets was required to obtain the desired dimensional tolerances.

The growth facility shown in Figure I-1 remained basically unchanged during all of the solidification experiments. The sintered pellets were heated in a  $N_2$  atmosphere inside the molybdenum tube from room temperature to  $1400^{\circ}C$  in 60 to 90 minutes. Utilization of the  $N_2$  atmosphere kept the oxide hyperstoichiometric and facilitated the direct internal rf melting. The Mo preheat tube was lowered out of the induction coil and, using careful control of the rf power, the sample was internally melted. The power was slowly increased after initial melting to increase the size of the molten zone. Stabilization of the internal liquid-solid geometry required 15 to 20 minutes. Also, immediately after the direct melting of the  $UO_2$ -W pellets, the atmosphere was switched to CO-1

v/o  $\text{CO}_2$ . When a stable molten zone was achieved the molybdenum tube was raised back up into the bottom one or two turns of the rf coil and the sample lowered into this tube at rates of 2 to 4 cm/hr. After 75% of the  $\text{UO}_2$ -W pellet was inside the Mo tube, the run was complete (because the top of the ingot contained the void) and the lowering was stopped. Cooling to room temperature was accomplished in several hours by slowly decreasing the rf power. In numerous  $\text{UO}_2$ -W solidification experiments conducted in this and other projects it has been found that the cracking characteristics were relatively insensitive to the rate of cooling. After removal from the growth facility a sample was sectioned into wafers for the fabrication of the field emission cathodes. The description of the brazing and etching procedures for the  $\text{UO}_2$ -W composites is described in the next section.

## SECTION IV

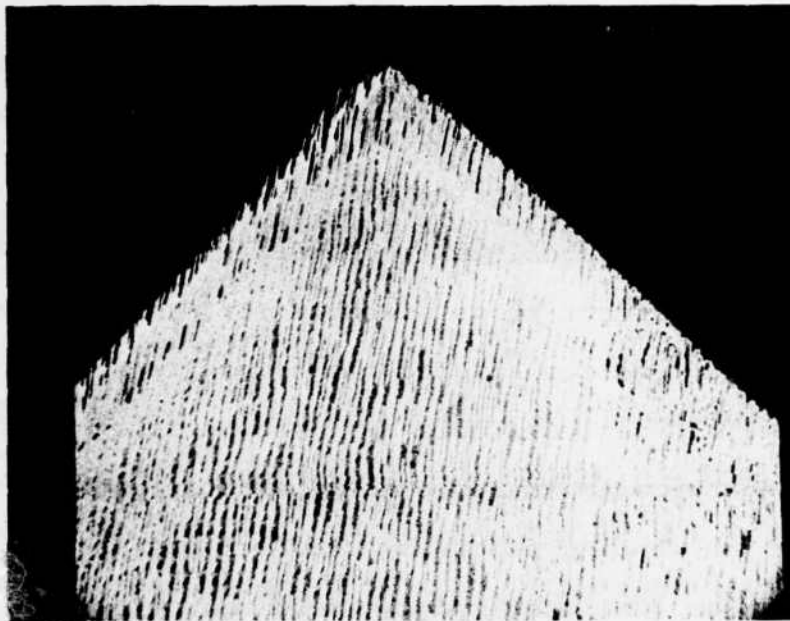
### MACHINING, BRAZING, AND ETCHING TECHNIQUES FOR EMITTERS

The purpose of this section was to develop machining, brazing, and etching techniques necessary for forming  $\text{UO}_2$ -W composites into configurations suitable for use as electron emitters. Procedures for slicing the composite into wafers, brazing the wafers onto suitable high vacuum materials, machining the composite into desirable emitter geometries, and exposing and shaping fibers by chemical etching and ion milling have been developed and are reported below.

#### A. MACHINING

Development of techniques for slicing and machining  $\text{UO}_2$ -W composites was not necessary, as conventional ceramic machining and slicing techniques were successful in fabricating shapes. The unidirectionally solidified  $\text{UO}_2$ -W boules were sliced into wafers as thin as 0.25 mm using a low speed diamond saw. Wafers, brazed to metal bases, were machined in a small lathe using rotating silicon carbide and diamond tools for grinding to desired shapes. Styluses, i.e. pointed cones, were routinely ground to cone angles of  $60^\circ$ - $90^\circ$  with cone apex radii of  $\sim 5 \mu\text{m}$ . Examples of machinability are shown in Figures IV-1 and IV-2, where a  $90^\circ$  cone with a  $5 \mu\text{m}$  apex radius and a  $72^\circ$  cone with a  $25 \mu\text{m}$  apex radius are presented.

(a)



(b)

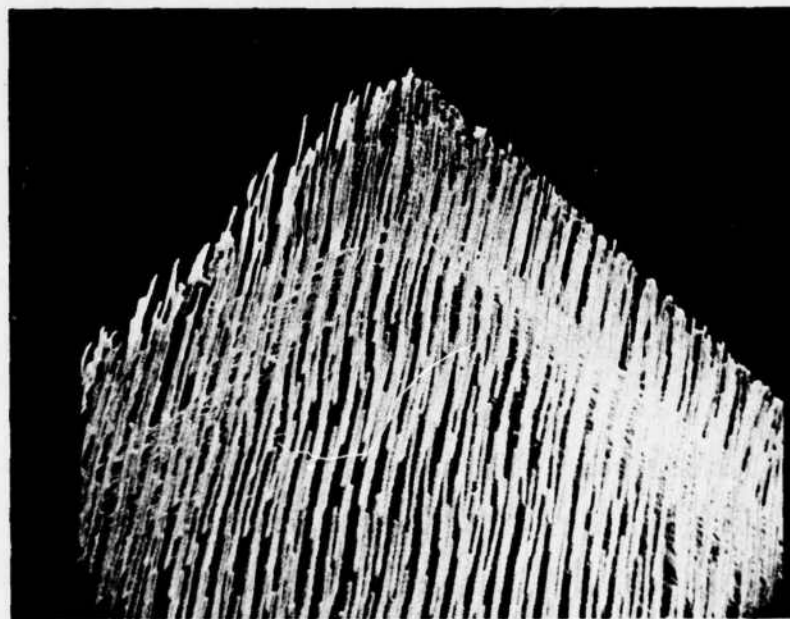
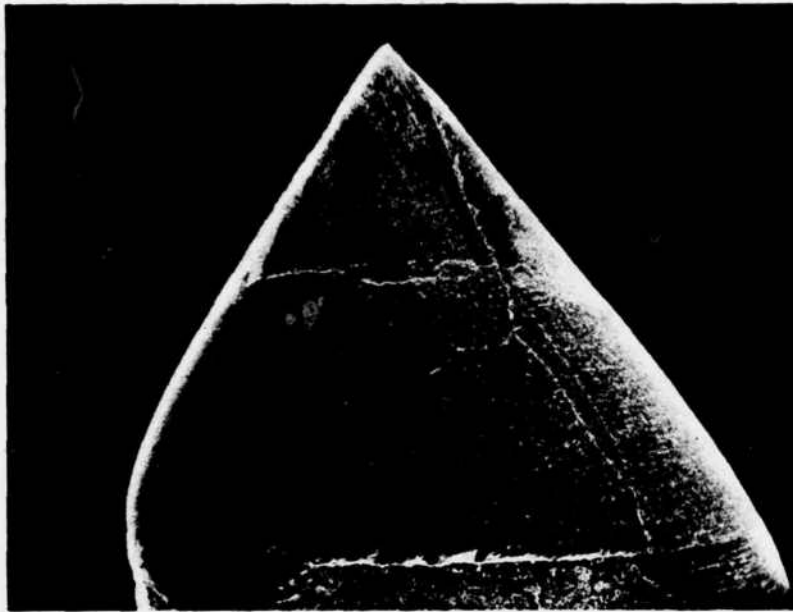


Figure IV-1. Machined  $\text{UO}_2\text{-W}$  Composite Stylus with  $90^\circ$  Cone Angle and  $52\ \mu\text{m}$  Apex Radius, Etched to Expose Tungsten Fibers; (a) X575 and (b) X1200,  $90^\circ$  From Cone Axis.

(a)



(b)

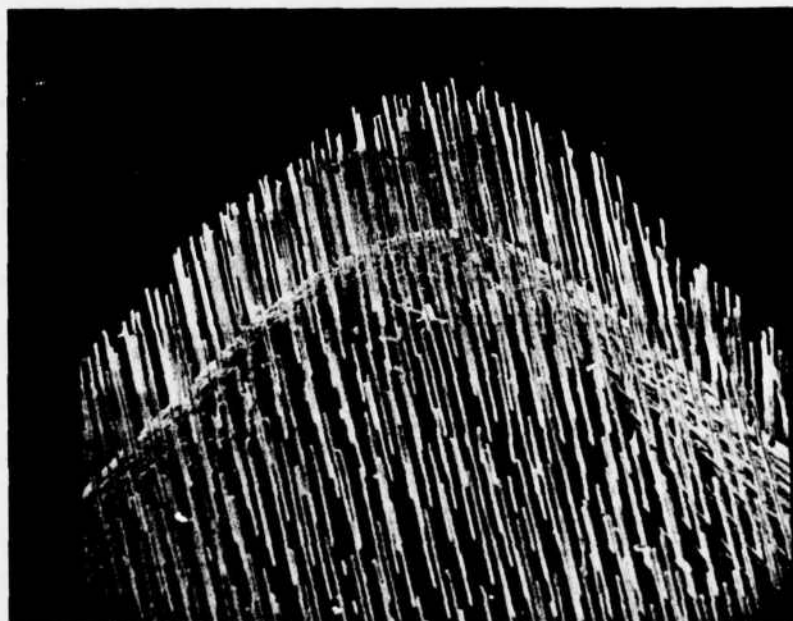


Figure IV-2. Machined UO<sub>2</sub>-W Composite Stylus with 72° Cone Angle and 25 μm Apex Radius, Etched to Expose Tungsten Fibers; (a) X62 and (b) X1200, 90° From Cone Axis.

It should be noted that the  $\text{UO}_2$ -W composites are friable and weak in tension so that machining had to be performed with care, i.e. using small-grained grinding tools and machining in increments of a few mils at a pass. It was also necessary that the wafers be brazed or glued on a substrate for machining, as the strength was insufficient for mechanical clamping. Developing an adequate braze-substrate combination was important to sample fabrication as well as high vacuum requirements, and a strong effort was made in brazing techniques.

#### B. BRAZING

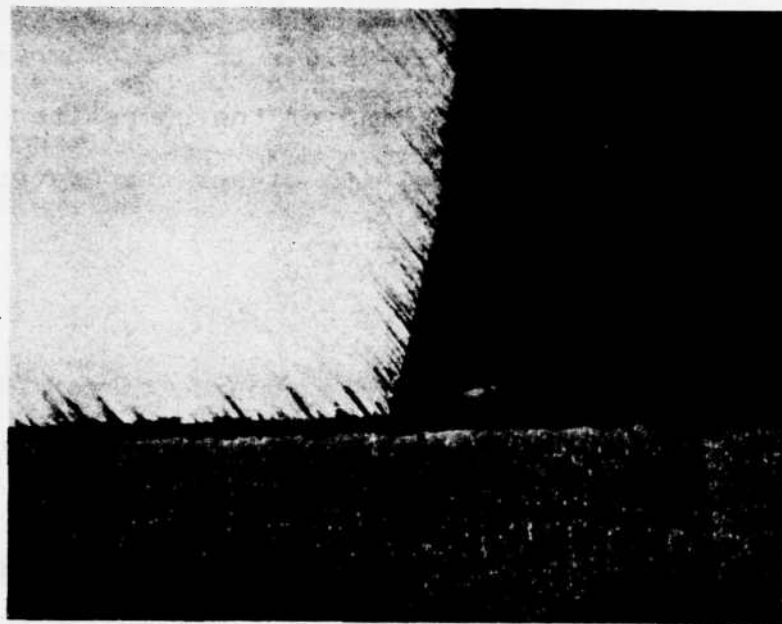
The purpose of the work reported in this section was to select a metal substrate material compatible with the  $\text{UO}_2$ -W composite and to develop a braze for joining the two. The substrate material had to be suitable for high temperature and high vacuum application, and also had to provide an acceptable thermal expansion match. Since  $\text{UO}_2$ -W composites are weak in tension perpendicular to the growth direction, it was desirable to have the thermal expansion of the substrate slightly higher than that of the composite so the composite would be under a slight compressive stress after cooling from the brazing temperature. At the start of this program,  $\text{UO}_2$ -W composites were being joined to molybdenum using a copper braze. This brazing procedure

was reliable but the thermal expansion of molybdenum is much lower than that of the  $\text{UO}_2\text{-W}$  ( $5.0 \times 10^{-6}/^\circ\text{C}$  compared to  $10.5 \times 10^{-6}/^\circ\text{C}$ ) and microcracking of the composite resulted. Additionally, a braze with higher temperature capability than copper was desired.

#### 1. Braze Materials

The higher temperature materials considered for brazes were cobalt, nickel, titanium, and 50/50 w/o Mo-Ni. To test the wettability and adherence of these materials, sessile drop tests were conducted on  $\text{UO}_2\text{-W}$  composite substrates. Copper was also included in the tests for comparison. Small pieces of the metals were placed on  $\text{UO}_2\text{-W}$  wafers which had been polished to a one micron diamond finish perpendicular to the W fibers. The wafers and braze materials were each heated in an rf furnace in a  $\text{H}_2$  atmosphere until the metal melted. After the metal had been held molten for 15 minutes, the sample was cooled, sectioned through the center of the sessile drop perpendicular to the braze-composite interface, and polished. Contact angles were measured from micrographs (Figure IV-3), and are reported in Table IV-I along with melting temperatures. Microscopic examination of the braze-composite interfaces revealed that all of the braze materials joined the composite with few discontinuities. The largest variation was seen in

(a)



(b)

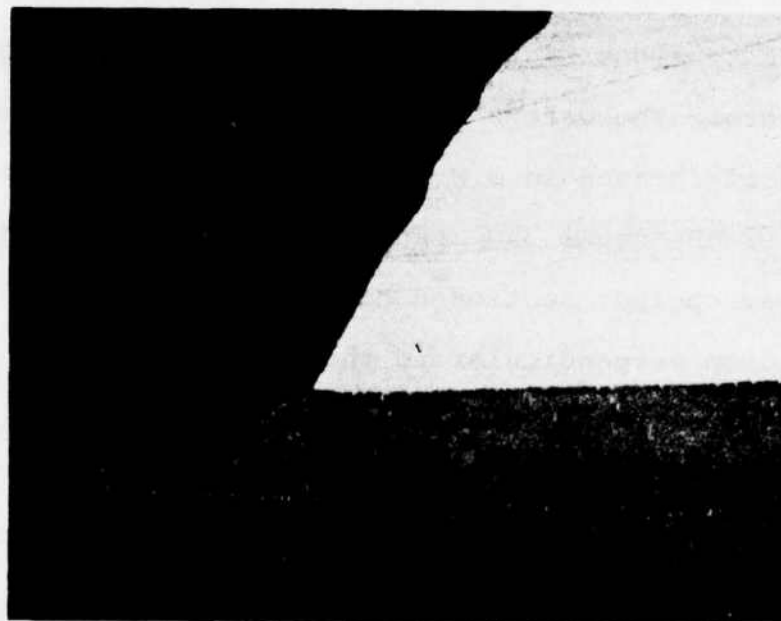


Figure IV-3. Reflected Light Micrographs of (a) Mo-Ni and (b) Ni Sessile Drops on  $UO_2$ -W Composites Showing  $100^\circ$  and  $60^\circ$  Contact Angles Respectively, X200.

Table IV-I. Melting Temperatures and  $\text{UO}_2$  Contact Angles for Various Braze Materials.

Material	Melting Temperature ( $^{\circ}\text{C}$ )	Contact Angle* on $\text{UO}_2$ -W
Copper	1050	100 $^{\circ}$
Mo-Ni	1350	100 $^{\circ}$
Nickel	1450	60 $^{\circ}$
Cobalt	1495	100 $^{\circ}$
Titanium	1660	0 $^{\circ}$

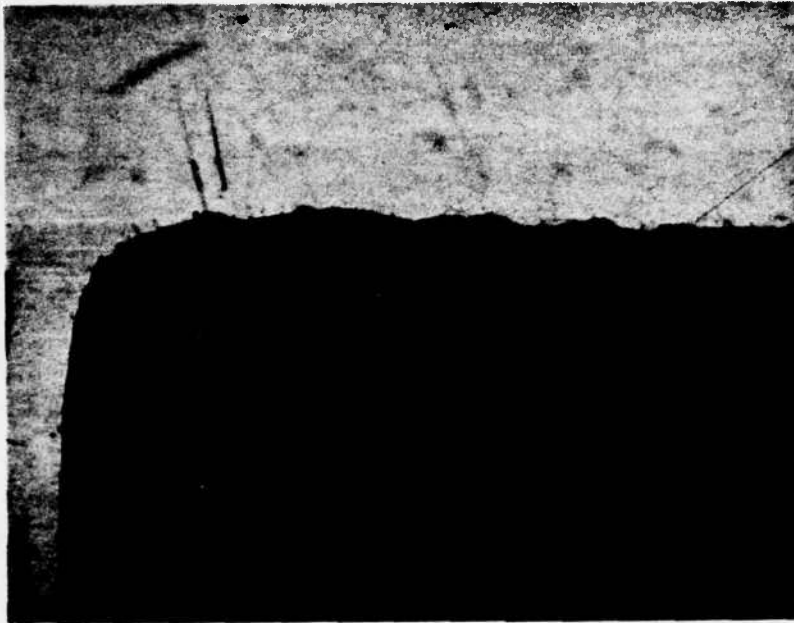
\* Angle measured through metal.

wetability, as evidenced by contact angle. Copper, cobalt, and Mo-Ni all had contact angles of  $100^{\circ}$ , indicating poor wetability. (Note that poor wetability does not necessarily imply poor adhesion.) Titanium, with a  $0^{\circ}$  contact angle, apparently reacted with the  $UO_2$  and spread over the surface of the wafer. The wetting of the nickel was the most encouraging. It spread to a contact angle of  $60^{\circ}$  and produced a continuous interface with the composite (Figure IV-4). From the sessile drop tests, and brazing tests described below, nickel proved to be the best braze of those tested.

## 2. Substrate Materials

When a thin braze is used, the thermal expansion of the substrate material controls the stress on the  $UO_2$ -W composite on cooling from the brazing temperature. Thus, substrate materials selection was initially based on thermal expansion and limited to materials with melting points of  $1400^{\circ}C$  or higher. Thermal expansion values from the literature were used to construct a comparative graph of the candidate materials: Ni, Co, Cr, Ti, Ti-7Al-4Mo, and the 300-series stainless steels (Figure IV-5). Nickel, cobalt, chromium, and 300-series stainless steels all have considerably greater thermal expansion than  $UO_2$ . Titanium and titanium alloys appeared to have the most acceptable

Ni



UO<sub>2</sub>-W

Figure IV-4. Reflected Light Micrograph of Ni Braze - UO<sub>2</sub>-W Composite Interface Showing a Continuous Void Free Join, X200.

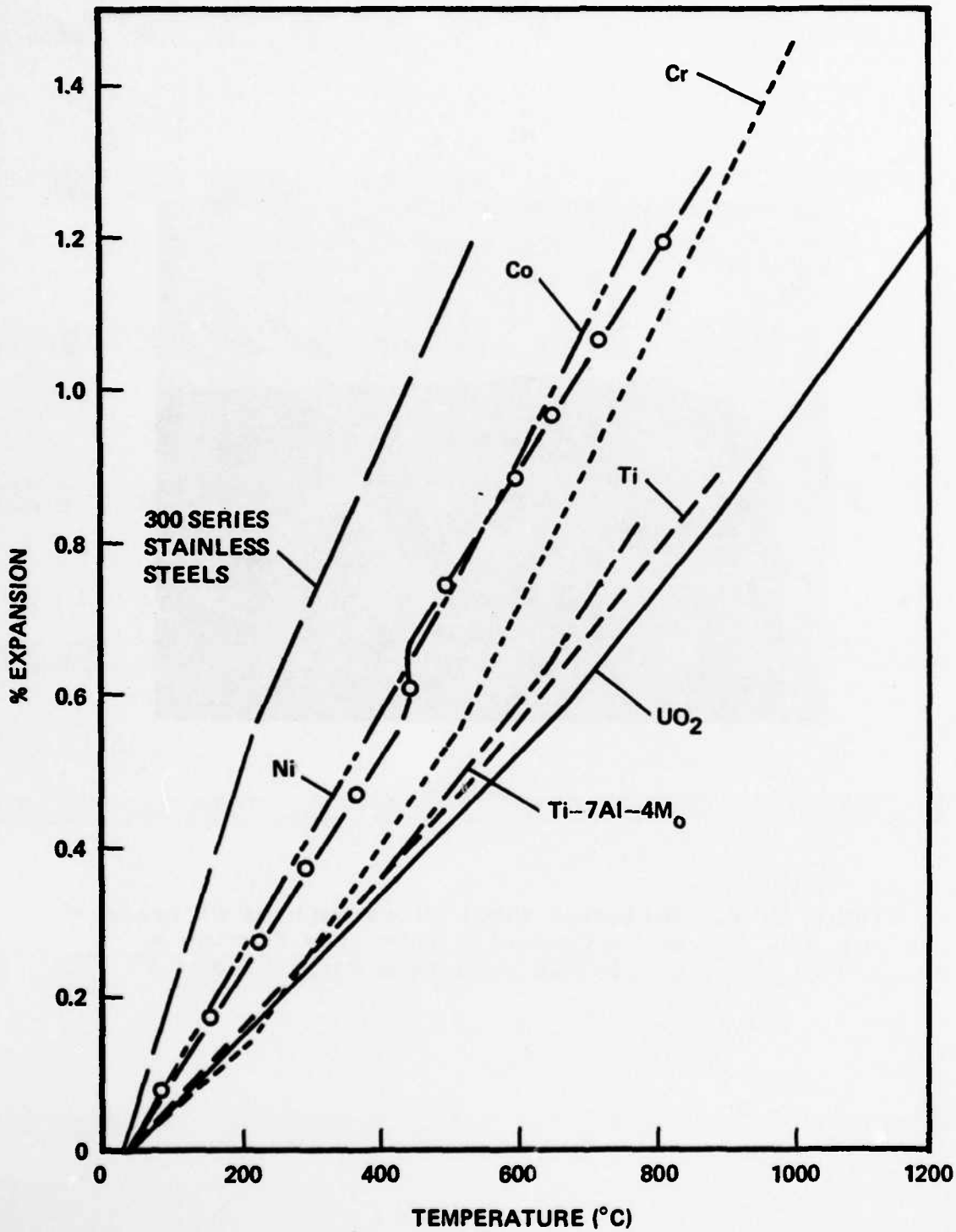


Figure IV-5. Thermal Expansions for Various Candidate Substrate Metals Compared to UO<sub>2</sub>-W Composites.

thermal expansion match with  $\text{UO}_2$ . Later in the program, vanadium, aluminum oxide ( $\text{Al}_2\text{O}_3$ ), and 410 stainless steel were added to the list of candidate substrate materials.

### 3. Braze-Substrate Combinations

During the program a number of braze-substrate combinations were attempted, with various degrees of success. A summary of the combinations investigated are noted in Table IV-II and each will be discussed below. The substrate materials tested included titanium, vanadium,  $\text{Al}_2\text{O}_3$ , 410 SS and tungsten; the braze materials were copper and nickel. Comparative expansions for these materials are shown in Figure IV-6. The curves shown for titanium,  $\text{UO}_2$ -W, and 410 SS were measured with an automatic dilatometer while the remaining are literature values.

#### 3.1 Copper-Titanium

The expansion of titanium was approximately  $3 \times 10^{-6}/^\circ\text{C}$  greater than that of  $\text{UO}_2$ -W up to  $880^\circ\text{C}$ , and at  $890^\circ\text{C}$  titanium undergoes an  $\alpha+\beta$  phase transformation with 0.22% linear contraction. In all of the brazing trials with Ti, the  $\text{UO}_2$ -W wafer crumbled to a powder during cooling of the sample. This was undoubtedly due to the destructive expansion of the  $\alpha+\beta$  transformation on cooling and to excessive reaction between the  $\text{UO}_2$  and titanium. Thus titanium was eliminated as a suitable substrate.

Table IV-II. Summary of Braze-Substrate Combinations Investigated for Joining to  $UO_2$ -W Composites.

Substrate	Braze	$a_s$ ( $10^{-6}/^{\circ}C$ )	$a_b$ ( $10^{-6}/^{\circ}C$ )	Brazing Temperature ( $^{\circ}C$ )	Comments
Titanium	None	14.6	--	1670 $^{\circ}C$	Too reactive with $UO_2$ . Titanium has a destructive phase inversion.
Titanium	Copper	14.6	20	900 $^{\circ}C$	
Vanadium	Copper	12-13	20	1250 $^{\circ}C$	Vaporization of copper
Vanadium	Nickel	12-13	15	1300 $^{\circ}C$	V reaction with $UO_2$
$Al_2O_3$	Nickel	8.8	15	1550 $^{\circ}C$	Excellent adherence
Tungsten	Nickel	5	15	1550 $^{\circ}C$	OK with thick braze layer
410 SS	Copper	11.5	20	1000 $^{\circ}C$	OK but tricky due to eutectic liquid formation

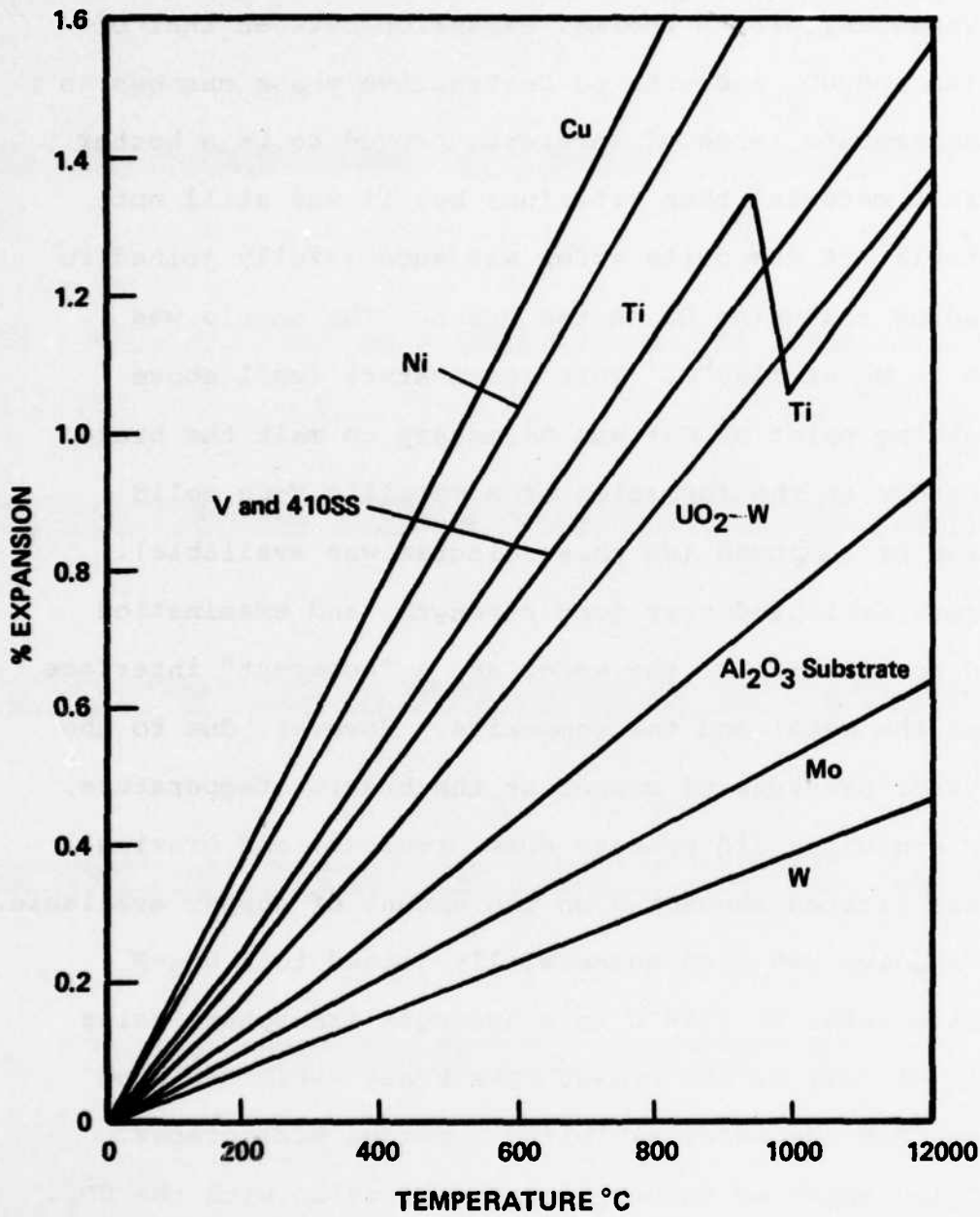


Figure IV-6. Comparative Thermal Expansion of Materials Used for Braze-Substrate Combinations with UO<sub>2</sub>-W Composites.

### 3.2 Copper-Vanadium and Nickel-Vanadium

Vanadium, with a thermal expansion between that of titanium and  $UO_2$  and with no destructive phase changes in the temperature range of interest, proved to be a better substrate material than titanium; but it was still not acceptable. A composite wafer was successfully joined to a vanadium rod using Cu as the braze. The sample was brazed in  $H_2$  at  $1250^{\circ}C$ . This temperature (well above the melting point of Cu) was necessary to melt the braze, perhaps due to the formation of a metallic V-Cu solid solution or compound (No phase diagram was available). The braze exhibited very good strength, and examination showed no cracking of the wafer and a "coherent" interface between the metal and the composite. However, due to the high vapor pressure of copper at the brazing temperature, copper evolution did present some problems, and brazing time was limited depending on the amount of copper available.

Vanadium was also successfully joined to a  $UO_2$ -W composite wafer at  $1124^{\circ}C$  in a hydrogen atmosphere using 0.5 mil Ni foil as the braze. The braze exhibited good strength but the wafer exhibited numerous microcracks. There also appeared to be excessive reaction with the  $UO_2$ .

Although vanadium did show some promise as a substrate material, experiments with vanadium were discontinued for both economic and technical reasons. Vanadium at present

prices cost ~\$100/lb and is difficult to obtain in small quantities. Furthermore, delivery times of a minimum of six months were quoted for a new order.

### 3.3 Nickel-Al<sub>2</sub>O<sub>3</sub>

The most successful substrate-braze combination, particularly for future mozaic structures of larger areas, proved to be Al<sub>2</sub>O<sub>3</sub>-Ni. Alumina was selected as a substrate candidate because of excellent high temperature vacuum capability, reasonable thermal expansion match ( $7.8 \times 10^{-6}/^{\circ}\text{C}$  compared to  $10.5 \times 10^{-6}$  for UO<sub>2</sub>-W), and economical availability in a wide variety of shapes. Nickel was selected because of the favorable sessile drop test. For all nickel brazing Nickel 200 alloy was used.

Nickel was melted on alumina in a H<sub>2</sub> atmosphere and showed no adverse reaction. On an unpolished, high density, fine grain alumina substrate, Ni formed a contact angle slightly less than 90°. A UO<sub>2</sub>-W wafer was brazed with Ni to Al<sub>2</sub>O<sub>3</sub> and good bonding was observed at both the UO<sub>2</sub>-W-Ni and Ni-Al<sub>2</sub>O<sub>3</sub> interfaces (Figure IV-7). Thus, the braze-substrate combination does work and provides support for the composite. In another experiment a sheet of Ni, 1.0 x 1.0 x 0.076 cm, was sandwiched between a 1.43 μm diameter UO<sub>2</sub>-W wafer and an alumina substrate. After melting in a H<sub>2</sub> atmosphere, the Ni formed a continuous layer between

AD-A148 435

MANUFACTURING METHODS FOR THE PRODUCTION OF FIELD  
EFFECT ELECTRON EMITTERS FROM OXIDE-METAL COMPOSITES

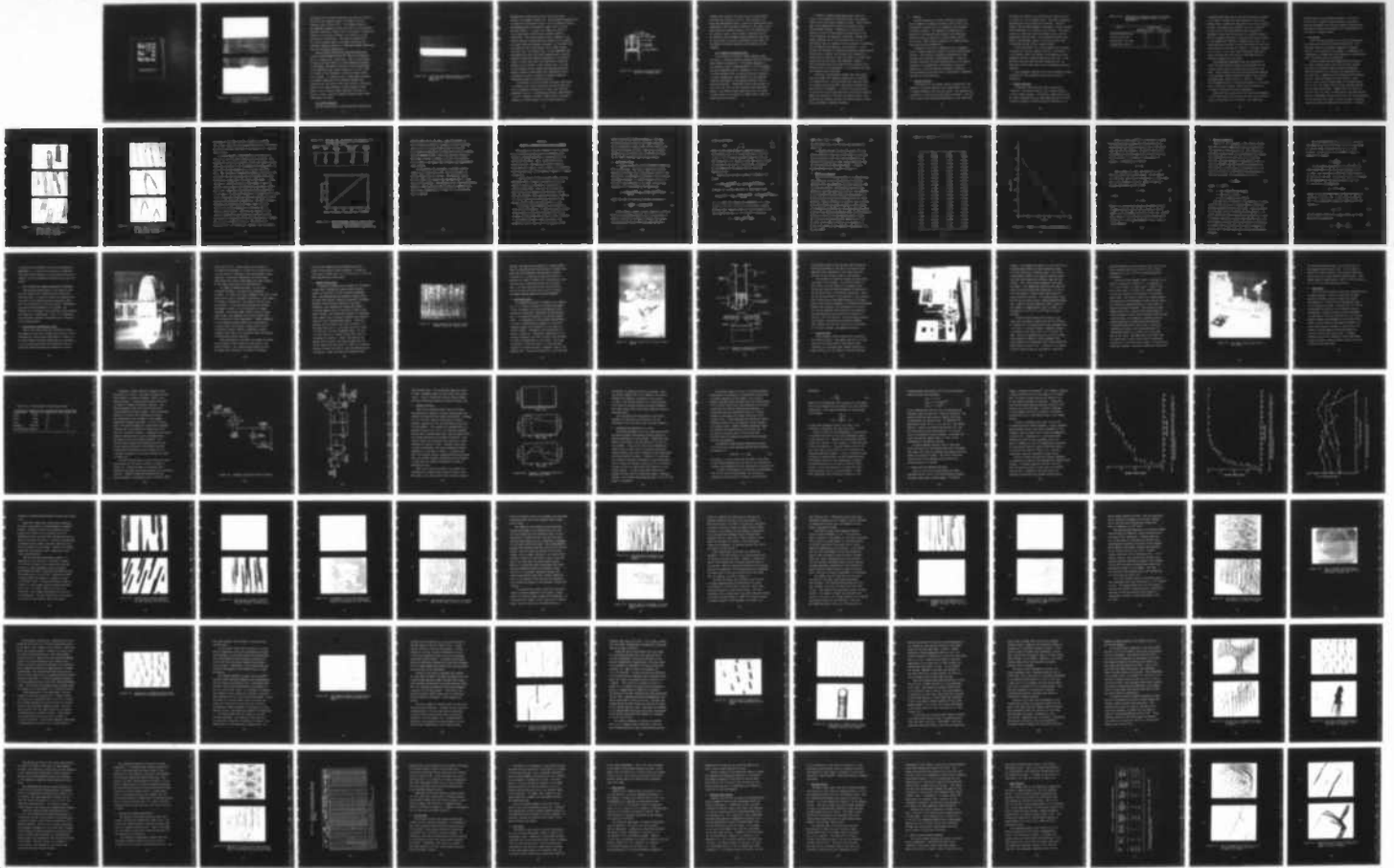
2/3

UNCLASSIFIED

DAAH01-75-C-0852

F/G 9/1

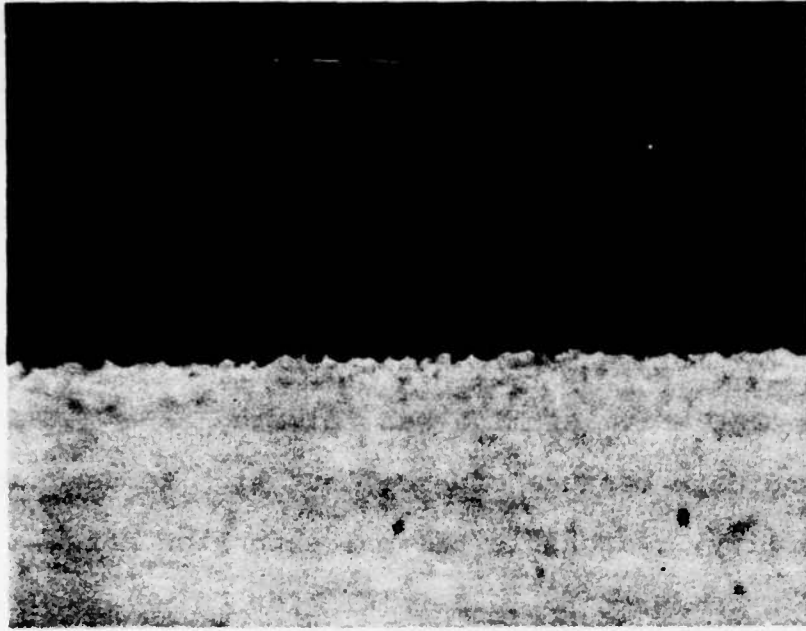
NL





MICROCOPY RESOLUTION TEST CHART  
NATIONAL BUREAU OF STANDARDS-1963-A

(a)



(b)

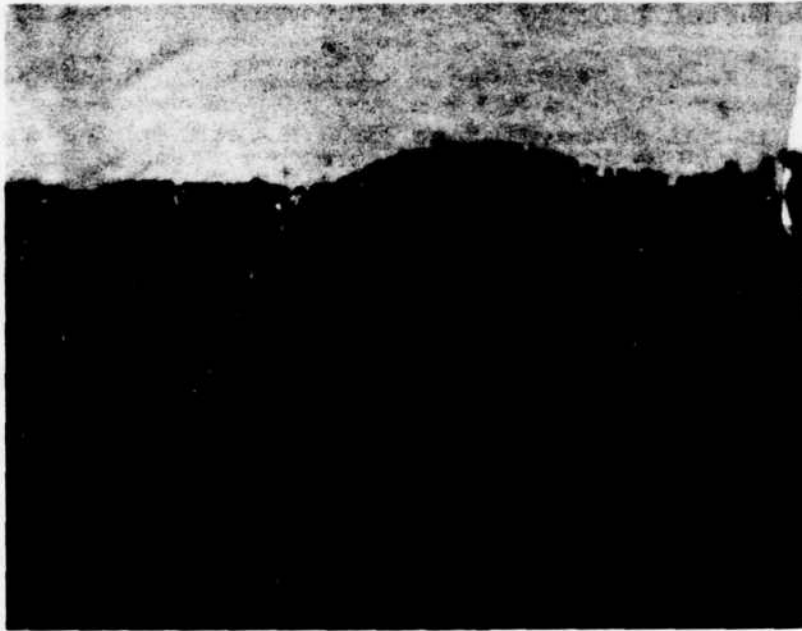


Figure IV-7. Reflected Light Micrographs of (a)  $\text{Al}_2\text{O}_3$ -Ni Interface and (b) Ni- $\text{UO}_2$ -W Composite Interface, X545.

the wafer and the alumina substrate; the layer was 0.056 cm thick and just slightly smaller in diameter than the composite wafer (Figure IV-8). The tungsten fibers in the composite appeared to alloy with the Ni, thus providing excellent electrical contact; and a third phase, unidentified, formed at the Ni-Al<sub>2</sub>O<sub>3</sub> interface, and seemed to enhance the bonding at that point. The relative simplicity of this brazing method makes it extremely attractive for attaching composite emitters to large-area alumina substrates, which are available commercially.

Because nickel wets both the UO<sub>2</sub>-W and Al<sub>2</sub>O<sub>3</sub> with contact angles between 50° and 90°, there is no tendency for Ni to spread over a large area. Thus, by positioning the Al<sub>2</sub>O<sub>3</sub> and UO<sub>2</sub>-W wafer at a fixed separation distance, a considerable thickness of molten Ni can be maintainable in the separation gap, often as much as 3 or 4 mm. With a Ni braze of this thickness, electrical contact would be no problem. In addition, with a large braze thickness, the thermal expansion of the substrate becomes less important and the stress on the UO<sub>2</sub>-W wafers is controlled mainly by the braze-composite thermal expansion match. Nickel, with a slightly higher expansion than that of UO<sub>2</sub>-W, is ideal, since the composite remains under slight compression on cooling.

### 3.4 Nickel-Tungsten

Further investigation of braze-substrate combinations

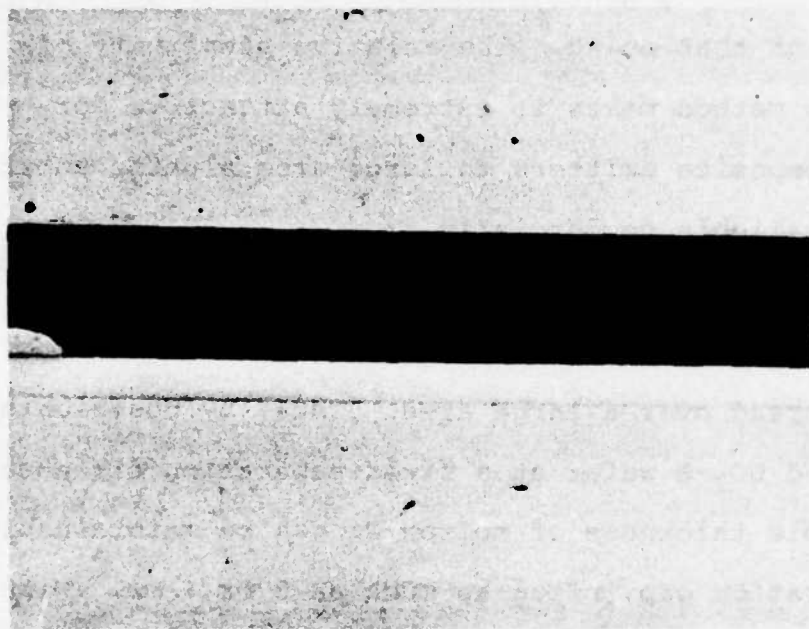


Figure IV-8.  $\text{UO}_2$ -W Composite Wafer Brazed to an  $\text{Al}_2\text{O}_3$  Substrate with a 0.056 cm Thick Ni Braze, X8.

revealed that nickel may be used to braze the  $\text{UO}_2$ -W emitter to a tungsten support rod. The jig shown schematically in Figure IV-9 was used to hold a 0.317 cm diameter tungsten rod perpendicular to the emitter sample and at a fixed distance above it. A piece of Ni sheet was placed on top of the emitter and the whole assembly heated to 1500-1550°C. The nickel melted to form a droplet on the emitter surface, making electrical contact to the tungsten pin array, which was exposed by etching. At the same time, the center of the nickel droplet rose to make contact, and alloy with, the tungsten rod. If the temperature was maintained just above the nickel melting point, then the tungsten rod did not dissolve excessively in the molten nickel, and yet there still was sufficient interaction between the two metals to form a strong bond. The end of the tungsten rod was placed some distance above the emitter surface so that there was a sufficiently thick interlayer of nickel to absorb any thermal expansion difference between the tungsten and  $\text{UO}_2$ .

To determine if the low thermal expansion coefficient of tungsten might cause cracking of the  $\text{UO}_2$ -W wafer even with a reasonable thickness of Ni braze, the following experiment was run. A polished  $\text{UO}_2$ -W wafer, approximately 1.42 cm in diameter and about 0.089 cm thick, was photographed at a magnification of x8 and then brazed to a

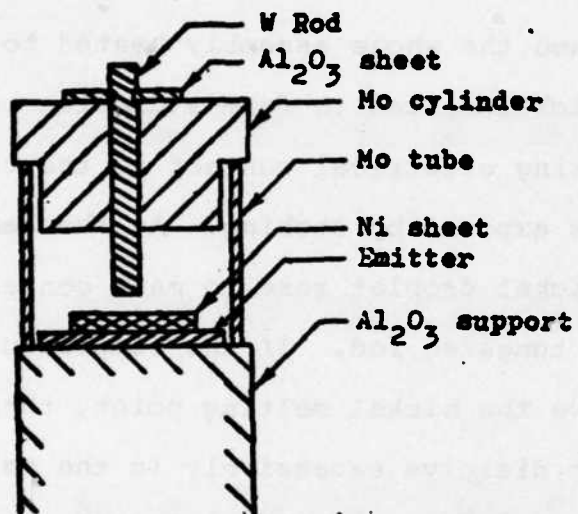


Figure IV-9. Jig Used to Ni Braze Field Emitter to Tungsten Rod.

tungsten rod, leaving a Ni layer 0.287 cm thick between the wafer and the end of the rod. After brazing, the wafer was photographed again at about the same magnification. Comparison of the two photos revealed no new cracks in the wafer after the brazing operation, nor any lengthening of the existing cracks. This behavior indicates that the Ni provides a very favorable thermal expansion match with the  $\text{UO}_2$ -W wafer, and that a sufficiently thick layer of Ni absorbs the thermal expansion match between  $\text{UO}_2$  and tungsten.

### 3.5 Copper-410 Stainless Steel

In an attempt to provide a closer expansion match for  $\text{UO}_2$ -W, a literature search indicated that 410 stainless steel should be compatible. The thermal expansion of 410 stainless steel is approximately  $13 \times 10^{-6}/^\circ\text{C}$  whereas the  $\text{UO}_2$ -W composites have an expansion of  $10.5 \times 10^{-6}/^\circ\text{C}$ . It was anticipated that, by placing the  $\text{UO}_2$ -W composite in slight compression, some reduction of the composite cracking attributed to the expansion mismatch with Mo should be observed. Preliminary results using copper as the braze with 410 SS as the substrate were encouraging. However, the copper reacted extensively with the steel, so that control of the amount of copper used to make the braze joint was critical.

A number of brazing experiments, were carried out using 0.32 cm diameter 410 stainless steel rods copper-brazed to the oxide-metal composite wafers. After brazing, many of the samples were ground and polished to form stylus-shaped cathodes. Examination of the polished surfaces of most of these samples revealed some of the grain boundaries had apparently separated. Because the larger expansion of the 410 stainless steel, it was anticipated that the composite would be placed in compression, thus minimizing the formation of microcracks. It was thought that perhaps the temperature gradients present during the heating or cooling could produce this cracking; so brazing cycles lasting as long as 24 hours, with very slow heating and cooling cycles were employed. However, the microcracks were still present and the source of the cracks has yet to be determined. It is possible that they were present prior to brazing.

Successful stylus-shaped cathodes were fabricated, using the copper-410 stainless combination, by reducing the composite size. The  $\text{UO}_2$ -W wafer was initially glued to a plastic rod and ground to form small cylinders less than 0.254 cm in diameter. A 0.254 cm hole was drilled in the end of the 410 stainless steel rod and the composite sample was inserted in the hole and copper brazed. This minimized the cracking problem and provided several "sound" stylus cathodes for emission testing.

### C. ETCHING

The main objective of etching the  $UO_2$ -W composites was to expose the tungsten pins above the  $UO_2$  matrix and to provide a variety of pin tip geometries for purposes of emission testing. The exposed-pin geometries of a majority of the emission test samples were produced by chemical etching as reported in several ARPA reports<sup>2</sup>. For clarity, these etching procedures are restated below, along with the etch composition.

Rounding of the tips of exposed pins was attempted using a thermal annealing process on several nickel-brazed samples. Unfortunately, excessive contamination of the tungsten pins resulted, as discussed below. A new and promising technique that was developed for pin tip shaping appeared to be reproducible and provided a variety of geometries. This new approach consisted of argon ion milling exposed cylindrical pins. The variety of geometries available is detailed below.

#### 1. Chemical Etching

The majority of the samples emission tested had a pin geometry of pointed tungsten fibers approximately 8-10  $\mu m$  in length extending above the  $UO_2$  matrix. This geometry was produced by a two-step selective etching process.<sup>2</sup> Starting with a  $UO_2$ -W wafer polished perpendicular to the fiber axes

the wafer was rotated in the pointing etch (Table IV-III) at 20 rpm in a 2.0 cm radius circle. The wafer surface was perpendicular to the direction of rotation. After 30 minutes, the resulting geometry consisted of conical pointed fibers extending 2.5  $\mu\text{m}$  above the  $\text{UO}_2$  surface. The second step was an identical etching procedure except that the lengthening etch was used. The lengthening etch has been shown to consistently remove 7-9  $\mu\text{m}$  of  $\text{UO}_2$  matrix with no detectable attack on the tungsten fibers.

It has been shown<sup>2</sup> that the lengthening etch removes the matrix at a fairly constant rate of 0.3  $\mu\text{m}/\text{minute}$ . In a few emission tests, the length of the exposed pins was purposely varied by varying lengthening etch time. A few emission tests were also run with cylindrical pin tip geometries, and in this case only the lengthening etch was employed.

A more complete analysis of the various chemical etches available for fiber geometry control may be found in reference 2.

## 2. Thermal Annealing

A relatively long period of time is required to "condition" the emitter before it will operate stably at a useful current density. Furthermore, observation of the pin tips of samples that have been operating for 1000 hours or more at gradually increasing current densities up to

Table IV-III. Composition of Chemical Etches for Pointing and Lengthening Tungsten Fibers in  $UO_2$ -W Composites.

Acid	Volume Ratios	
	Lengthening Etch	Pointing Etch
Saturated Aqueous $CrO_3$	40.0	30.0
Glacial Acetic Acid	20.0	20.0
Concentrated (70%) $HNO_3$	6.0	14.0
Concentrated (49%) $HF$	4.0	11.6

1 amp/cm<sup>2</sup> showed that many of the tips have become rounded. In an effort to reduce the time required for the initial conditioning, increase the stability of the initial emission current, and perhaps even increase the area of emission on the pin tip, the etched emitters were annealed in hydrogen to round the pin tips prior to emission testing. Since the copper braze has a relatively high vapor pressure at the temperature required to anneal the pin tips, the Nickel-200 alloy was used to braze the emitter to the 0.125 inch diameter Mo rod used as a support. The vapor pressure of Ni is  $<10^{-4}$  torr at the 1200°C annealing temperature, and it was felt that this would be sufficiently low to prevent contamination of the pins.

Five annealing experiments were run from 850°C to 1200°C and unfortunately excessive contamination of the tungsten fibers from the nickel braze resulted in each case. X-ray analysis in an SEM indicated foreign deposits on the tungsten fibers contained Ni and Mn (the Ni alloy contained small amounts of Mn, Cr, and Fe). At 850°C the contamination was in the form of deposits on the fibers, and at 1200°C the tungsten fibers melted completely as a result of alloying with the contaminants.

After the poor results with the nickel-brazed samples, a UO<sub>2</sub>-W wafer with 4.5 μm-long cylindrical pins was heated in H<sub>2</sub> at 1600-1700°C for 10 minutes. The sample was

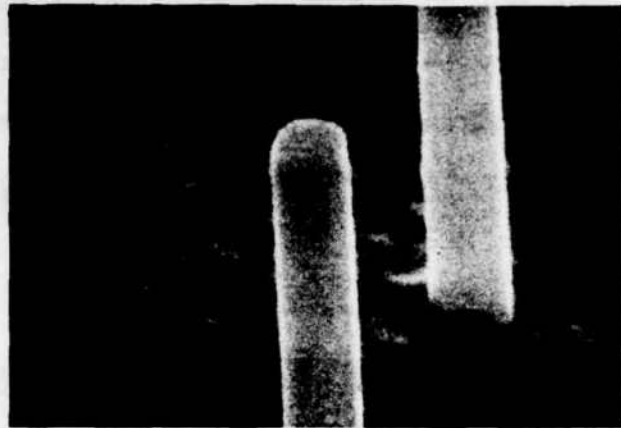
heated unbrazed on a molybdenum pedestal. The tips of the pins were rounded by the annealing to form almost perfect hemispheres, and the pins appeared uncontaminated. The wafer was then silver pasted to an aluminum SEM stub for emission testing as MM-31.

### 3. Ion Milling

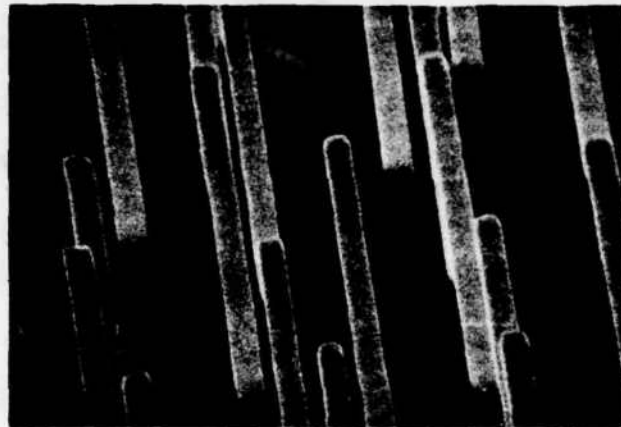
A new technique, based on ion milling, was developed for rounding and pointing exposed tungsten pins. The technique offers an alternative approach to chemical etching to form pointed pin tip shapes. In addition, all intermediate tip shapes from flat cylinders to pointed cones appear attainable using this approach.

Uranium dioxide-tungsten composites were processed to produce exposed fibers with right circular cylinder tips using the standard chemical etching techniques, and then exposed to an 8 KV argon ion beam parallel to the fiber axes. Samples were ion milled for six different times at several different ion beam currents. Since the ion milling rate is proportional to the beam current and to time, the product of ion current and time ( $\mu\text{A}\cdot\text{min}$ ) was the varying parameter. Samples were ion milled for 40, 100, 230, 750, 4250, and 8500  $\mu\text{A}\cdot\text{min}$ , and from scanning electron micrographs (Figures IV-10 and IV-11) the progression of the tip shape from right circular cylinders to pointed cones may be seen as ampere-minutes increased. Initially,

(a)



(b)



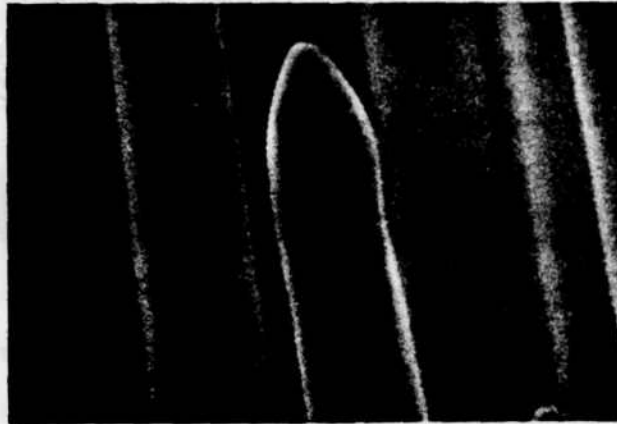
(c)



Figure IV-10. Scanning Electron Micrograph of Ion Milled Exposed Fibers.

(a) 40  $\mu\text{A-min}$ , X28,000;  
(b) 100  $\mu\text{A-min}$ , X14,000; and  
(c) 230  $\mu\text{A-min}$ , X28,000.

(a)



(b)



(c)

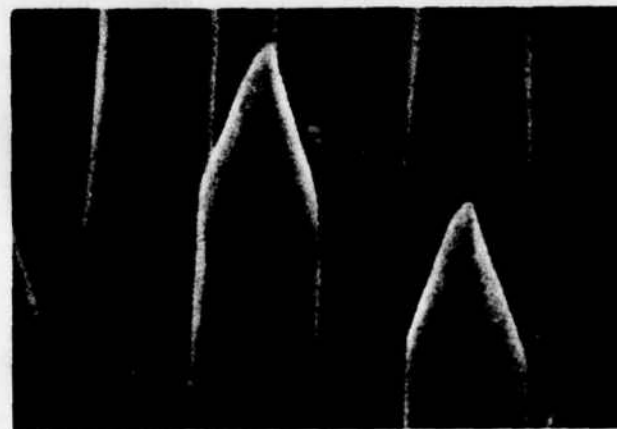


Figure IV-11. Scanning Electron Micrograph of Ion Milled Exposed Fibers.

- (a) 750  $\mu\text{A-min}$ , X29,500;
- (b) 4250  $\mu\text{A-min}$ , X30,000; and
- (c) 8500  $\mu\text{A-min}$ , X16,800.

the edges of the right circular cylinders are rounded (40  $\mu\text{A-min}$ ); later the tips became hemispherical (230  $\mu\text{A-min}$ ), and finally pointed cones with a cone angle of  $35^\circ$  resulted (8500  $\mu\text{A-min}$ ).

A second change in fiber geometry was observed as a function of ion milling as ampere-minutes increased. The diameter of the fibers increased, and by 8500  $\mu\text{A-min}$ , fibers that were initially 0.4  $\mu\text{m}$  in diameter were larger than 1  $\mu\text{m}$  below the cone and tapered out to 2.5  $\mu\text{m}$  at the fiber base. The increase in diameter was caused by material being sputtered from the  $\text{UO}_2$  matrix and the tungsten fibers and subsequently deposited on the sides of the fibers. If the volume or a constant fraction of the volume of material removed from the matrix was deposited on the fibers, then the volume deposited on the fibers would be proportional to  $\pi d^2$  where  $d$  is the fiber diameter or  $d$  would be proportional to the square root of amp-min since the thickness of matrix removed is proportional to ampere-min. The fiber diameters measured just below the milled tips, Table IV-IV was found to be linearly dependent on the square root of amp-min (Figure IV-12). Certainly the majority of the material deposited on the fibers is  $\text{UO}_2$  from the matrix. For Sample Q, milled 8500  $\mu\text{A-min}$ , the average fiber diameter was 1.05  $\mu\text{m}$  and length was 12  $\mu\text{m}$ . The sample had a density of  $10 \times 10^6$  fibers/ $\text{cm}^2$ . Assuming that the fibers

Table IV-IV. Milling Time, Ion Current, and Tungsten Fiber Diameter for Ion Milled  $UO_2$ -W Composites with Exposed Fibers.

Sample	Time (min)	Ion Current ( $\mu A$ )	Time x Ion Current ( $\mu A$ -min)	Fiber Diameter ( $\mu m$ )
U	2	20	40	0.40
T	5	20	100	0.36
Q	10	23	230	0.46
T	15	50	750	0.55
U	42.5	100	4250	0.88
Q	85	100	8500	1.05

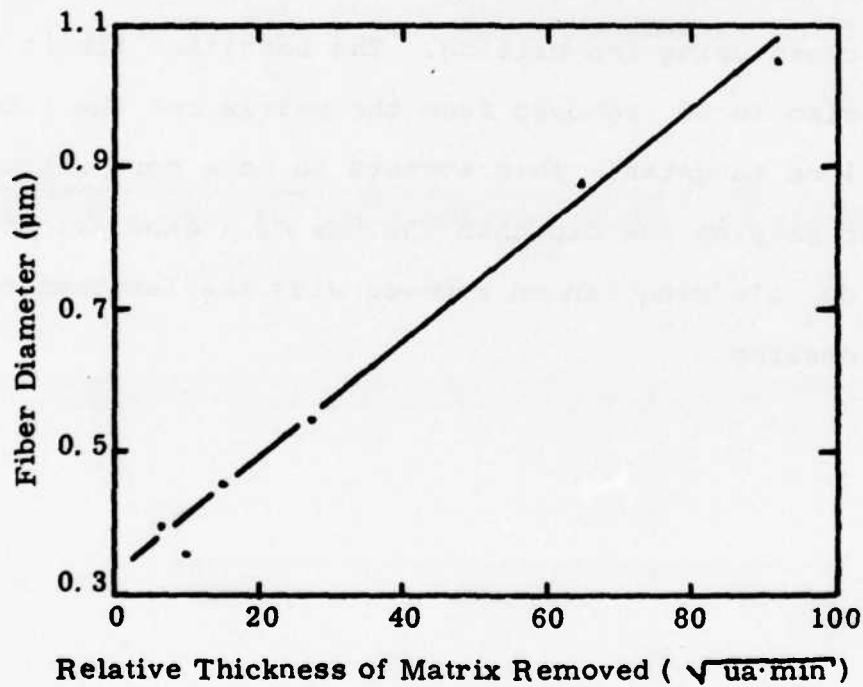


Figure IV-12. Relation Between Increased Fiber Diameter Due to Sputtered Deposits and Relative Thickness of Matrix Removed, for  $UO_2$ -W Composites, Ion Milled with Exposed Fibers.

did not taper out at the base, a matrix thickness of 3.5  $\mu\text{m}$  would be required to increase the fiber diameters from 0.4 to 1.05  $\mu\text{m}$  but a fiber length of more than 70  $\mu\text{m}$  would be required if the deposit were mainly tungsten from the exposed fibers. Since the pins were etched to form right circular cylinders 10  $\mu\text{m}$  tall, the cladding on the sides of the fibers must be mainly  $\text{UO}_2$  contaminated with tungsten.

In conclusion, the tip shapes of exposed tungsten fibers may be varied from right circular cylinders to pointed cones using ion milling. The resultant fibers will be clad in  $\text{UO}_2$  removed from the matrix but the fiber tips will be tungsten. This appears to be a more reproducible method of shaping the tip than the use of a chemical etch, and the  $\text{UO}_2$  cladding can be removed with the lengthening etch if desired.

## SECTION V

### TESTING OF PROTOTYPE FIELD EMISSION CATHODES

The purpose of the field emission testing program was to evaluate the performance of prototype  $\text{UO}_2\text{-W}$  composite cathodes operating at current densities of  $100 \text{ mA/cm}^2$  and above. Goals included optimizing emission current with respect to cathode geometry, determining the emission current capacity of individual pins, and operating a field emission cathode in a sealed vacuum tube.

A brief outline of field emission theory will be presented first, including a discussion of how the theory is applied in the case of the multi-pin cathodes tested here. This will be followed by a description of the apparatus and equipment used to test the cathodes. Next, general procedures common to all of the tests will be outlined, along with the methods used to obtain and analyze the V-I data.

The emission tests themselves are divided into three general categories: 1) Tests evaluating pin and cathode geometry using flat cathodes and a 1.5 mm diameter uniform-field (UF) anode, 2) tests of stylus- or cone-shaped cathodes, either in diode or gun geometries, and 3) tests run in the Semicon vacuum

tubes using various cathode geometries. The more significant tests in each of the three categories will be described in some detail and the results compared and analyzed. Finally, some of the possible mechanisms of pin failure will be reviewed in light of the results obtained from the above tests.

#### A. BACKGROUND THEORY

A rigorous derivation of field emission theory will not be given here. The theory, describing electron emission from metals into a high electric field on the vacuum side, is thoroughly documented in the literature and widely accepted. It relates current density,  $J$ , in  $A/cm^2$ , field strength,  $E$ , in  $V/cm^2$ , and the work function  $\phi$  in eV according to the expression:

$$J = \frac{1.54 \times 10^{-6} E^2}{\phi t^2(y)} \exp \left[ \frac{-6.83 \times 10^7 \phi^{3/2} f(y)}{E} \right], \quad (1)$$

where  $f(y)$  and  $t(y)$  are slowly varying functions of

$$y = \frac{(e^3 E)^{1/2}}{\phi} = \frac{3.79 \times 10^{-4} E^{1/2}}{\phi}. \quad (2)$$

Unfortunately, neither current density nor electric field can be measured directly, so it is necessary to rewrite equation (1) in terms of voltage and current, quantities which can be determined experimentally,

using the relations,

$$I = JA \quad (3)$$

and

$$E = \beta V. \quad (3a)$$

Here  $I$  is the total current in amperes produced by a field emission tip,  $A$  is the emitting area of the tip in  $\text{cm}^2$ ,  $V$  is the voltage applied between the tip and the anode, and  $\beta$  is a factor by which the electric field is enhanced at the surface of the emitter, dependent on the geometry of the emitter and the anode and measured in  $\text{cm}^{-1}$ .

Substituting the above relations in Equation (1) gives:

$$I = \frac{1.54 \times 10^{-6} A \beta^2 V^2}{\phi t^2(y)} \exp \left[ \frac{-6.38 \times 10^7 \phi^{3/2} f(y)}{\beta V} \right]. \quad (4)$$

Equation (4) is often rewritten in logarithmic form:

$$\log_{10}(I/V^2) = \log_{10} \left[ \frac{1.54 \times 10^{-6} A^2}{\phi t^2(y)} \right] - \frac{2.97 \times 10^7 \phi^{3/2} s(y)}{\beta V} \quad (5)$$

If  $\phi$ ,  $\beta$ , and  $A$  are constant and independent of  $V$ , then a plot of  $\log(I/V^2)$  versus  $1/V$ , will produce a nearly straight line, commonly known as a Fowler-Nordheim plot.

The slope of the line,  $m$ , at any point is given by:

$$m = - \frac{2.97 \times 10^7 \phi^{3/2} s(y)}{\beta}, \quad (6)$$

$$\text{where } s(y) = f(y) - y/2\left[\frac{df(y)}{dy}\right]. \quad (6a)$$

The functions  $f(y)$ ,  $t(y)$ , and  $s(y)$  are tabulated in Table V-I.

A theoretical plot of  $\log(I/V^2)$  versus  $1/V$  will not be perfectly linear due to the effect of the image force correction term,  $s(y)$ ; but the deviations are minimal, particularly at lower current densities, and are undetectable for most experiments. A typical Fowler-Nordheim plot is shown in Figure V-1.

#### 1. Single Pin Geometry

From the Fowler-Nordheim model it is apparent that the performance of the field emitter is initially dependent upon two parameters, the work function  $\phi$  and the electric field  $E$ . Considerations such as high mechanical strength, high melting point, and availability in suitable form have lead most investigators to choose tungsten as the best suited material for field emitters. The work function is fixed by this selection as a fortuitously low value, assuming a clean surface (an assumption stipulated for the Fowler-Nordheim model). Thus the only remaining parameter under the experimenter's control is the value of the applied electric field. The field was defined previously (Equation 3a) as a function of the applied voltage and a parameter,  $\beta$ , which is dependent on the geometry of the emitter tip and the anode.

Table V-I. Values of the Functions  $f(y)$ ,  $t(y)$ , and  $s(y)$ .

$y$	$f(y)$	$t(y)$	$s(y)$
0.00	1.0000	1.0000	1.0000
0.05	0.9948	1.0011	0.9995
0.10	0.9817	1.0036	0.9981
0.15	0.9622	1.0070	0.9958
0.20	0.9370	1.0111	0.9926
0.25	0.9068	1.0157	0.9885
0.30	0.8718	1.0207	0.9835
0.35	0.8323	1.0262	0.9777
0.40	0.7888	1.0319	0.9711
0.45	0.7413	1.0378	0.9637
0.50	0.6900	1.0439	0.9554
0.55	0.6351	1.0502	0.9464
0.60	0.5768	1.0565	0.9366
0.65	0.5152	1.0631	0.9261
0.70	0.4504	1.0697	0.9149
0.75	0.3825	1.0765	0.9030
0.80	0.3117	1.0832	0.8903
0.85	0.2379	1.0900	0.8770
0.90	0.1613	1.0969	0.8630
0.95	0.0820	1.1037	0.8483
1.00	0.0000	1.1107	0.8330

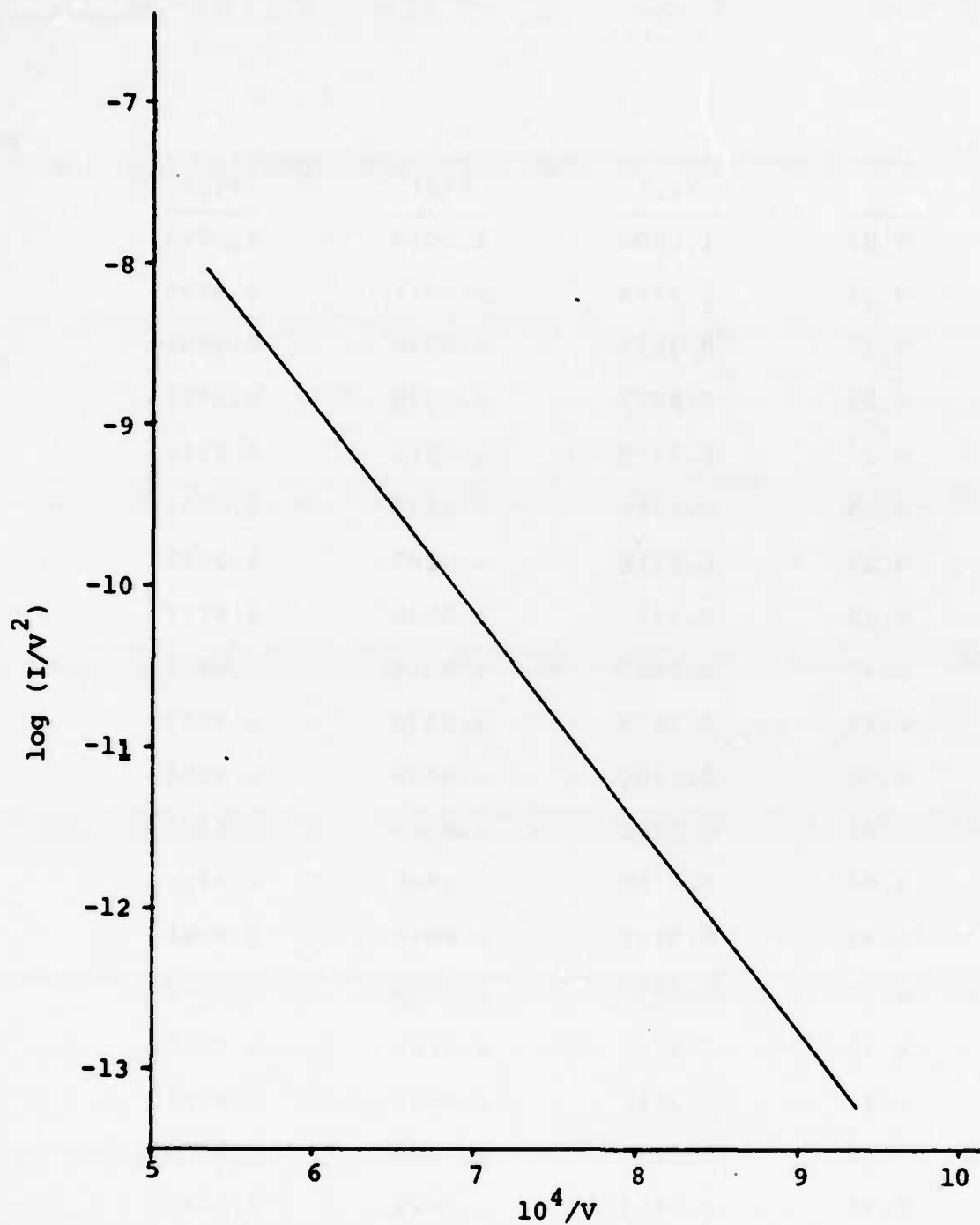


Figure V-1. Example of a Typical Fowler-Nordheim Plot.

Several investigators<sup>5-9</sup>, in attempting to verify the Fowler-Nordheim model, have devised methods of approximating the value and distribution of the field over the tip of an emitter. In general, each of the approximations involves modification of the equations for the field at the surface of a free sphere of radius  $r$ , at potential  $V$ , given by:

$$E = V/r. \quad (7)$$

From Equation 3a, then, the value of  $\beta$  is  $r^{-1}$  for the case of the isolated sphere. At the apex of an actual tip, the field is reduced from the above value due to the presence of the pin shank, for which a general expression can be written:

$$E = V/kr \quad (8)$$

so that

$$\beta = 1/kr. \quad (9)$$

Thus  $k$  is a factor which defines the degree of field strength reduction, due to the influence of the pin shank, on the strength of the field at the tip. Gomer<sup>10</sup> has pointed out that all of the various models yield values of  $k \approx 5$  and that assumption of this value is often adequate.

## 2. Multi-Pin Emitters.

Because of the complexity of the problem, there has been no really adequate theoretical treatment of the case of the multi-pin emitter. Even assuming a perfectly uniform array, one must determine the effect of neighboring pins on the field at an individual pin tip. The best estimate of this effect to date is given by Levine<sup>11</sup>, who has derived an expression for the value of  $\beta$  at the tip of an individual pin in an array as a function of the geometrical parameters of the pin and array. It is expressed as follows,

$$\beta = \frac{1}{r(1+\alpha)}, \quad (10)$$

where  $\alpha = 4\pi dr/a^2$

and  $d$  = the interelectrode spacing,  
 $r$  = the pin tip radius,  
 $a$  = the pin separation distance.

The quantity  $\alpha$  in Equation (10) represents the amount by which the value of  $\beta$  is reduced due to interaction between neighboring pins in the array. Since the effect of pin height was not considered in this analysis, the value calculated from a given set of values of  $d$ ,  $r$ , and  $a$  probably represents an upper limit for the value of  $\beta$ . The assumption is made that the pin height is sufficient to assure that all electric flux lines are gathered to the pin tips and none reach the pin shank or the matrix surface.

The above approximation can be further improved if the reduction of the field at the tip due to the effect of the pin shank, discussed above, is taken into account. If the value of  $k$  is assumed to equal 5, equation (10) becomes

$$\beta = \frac{1}{5r(1+\alpha)} . \quad (11)$$

If one assumes that equation (11) describes the field enhancement at the tip of an individual pin in an array, then equation (1) gives the current density,  $J$ , at the tip of that pin. If the tip of the pin is assumed to be hemispherical, the emitting area at the tip,  $A_p$ , is given by the expression:

$$A_p = 2\pi r^2(1-\cos\theta) \quad (12)$$

where  $\theta$  is the polar angle measured from the center of curvature of the pin tip. If this angle is taken as  $60^\circ$ , a not unreasonable assumption, then equation (12) reduces to

$$A_p = \pi r^2 , \quad (13)$$

and the current density of a square array,  $J_m$ , is then given by the expression:

$$J_m = \frac{A_p}{a^2} J = \frac{\pi r^2}{a^2} J \quad (14)$$

An analysis of the effects of each of the geometrical parameters,  $a$ ,  $r$ , and  $d$  on the value of  $J_m$  indicates that array current density is particularly sensitive to changes in the pin separation distance and the pin tip radius.

#### B. TEST FIXTURES AND CATHODE INSTALLATION PROCEDURES

The various fixtures used for the emission tests and the procedures for installing the cathodes are described next. In almost all cases the cathodes were inspected in the scanning electron microscope (SEM) prior to installation in the test fixture. Assessments were made of such parameters as pin height, pin diameter, pin tip shape, array uniformity, array density, and presence of contaminants, if any. All components were thoroughly cleaned in methanol prior to insertion in the vacuum system.

##### 1. Water-Cooled, Fixed-Spacing Diode.

Most of the tests using the uniform-field anode and several of the stylus cathode tests were run in the fixed-spacing, water-cooled diode shown in Figure V-2. Two high-current insulated feedthroughs were mounted in a nine-inch ASA-type flange and machined so that the anode and cathode mountings were parallel to within

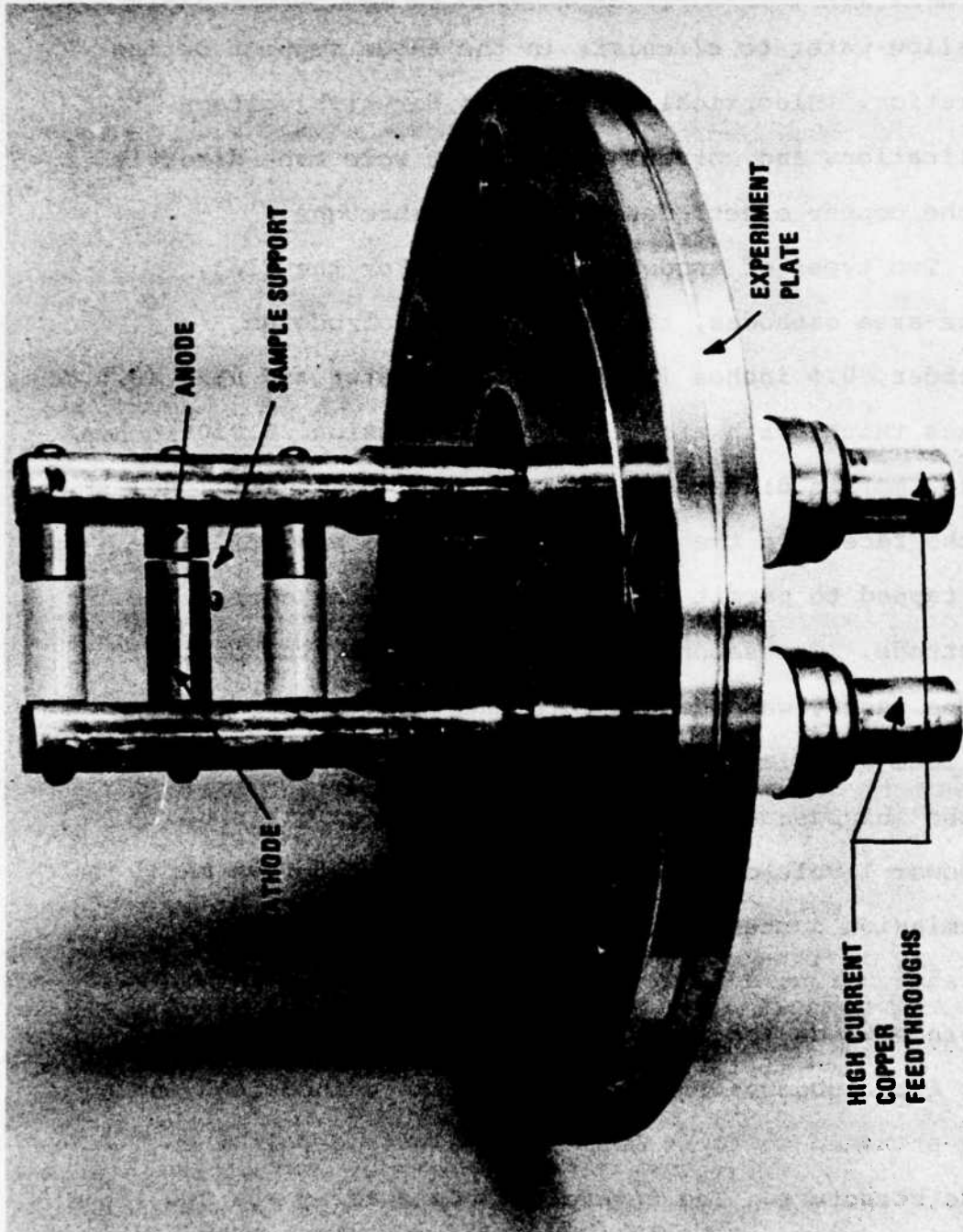


Figure V-2. Fixed-Spacing Water-Cooled Diode Test Fixture.

0.001 inch (25  $\mu\text{m}$ ). Water cooling was provided by drilling the electrodes to a depth of six inches (15 cm) to allow water to circulate in the anode support during operation. Electrical connections for high voltage applications and current measurement were made directly to the copper electrodes of the feedthroughs.

Two types of anodes were used. For the flat, large-area cathodes, the anode was a molybdenum cylinder, 0.5 inches (12.5 mm) in diameter and 0.25 (6.3 mm) inches thick, with a cylindrical protrusion, 0.060 inches (0.152 mm) in diameter by 0.05 inches (0.125 mm) long, on the face. On the back side the anode was drilled and tapped to permit it to be bolted to the copper electrode. The second anode, used for several of the stylus tests, was identical to the first except that the face was flat with no protrusion. Thermal expansion of the molybdenum anodes proved to be negligible up to power levels of ten watts (usually about five mA of emission current), making it possible to obtain voltage-current data up to this power level with minimal interelectrode spacing variation.

After observation in the SEM, the cathode and anode were attached to their respective electrodes in the diode structure. The interelectrode spacing was set by viewing the structure in a binocular microscope

(at 30x) and comparing the backlighted gap with a piece of shim stock of known thickness. Spacings of 0.001 inch to 0.008 inch ( $2.5 \times 10^{-3}$  cm to  $2.0 \times 10^{-2}$  cm) were used for most of the tests.

## 2. Semicon Vacuum Tubes.

A variety of cathodes were installed in the Semicon vacuum tubes, although the majority were styluses mounted on 1/16 inch (0.15 mm) diameter molybdenum rods. The cathodes were fabricated at Georgia Tech and then hand carried to Semicon Associates, Lexington, Kentucky, where they were mounted in the tubes. Frequently, the cathodes were simply spot-welded to the Mo support wires in the tube; in some of the tubes, however, the cathode was secured in a stainless steel support with a setscrew to permit more accurate setting of the interelectrode spacing. (Note, for example, the two tubes on the left in Figure V-3.) The anode used for all of the tube tests was a piece of 0.030 inch (.075 mm) molybdenum sheet, 1/2 inch (12.5 mm) wide by 1.5 inches (38 mm) long, bent in the shape of a square U. Before spot-welding the anodes into the tubes, they were polished with one micron diamond grit and heated to  $1500^{\circ}\text{C}$  in a hydrogen furnace to remove any oxide or other contaminants from the surface. After the anode and cathode had been

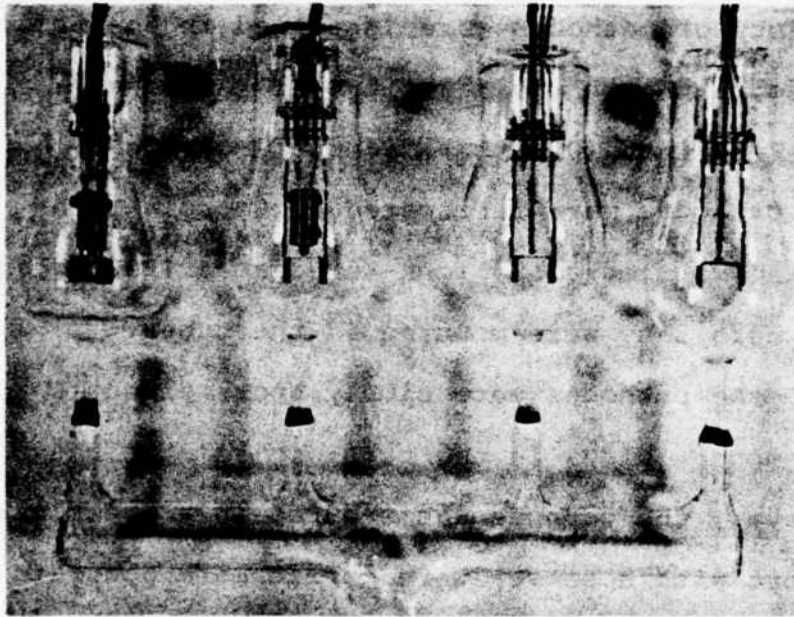


Figure V-3. Glass Manifold With Semicon Tubes Mounted, Ready for Testing, X0.3.

mounted, the tubes were assembled on a glass-blower's lathe at Semicon and then carried back to Georgia Tech where they were mounted on the manifold pictured in Figure V-3. A close-up of one of the tubes in operation is shown in Figure V-44, sub-section H, and the position of anode and cathode can be clearly seen. The final step was to bolt the manifold to the tip of the 2 3/4 inch cross of the 20 liter/s ion-pumped vacuum system and initiate pumpdown.

### 3. RCA Electron Gun.

The apparatus pictured in Figure V-4 was donated by Dr. J.D. Levine, Director of Cathode Development at RCA, Princeton, when their field emission test program was terminated. Designated the RCA Electron Gun, it was used for several of the stylus cathode tests. It consisted of a CRT electron gun modified to accept a field emission cathode on a 1/16 inch diameter support rod, mounted on a 2 3/4 inch o.d. Conflat flange. A diagram of the electron gun is shown in Figure V-5. Electrical connections to the cathode, extractor, and first focusing lens were made by means of feedthroughs on the flange. The flange was bolted to a mating flange on a Pyrex envelope (Figure V-4) which contained a phosphor screen at the opposite end. Electrical connections to the remaining

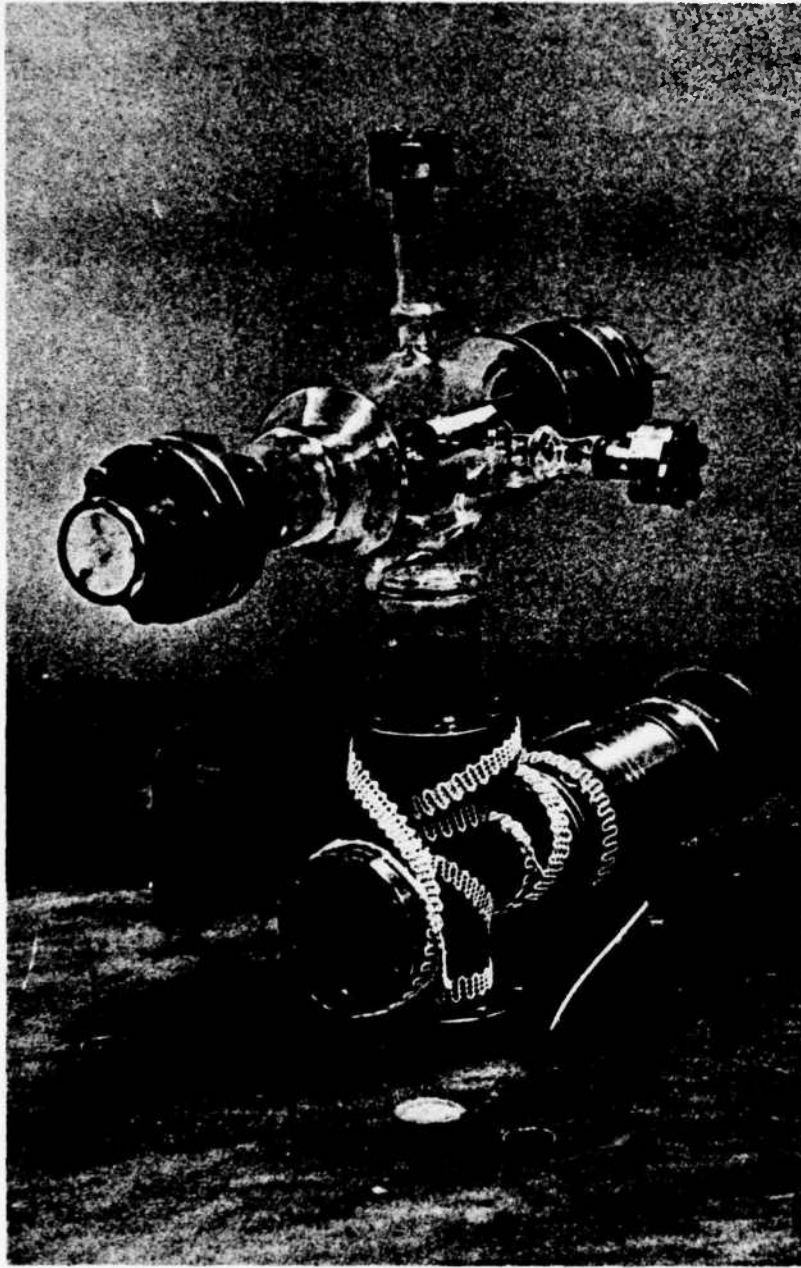


Figure V-4. RCA Gun Mounted on 20 liter/s Vacuum System.

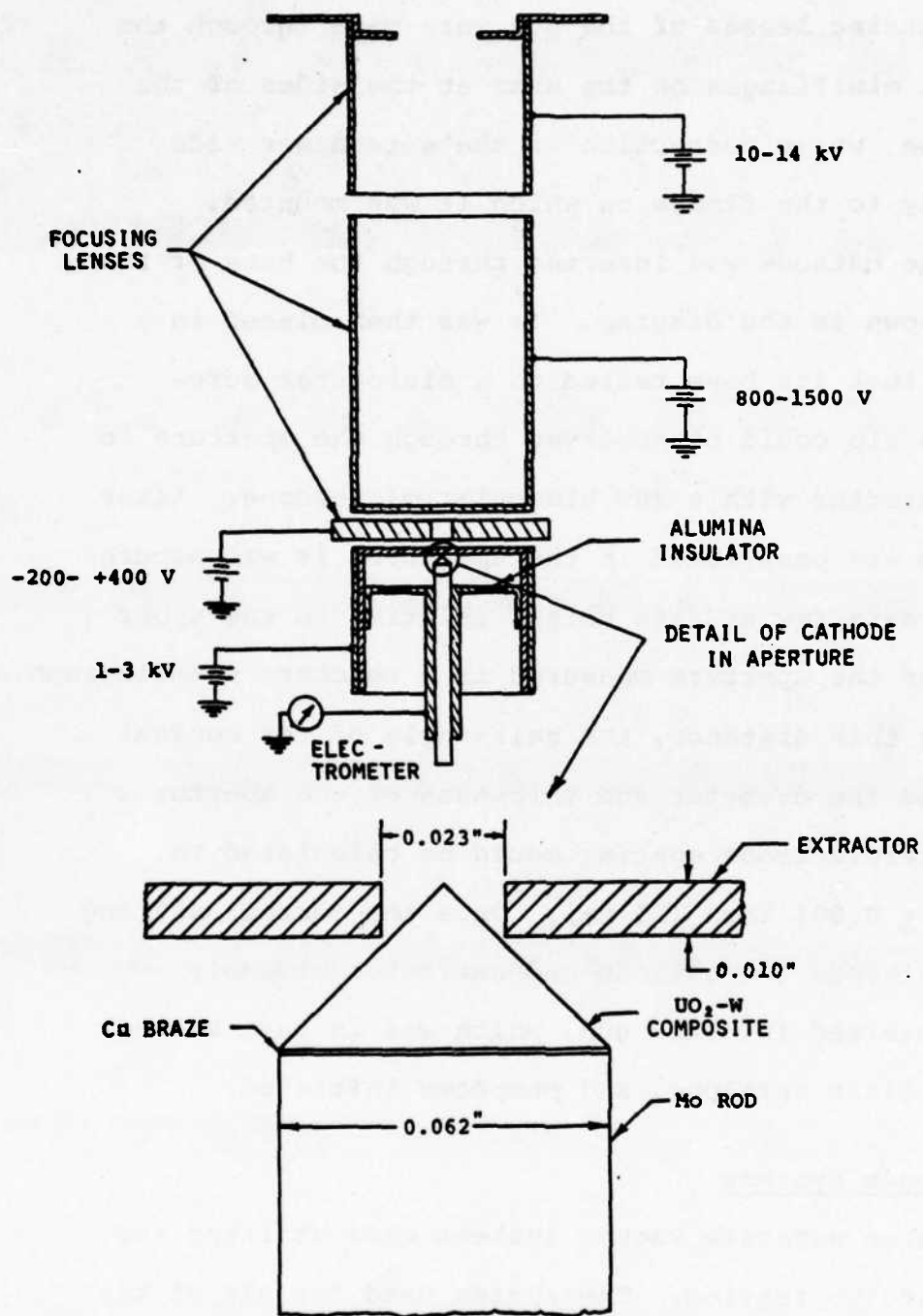


Figure V-5. Schematic Diagram of RCA Gun Showing Position of FE Cathode.

two focusing lenses of the gun were made through the Conflat miniflanges on the arms at the sides of the envelope, while connection to the screen was made directly to the flange on which it was mounted.

The cathode was inserted through the base of the tube shown in the diagram. It was then placed in a jig so that its base rested on a micrometer screw and the tip could be observed through the aperture in the extractor with a 30x binocular microscope. After the tip was positioned in the aperture, it was secured with a setscrew and its height relative to the upper plane of the aperture measured in a Reichert metallograph. Knowing this distance, the half-angle of the conical tip, and the diameter and thickness of the aperture, the interelectrode spacing could be calculated to within  $\pm 0.001$  inch (25  $\mu\text{m}$ ). Once the correct spacing was achieved, the cathode and extractor assembly were inserted into the gun, which was in turn bolted to the glass envelope, and pumpdown initiated.

#### 4. Vacuum Systems

Three separate vacuum systems were utilized for the emission testing. The system used for all of the tests with the water-cooled, fixed-spaced diode consisted of a stainless steel chamber mounted on a table (Figure V-6) and closed by nine-inch ASA-type

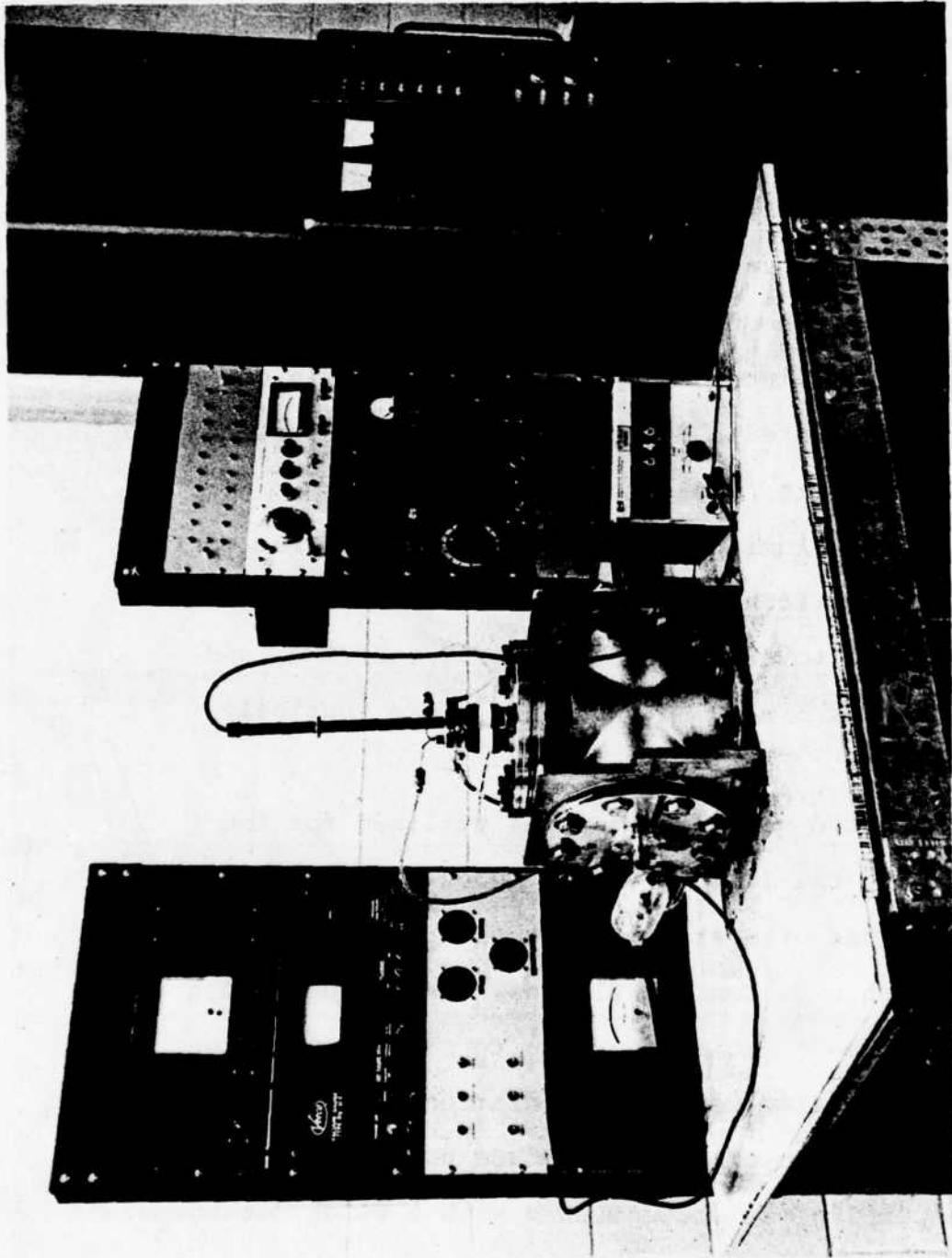


Figure V-6. Diffusion-Pumped Vacuum System Used in the Tests with the Fixed-Spacing Water-Cooled Diode.

flanges. The chamber was pumped by a four-inch CVC oil diffusion pump backed by a Welch mechanical pump, which also served as a roughing pump. A CVC water-cooled chevron baffle and a zeolite molecular sieve trap were used between the diffusion pump and the chamber. (All vacuum system components were below the table.) The chamber was closed on the other two sides by nine-inch ASA-type flanges also, in one of which was mounted a Bayard-Alpert type ionization gauge to monitor pressure. All vacuum chamber seals were of the aluminum o-ring or copper-gasketed Conflat type. Electric heating tapes were used to bake out the chamber to temperatures of 100° to 120°C, and pressures of  $5 \times 10^{-9}$  to  $3 \times 10^{-8}$  were routinely achieved.

A second vacuum system was utilized for the tests with the Semicon vacuum tubes and the RCA Gun. It consisted of a stainless steel cross, equipped with 2 3/4 inch o.d. Conflat flanges, connected through a viton-sealed right angle valve to a 20 liter/s ion pump. The valve permitted isolation of the ion pump during specimen changes to reduce pumpdown time. Rough pumping was accomplished with a Welch mechanical pump through a zeolite trap. Isolation of the system from the roughing pump was provided by a Granville-

Philips gold-seal ultra-high-vacuum valve (Series 204). After overnight bake out to 150° to 200°C, system pressures of 1 to 5 x 10<sup>-8</sup> torr could generally be maintained.

The third vacuum chamber, used for several of the tests, is pictured in Figure V-7. It consisted of a 1.5 inch (38 mm) o.d. Pyrex tube, 2 inches (5 cm) long, with Varian 2 3/4 inch o.d. Conflat flanges at each end, bolted to the top port of a stainless steel cross. The flange on which the cathode support was mounted was bolted between the tube and the cross. The cross was attached directly to a Veeco Mag Ion pump of 150 liter/s capacity. The system was rough pumped either with a Varian VacSorb pump cooled by liquid nitrogen or with a Welch mechanical pump through a zeolite trap. The chamber was isolated from the roughing pump with a Granville-Philips gold-seal ultra-high-vacuum valve (Series 104). Electrical connection was made to the cathode by means of a feedthrough mounted in a flange on the remaining port of the cross. The upper end of the Pyrex tube was closed with a Varian Linear Motion Feedthrough, mounted on a 2 3/4 inch Conflat flange, to which the Mo anode was attached. The entire system was constructed

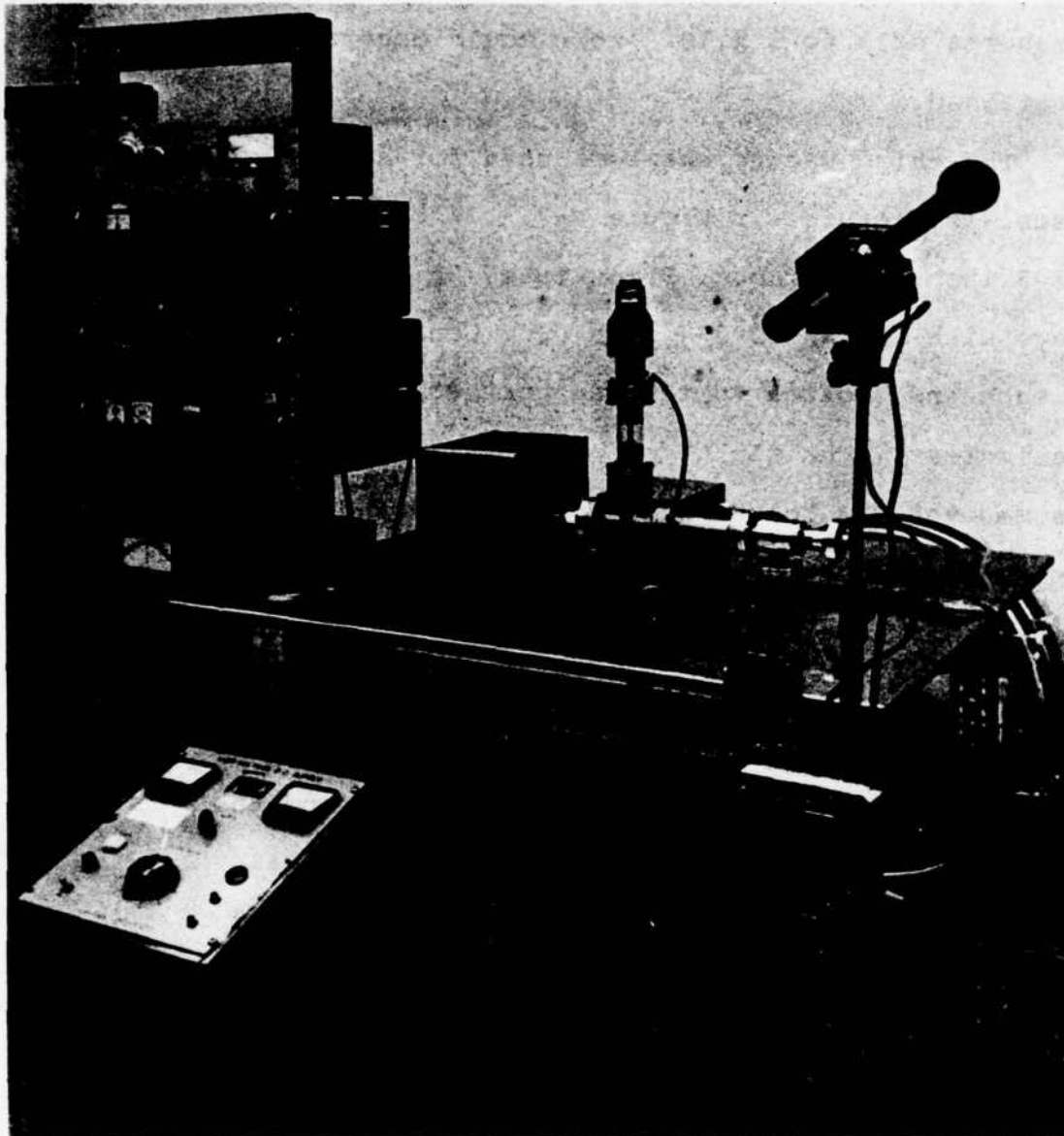


Figure V-7. Ion-Pumped Vacuum System Used in Test MM-32.

of glass and stainless steel and all seals were of the copper-gasketed Conflat type. The ion pump was baked with internal heaters, while heating tapes were used to bake the vacuum plumbing and Pyrex tube. With normal bake out temperatures of 180° to 200°C, pressures of  $5 \times 10^{-9}$  torr and below were routine.

#### 5. Electronics.

All of the field emission tests were conducted using dc power supplies. Table V-II describes the power supplies available, with the voltage and current requirements of a particular test determining which of the supplies was used. A Keithley 610 R or 610 CR electrometer was used for all cw emission current measurements, allowing accurate current measurement ( $\pm$  one percent) over the range from one nA to 100 mA. Applied voltages were measured to  $\pm$  ten volts using either a Hewlet-Packard 3430A digital voltmeter or a Fluke 8000A digital multimeter in conjunction with either a 1000 M $\Omega$  Simpson high voltage probe or a 10,000 M $\Omega$  Fluke high voltage probe. A Moseley Autograf recorder was connected to the electrometer output and used to monitor emission current stability on most of the later tests.

Table V-II. High Voltage dc Power Supplies Used.

<u>Manufacturer</u>	<u>Model No.</u>	<u>Max. Voltage (kV)</u>	<u>Max. Current (mA)</u>
Fluke	412B	2.1	30
Fluke	413D	3.1	20
Fluke	410B	10	10
Sorensen	2012-250	12	250
Del Electronics	50TC-5-1	50	5

Originally, buffer resistors, ranging in size from 1000 M $\Omega$  to 500 k $\Omega$  , were used in series with the field emitter to reduce arc damage. Early in the program however, a current-limiting device was built to replace or augment the buffer resistors. This device employed an RCA 833A vacuum triode with a variac-controlled filament supply. Since the current passed by the device was controlled strictly by the temperature of the filament, it was termed a temperature-limited diode (TLD). For all of the cw tests, the grid and cathode of the TLD were connected together and it was operated in series with, or in place of, the buffer resistor. (Because of its current-voltage characteristics, the TLD provided little protection at very low emission currents. So a 1000 M $\Omega$  buffer resistor was normally placed in the circuit during activation of the emitter and then removed when the emission current reached  $\sim 10$   $\mu$ A.) A schematic diagram of the cw test circuitry is shown in Figure V-8.

For the one pulse test, a pulse circuit was built and connected to the grid of the TLD, as shown in Figure V-9. Emission current was measured with a Tektronix dual-trace oscilloscope across a 10 k $\Omega$  precision resistor. Applied voltage was measured with the same instrument, in conjunction with a Tektronix P6015

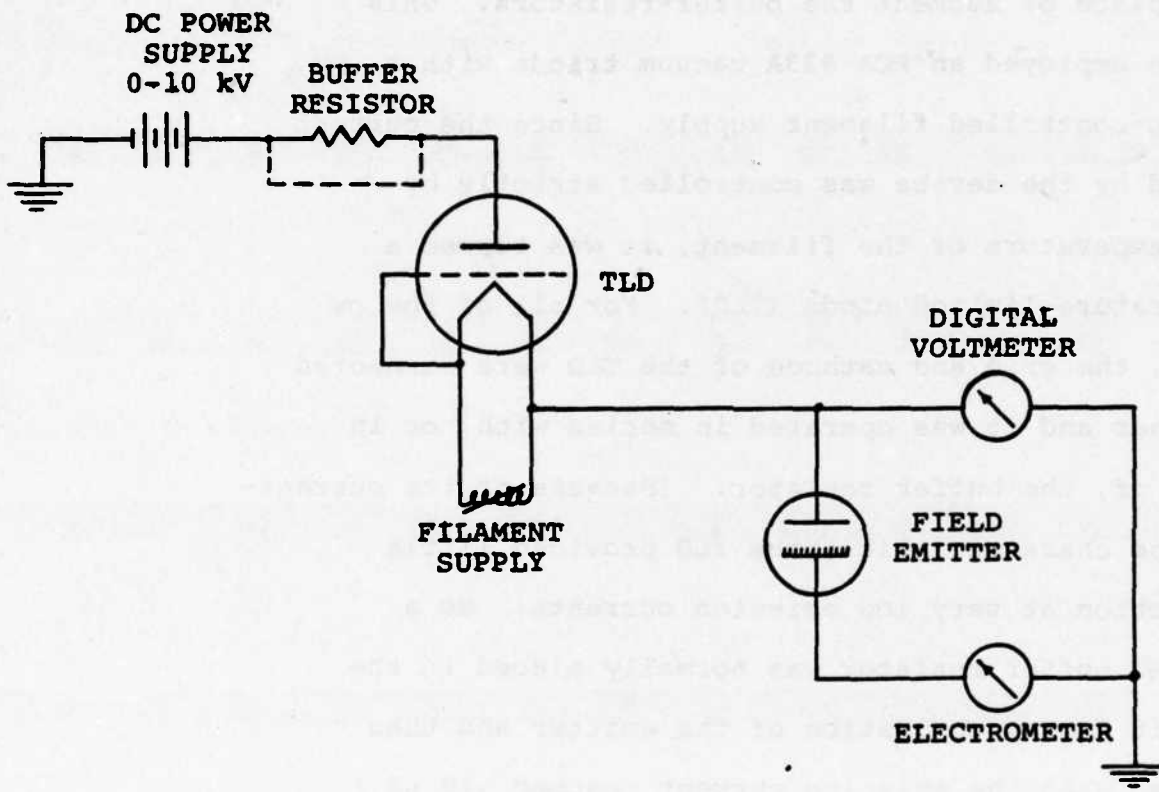


Figure V-8. Schematic Diagram of CW Test Circuitry.

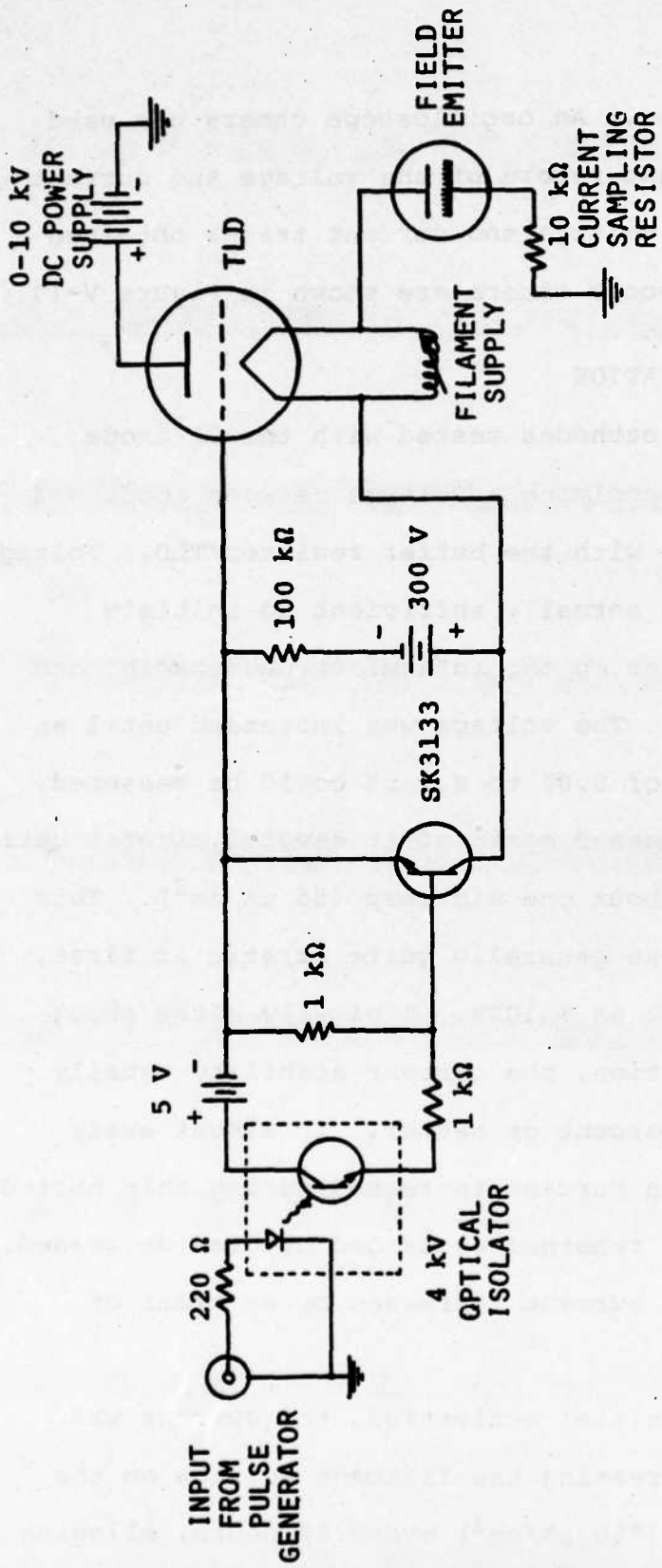


Figure V-9. Schematic Diagram of Pulse Test Circuitry.

High Voltage Probe. An oscilloscope camera was used to make a permanent record of the voltage and current traces. Typical voltage and current traces obtained with the oscilloscope camera are shown in Figure V-10.

### C. CATHODE ACTIVATION

Each of the cathodes tested with the UF anode was activated by applying a voltage between anode and cathode in series with the buffer resistor/TLD. Voltages of 1 to 3 kV were normally sufficient to initiate emission, depending on the interelectrode spacing and pin tip geometry. The voltage was increased until an emission current of 0.01 to 0.1  $\mu\text{A}$  could be measured, and was then increased again after several minutes until the current was about one microamp ( $55 \mu\text{A}/\text{cm}^2$ ). This initial current was generally quite erratic at first, varying by as much as  $\pm 100\%$ . Typically after about 12 hours of operation, the current stability usually improved to  $\pm 5$  percent or better. In almost every case, the emission current increased during this period, while the voltage remained unchanged or even decreased. In some cases the current increased by an order of magnitude or more.

After this initial activation, the current was increased (by increasing the filament voltage on the TLD) about 10  $\mu\text{A}$  ( $550 \mu\text{A}/\text{cm}^2$ ) every 12 hours, allowing

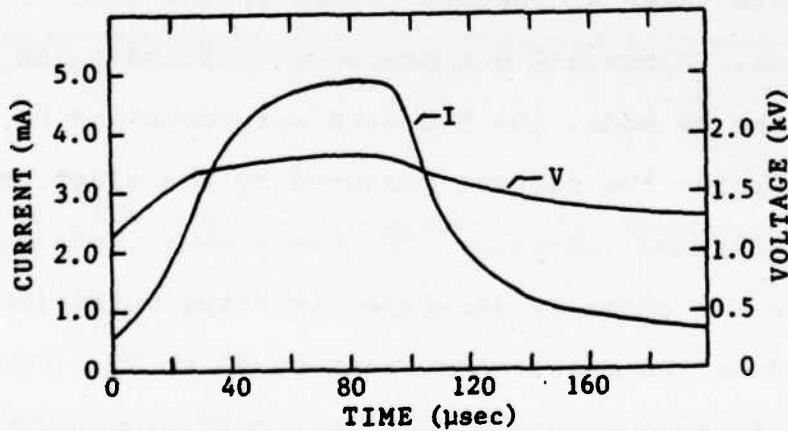
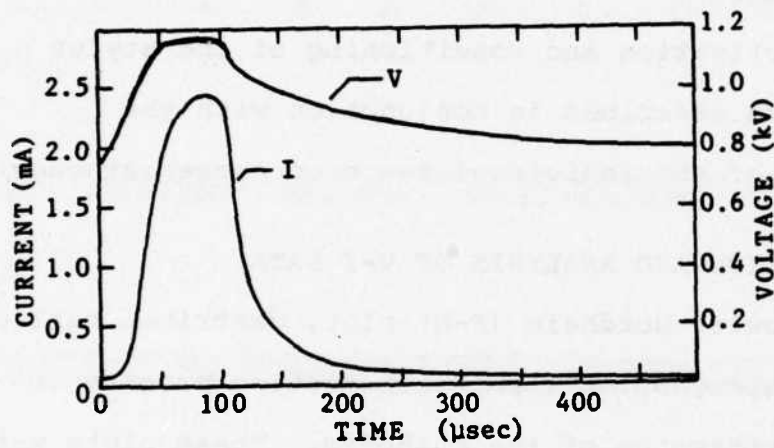
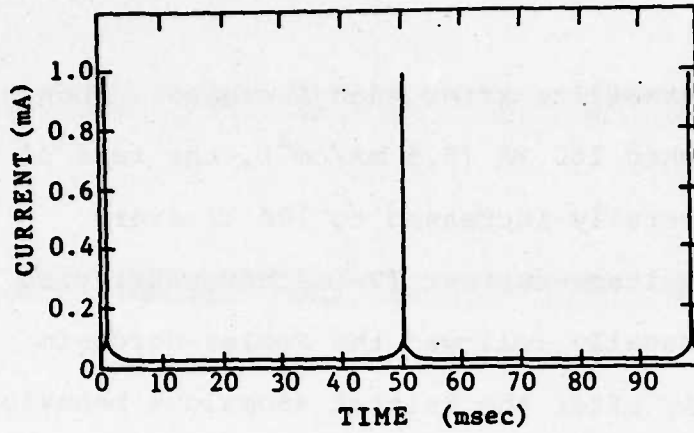


Figure V-10. Examples of Waveforms Observed in the Pulse Test, MM-31.

the emitter to stabilize after each increase. When the current reached 100  $\mu\text{A}$  ( $5.5 \text{ mA/cm}^2$ ), the rate of increase was generally increased to 100  $\mu\text{A}$  every 12 hours. The voltage-current (V-I) characteristics of the emitter usually followed the Fowler-Nordheim Law quite closely after the initial anomalous behavior mentioned above.

The activation and conditioning of the stylus cathodes are described in conjunction with the discussion of the individual tests of those cathodes.

#### D. COLLECTION AND ANALYSIS OF V-I DATA

The Fowler-Nordheim (F-N) plot, described earlier, was used throughout the emission testing program to monitor performance of the cathodes. These plots were based on data taken at various points in the life of each cathode. Since all but one of the cathodes was tested in the cw mode, the V-I data were obtained by simply recording the current measured by the electrometer at various applied voltages. To obtain a V-I data set, the voltage was normally decreased in steps sufficient in size to reduce the emission current by 50 to 75 percent, so that at least two data points were obtained in each current decade. V-I data were usually taken over a minimum of three orders of magnitude change in emission current, with currents being measured down to the  $10^{-8}$  amp decade if necessary.

The primary source of error in the Fowler-Nordheim plot proved to be changes in interelectrode spacing due to thermal expansion of the anodes. As a check on whether the power level was sufficient for anode heating to be a factor (This level varied depending on the test fixture and the initial interelectrode spacing.), a second data set was occasionally taken in a similar fashion by increasing the voltage step-wise to the original value. More frequently the voltage was simply increased rapidly until the emission current reached its original value. Either technique provided a means of checking the reproducibility of the data set. In the case of the pulse test, V-I data were taken directly from the voltage and current traces recorded from the oscilloscope.

The method of least squares regression was used to fit the data to the following generalized expression of equation (5)

$$\log(I/V^2) = a + b\left(\frac{1}{V}\right) \quad (15)$$

The slope,  $m$ , of the fitted line was taken as the slope of the Fowler-Nordheim curve and used in all calculations involving the expression for the slope given by equation (6).

In order to determine how accurately the experimental data fit the derived relationship, the correlation coefficient was calculated according to the following

expression,

$$n = \frac{m\sigma_x}{\sigma_y}, \quad (16)$$

where  $m$  is as defined above and  $\sigma_x$  and  $\sigma_y$  are the square roots of the variances of the values of  $1/V$  and  $\log(I/V^2)$ , respectively. The general expression for the variance is as follows:

$$\sigma_x^2 = \frac{\sum_{i=1}^N x_i^2}{N} - \bar{x}^{-2}. \quad (17)$$

No data were considered valid if the value of the correlation coefficient was lower than 0.985.

Once the value of  $m$  was determined, it was possible to calculate the value of the field enhancement factor,  $\beta$ , from equation (6). Before this calculation could be carried out, however, it was necessary to know the value of the work function  $\phi$ . This was taken as 6.6 eV, the best value which could be found in the literature for oxygen-contaminated tungsten. (Since no effort was made to clean the tungsten pins, one must assume they were contaminated with one or more monolayers of oxygen.) For maximum accuracy in the range of electric field covered, it was also necessary to include the image force correction,  $s(y)$ , in the calculation. Rather than interpolate from the values in Table V-I, the

relations below were found to fit the actual functions within an error of one percent:

$$f(y) = 1 - y^{1.7} \quad (18)$$

$$t(y) = 1 + 0.1107y^{1.43} \quad (19)$$

$$s(y) = 1 - 0.15y^{1.7} \quad (20)$$

Once an appropriate value for  $s(y)$  was determined by iteration, then the value of  $\beta$  could be calculated. The electric field for each value of voltage could then be determined from equation (3a). By inserting the appropriate values of  $E$ ,  $\phi$ ,  $f(y)$ , and  $t(y)$ , the current density  $J$  could be calculated from equation (1), and the total emitting area from equation (3), for each value of voltage and current measured. Of course, the above calculations require that  $A$ ,  $\beta$  and  $\phi$  all be independent of the applied voltage.

To insure maximum accuracy, the V-I data from which the values of  $\beta$  and emitting area were calculated were taken only after the cathodes had reached operating levels of at least 50 mA/cm<sup>2</sup>. The value of emitting area for each of the cathodes was calculated at a current density of  $\sim 5$  mA/cm<sup>2</sup>.

#### E. TESTS WITH THE UNIFORM-FIELD ANODE

Prior to use of the uniform-field (UF) anode, described earlier, most of the field emission cathodes had been tested under a planar anode. For several

reasons, discussed by Ohlinger<sup>12</sup>, this geometry produced a sharply enhanced field at the edges of the cathode. This, of course, greatly reduced the number of pins on the cathode available for emission. Experiments with various anode-cathode geometries resulted in the eventual use of the UF anode. The major advantage of this geometry was that it produced a relatively uniform field over a well-defined area of the cathode surface.

A total of seventeen tests were run with the UF anode/large-area cathode geometry. The pin geometry, anode-cathode spacing, any special treatments of the cathodes, and the results of the tests are summarized in Table V-III, (sub-section F). The conditioning schedules for the two most successful tests are shown in Figures V-11 and V-12 respectively, and plots of array current density versus voltage for several of the tests are shown in Figure V-13. The most significant tests are described in detail below.

The first tests were similar in nature, designed to determine the effect of pin geometry and interelectrode spacing. (It became apparent from the first test that the primary emission current goal of  $100 \text{ mA/cm}^2$  could be met. Thereafter, the major effort was devoted to determining the optimum cathode and pin

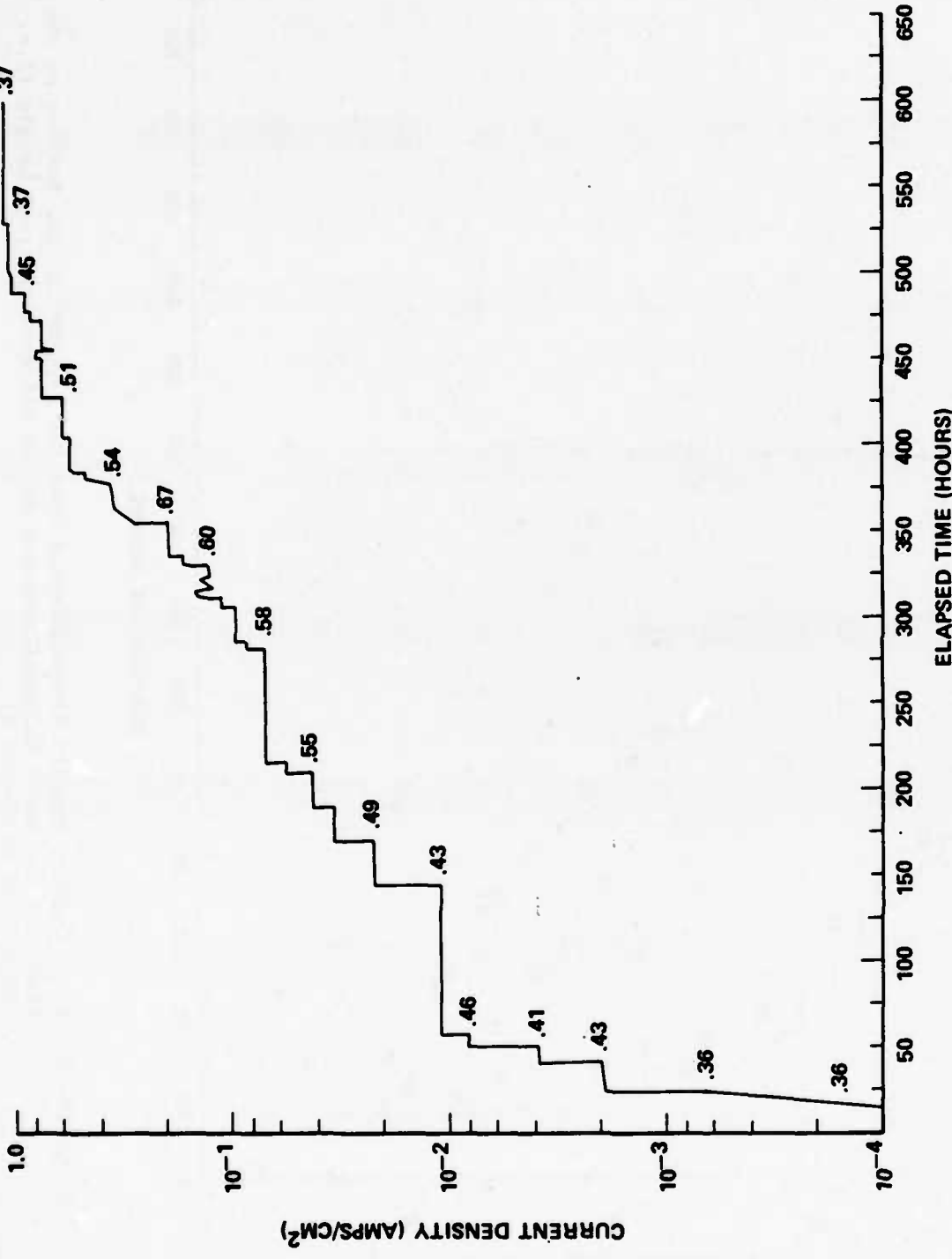


Figure V-11. Array Current Density Versus Elapsed Time for Test MM-6, the Numbers on the Graph are the Anode Voltages Measured at the Different Current Levels (i.e. .55 is 0.55 kV or 550 V).

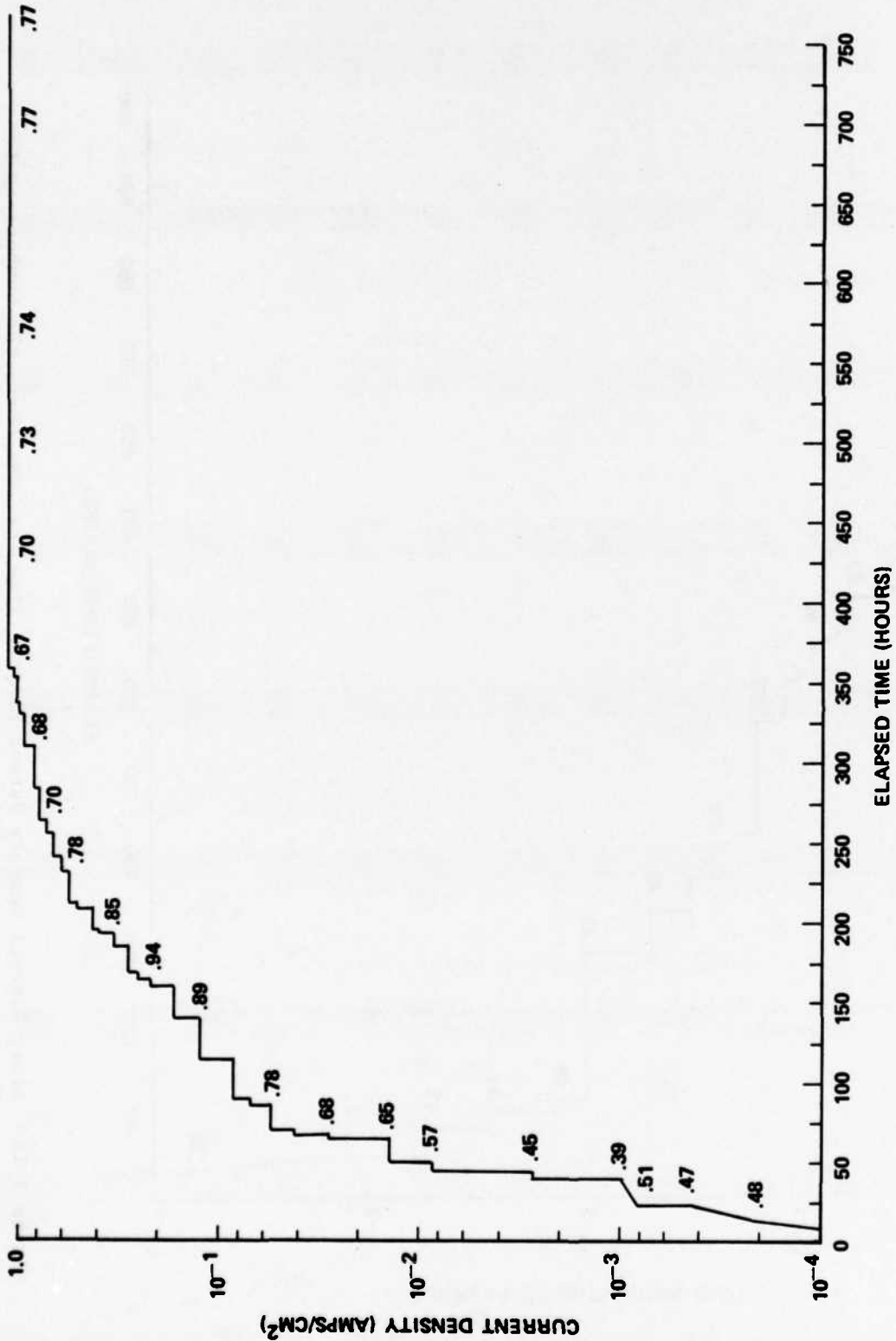


Figure V-12. Array Current Density Versus Elapsed Time for Test MM-10, the Numbers on the Graph are the Anode Voltages Measured at the Different Current Levels (i.e. .85 is 0.85 kV or 850 V).

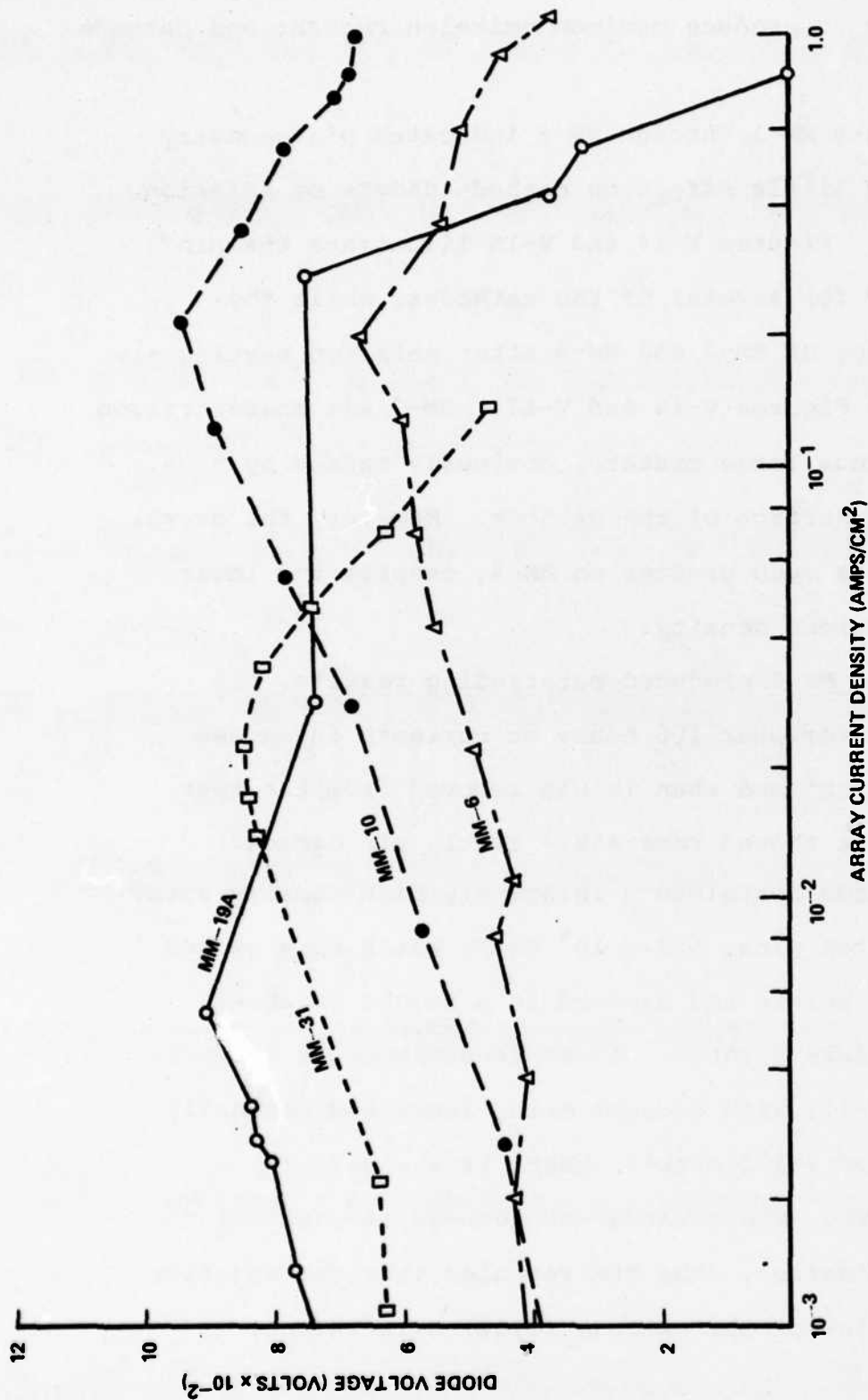


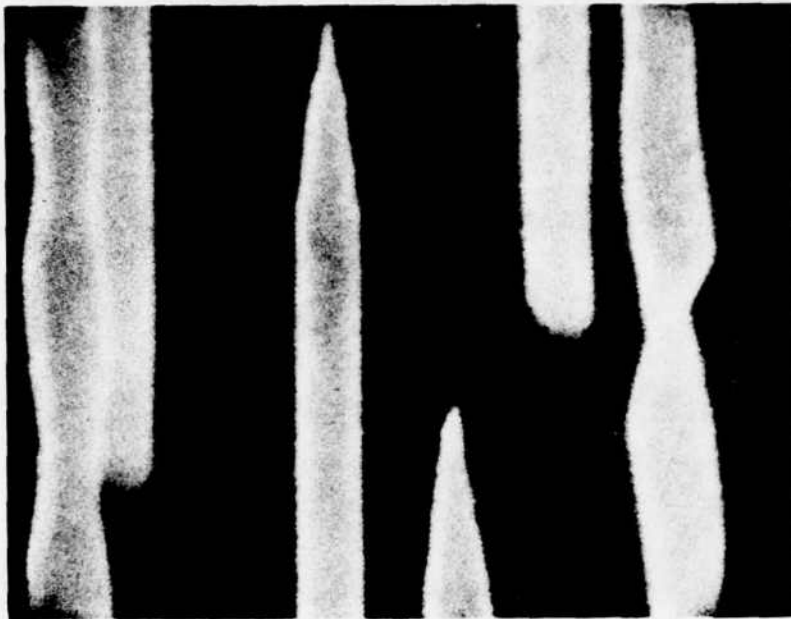
Figure V-13. Diode Voltage versus Array Current Density for Four Tests, Illustrating the Effect of Anode Heating on Voltage.

geometry to produce maximum emission current and cathode life.)

Tests MM-1 through MM-5 indicated pin geometry had very little effect on cathode damage or emission current. Figures V-14 and V-15 illustrate the pin geometry for several of the cathodes, while the appearance of MM-3 and MM-4 after emission testing are shown in Figures V-16 and V-17. MM-3 was characterized by numerous large craters, obviously caused by arcs, over the surface of the cathode. However, the overall damage was much greater on MM-4, despite the lower array current density.

Test MM-6 produced outstanding results. It operated for over 100 hours at currents in excess of  $1.0 \text{ A/cm}^2$  and when it was removed from the test fixture it showed remarkably little pin damage. The cathode contained a relatively high-density array of tungsten pins,  $\sim 20 \times 10^6 \text{ cm}^{-2}$ , which were etched to sharp points and exposed to a height of about  $8 \text{ }\mu\text{m}$  (Figure V-15b). It was conditioned as shown in Figure V-11, with current being increased gradually to  $21.5 \text{ mA}$  ( $\sim 1.2 \text{ A/cm}^2$ ), where it was held for  $\sim 100$  hours. The cathode was removed at this point for examination. The SEM revealed that the majority of the pins on the cathode ( $\sim 90\%$ ) were intact.

(a)



(b)

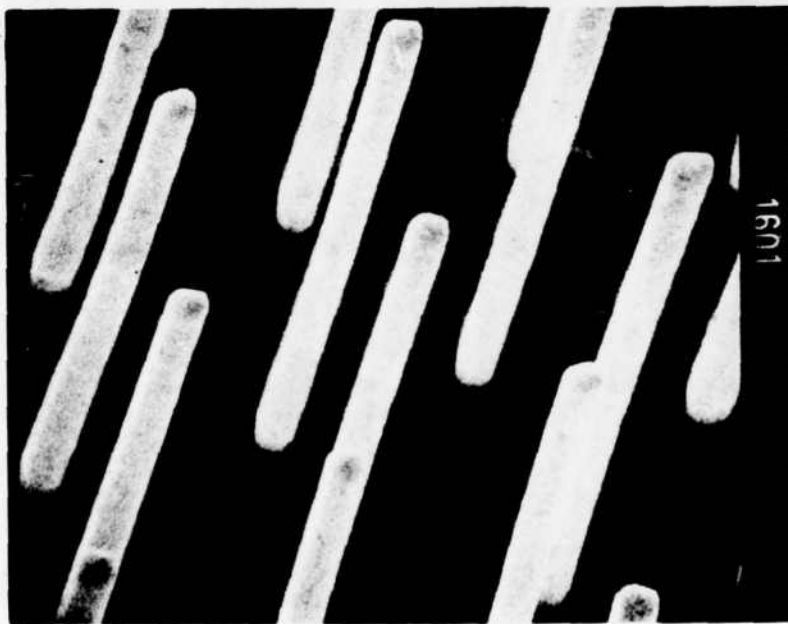
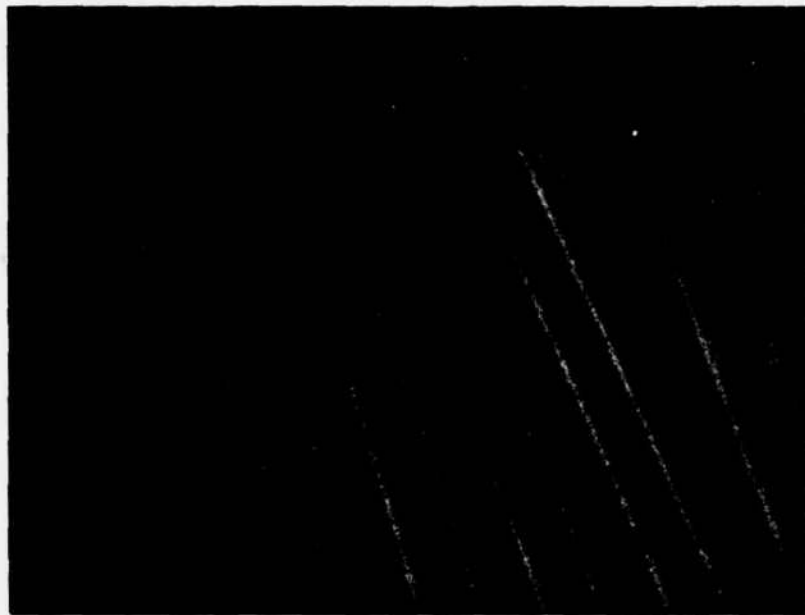


Figure V-14. Typical Pin Tip Shape on Cathodes MM-3 and MM-4 Prior to Testing.  
(a) MM-3, X21500, (b) MM-4, X11700.

(a)



(b)

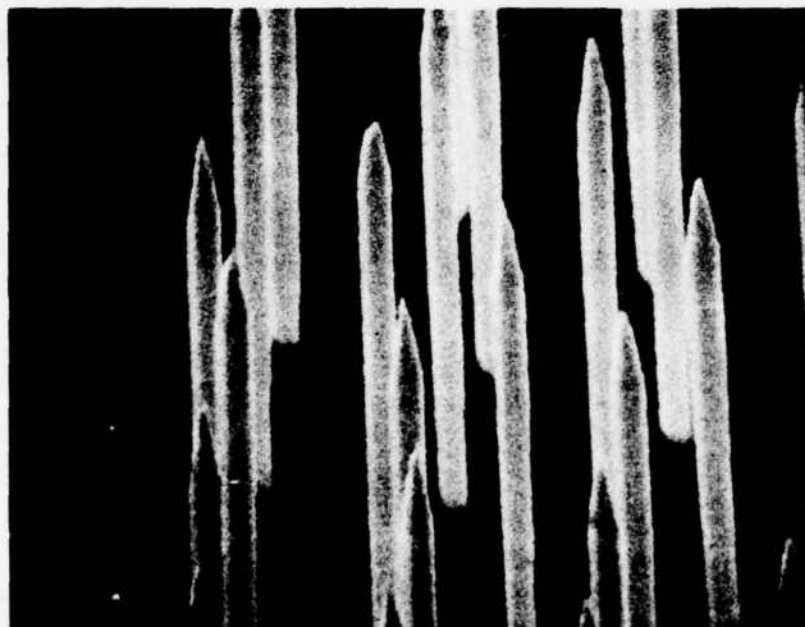


Figure V-15. Typical Pin Tip Shape on Cathodes  
MM-5 and MM-6 Prior to Testing.  
(a) MM-5, X22500, (b) MM-6, X1400.

(a)



(b)

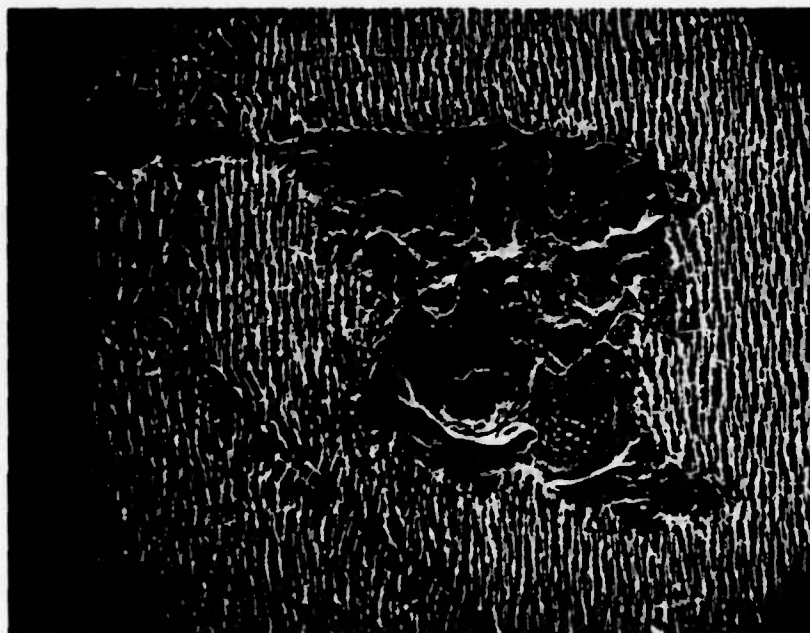
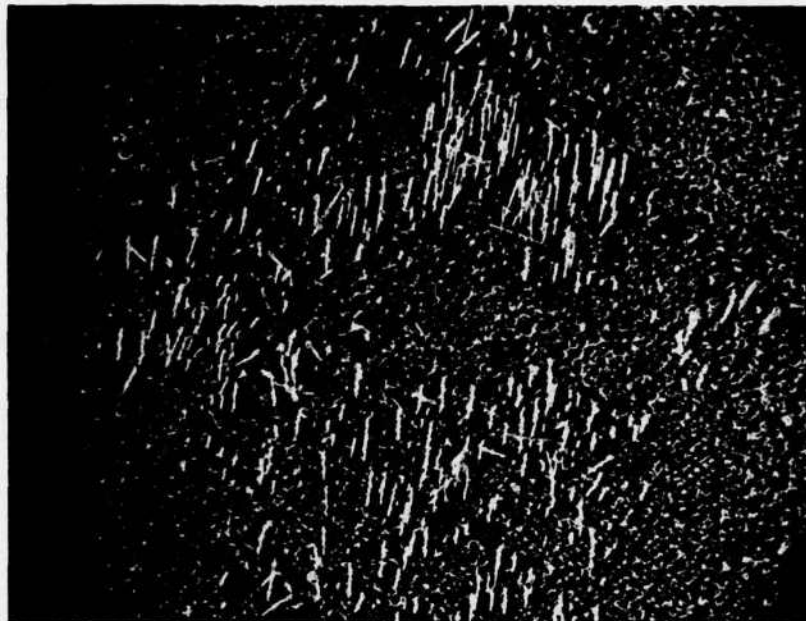


Figure V-16. Post-Emission View of the Cathode Used in Test MM-3, Illustrating the Damage Caused by Vacuum Arcs. (a) X70, (b) X610.

(a)



(b)

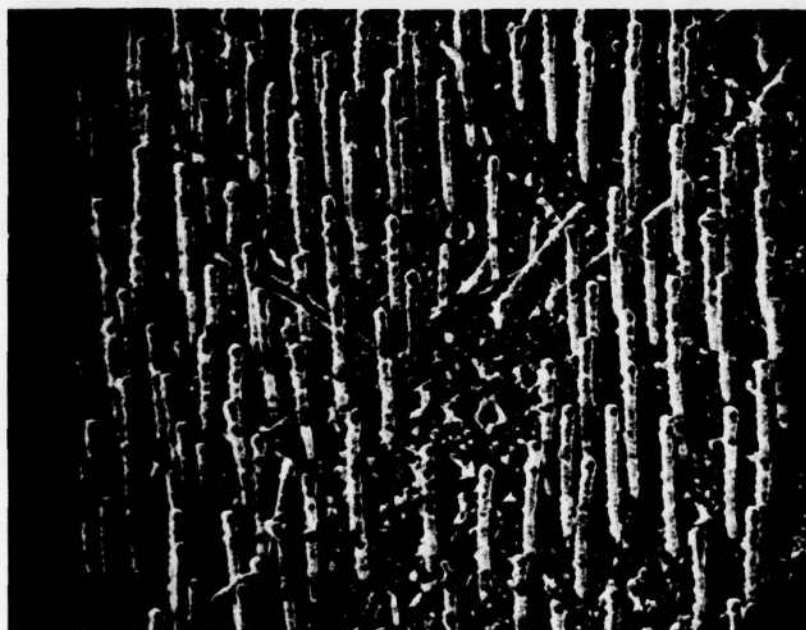


Figure V-17. Post-Emission Appearance of the Cathode Used in Test MM-4, (a) X590, (b) X2400.

Figure V-19 shows an area of arc damage, but such areas represented only ~10% of the cathode surface under the UF anode.

The reason for the success of this particular cathode was thought to be connected with the very low diode voltage but the overriding effect of the combination of sharply pointed pins and very small interelectrode spacing was not immediately recognized as the cause of the low voltage. The interelectrode spacing had originally been set at 0.004 inch (100  $\mu\text{m}$ ). However, when the flange was bolted to the vacuum chamber and the chamber evacuated, the flange flexed slightly, causing the electrodes to pivot around the spacer and close down the anode-cathode spacing. Based on V-I data from later experiments, the interelectrode spacing for MM-6 was probably no more than 25  $\mu\text{m}$ . To further complicate matters, the temperature-limited diode (TLD) had been installed early in the course of this test and was thought to have reduced pin damage on the cathode by limiting arc currents.

It was during the course of this test that the effect of thermal expansion of the anode, at power levels of 3 watts or more, became very noticeable. If the emitter was turned on after being off for several hours, and the current was increased quickly to

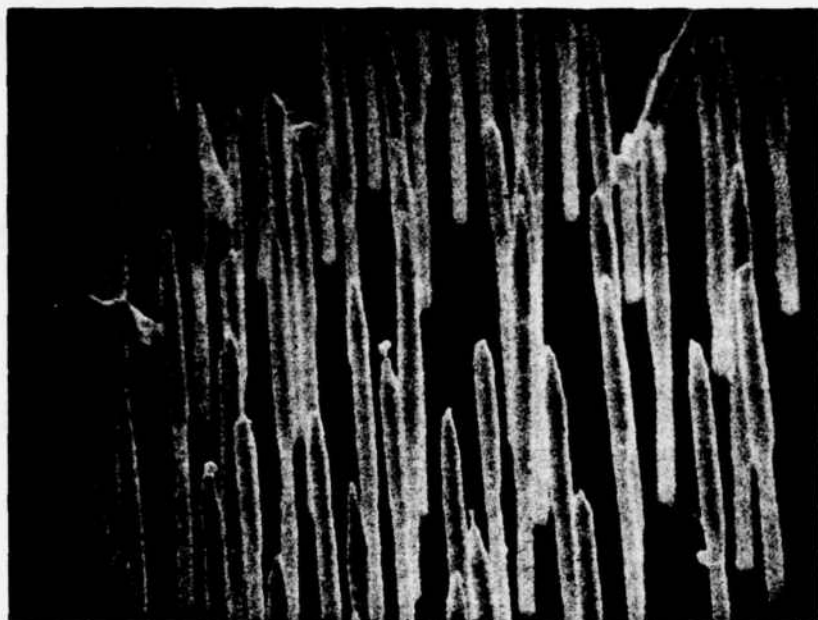


Figure V-18. Post-Emission Appearance of the Undamaged Pins on Cathode MM-6, X7900.

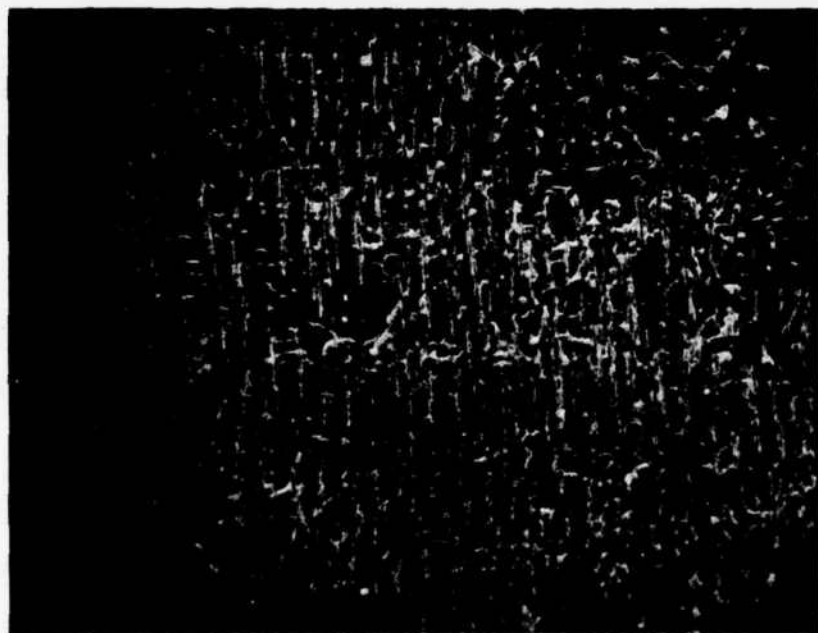


Figure V-19. Typical Area of Pin Damage on Cathode MM-6 Subsequent to Emission Testing, X1600.

20 mA ( $1.0 \text{ amp/cm}^2$ ) and held there by the TLD, the applied voltage would drop by over seven percent in less than an hour. This made it practically impossible to obtain accurate F-N plots at higher current levels. Of course, this problem of anode expansion manifested itself primarily at extremely small interelectrode spacings ( $\sim 50 \text{ }\mu\text{m}$ ), where only a small movement of the anode was necessary to produce a large percentage change in the spacing. At spacings greater than  $125 \text{ }\mu\text{m}$  the effect was very slight.

After examination in the SEM, the cathode was replaced in the test fixture, at a closer spacing, and the system evacuated once more. However, a resistance check of the diode prior to testing indicated that it was shorted. When the flange was removed and the spacing found to be unchanged, the flexing problem was recognized. All other tests in the water-cooled fixture were made with two spacers, as shown in Figure V-2.

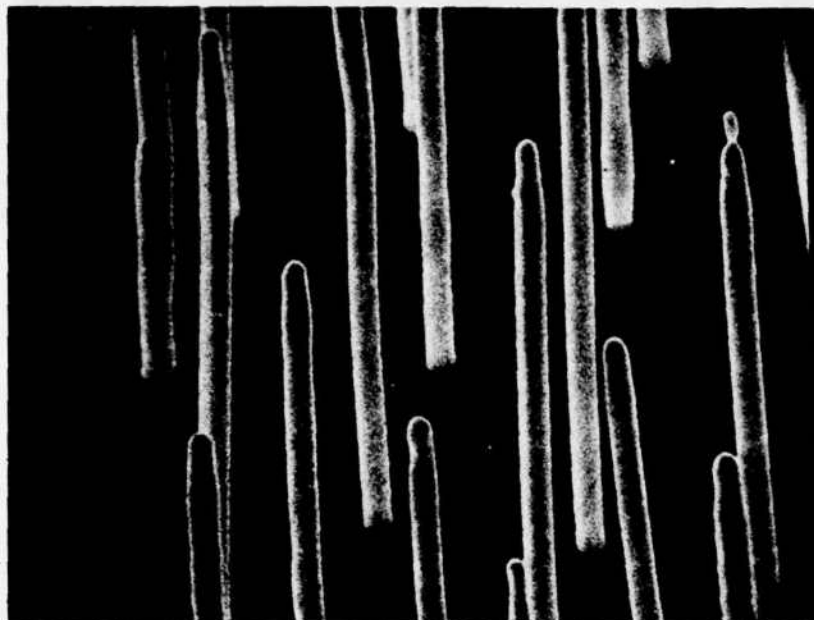
The next two tests, MM-7 and MM-8, were run with a slotted sapphire spacer placed between the anode and cathode to try and prevent reduction of the interelectrode spacing at higher power levels. MM-7 had relatively long, pointed pins, while MM-8 contained shorter pins which had been heated to  $1400^\circ\text{C}$  for several minutes to produce rounded, though somewhat non-uniform, pin

tips (Figure V-20). Unfortunately both tests were terminated prematurely when tungsten, either sputtered or evaporated from the pins, was deposited on the spacer, shorting the diode.

Test MM-9 was made using composite material grown at ORNL by Chapman et. al.<sup>2</sup> This material, shown in Figure 21, was dubbed the "pot-hole" structure after viewing an etched sample at low magnification in the SEM (the areas of  $UO_2$  matrix free of pins appear as depressions in the surface). It was hoped that the field enhancement of the pins around the edges of the "pot-holes" would be greater, because there were fewer surrounding pins to shield them, and that emission uniformity would thus be improved. Although subsequent examination of the cathode did reveal more pin damage around the edges of the pot-holes, there was no overall improvement in performance.

The cathode used for test MM-10 was the same one used for test MM-9, after being repolished and re-etched. The interelectrode spacing for this test, however, was set at not more than 0.002 inch (50  $\mu$ m). The results were remarkably similar to those of MM-6. The emission current was increased, with little or no arcing, to a current density of 1.0 amp/cm<sup>2</sup> and operated there for over 400 hours. The test was terminated after a total of 770 hours due to a

(a)



(b)

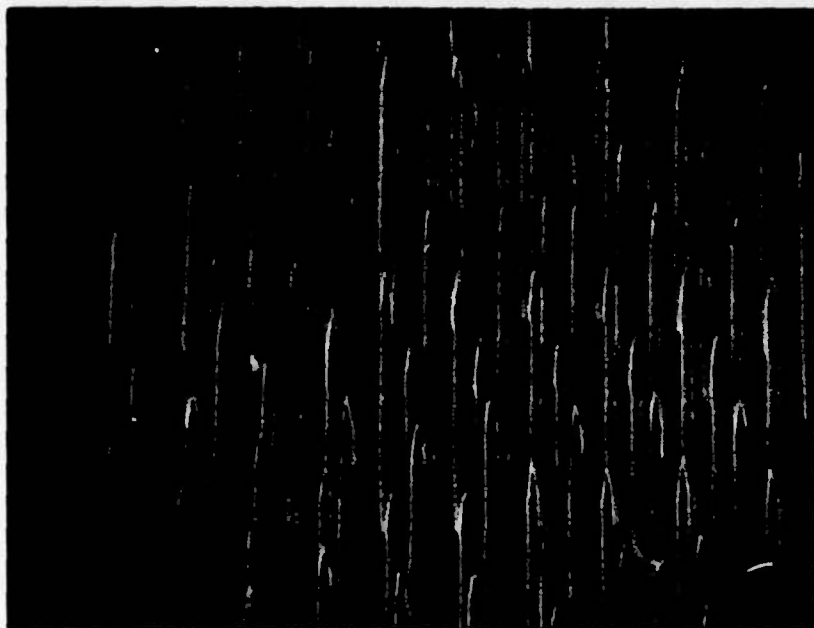
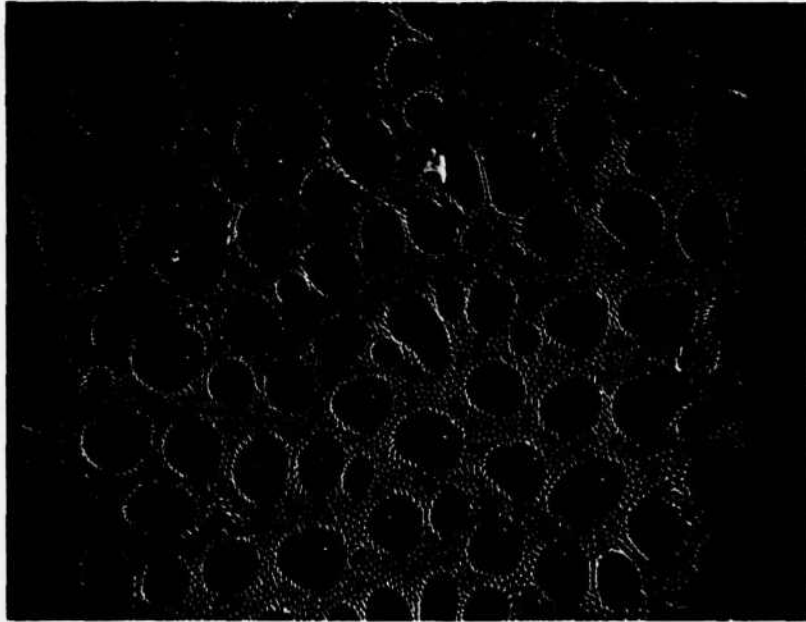


Figure V-20. Appearance of the Exposed Pins on Cathodes MM-7 and MM-8 Prior to Testing, (a) MM-7, X5200, (b) MM-8, X1200.

(a)



(b)



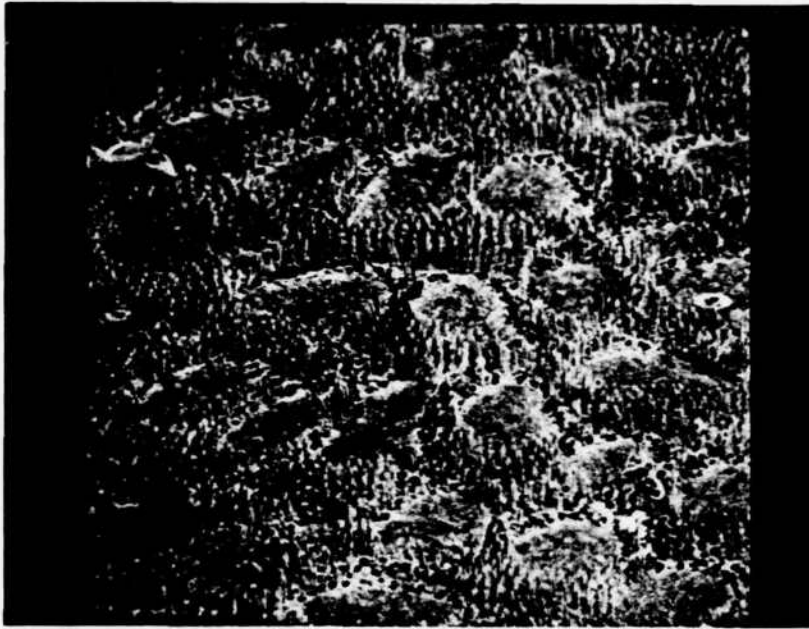
Figure V-21. Typical View of the "Pothole" Structure After Etching to Expose the Pins, (a) X220, (b) X1060.

short between cathode and anode. This was apparently due to build-up of tungsten on the anode, perhaps due to the relatively high pressure during this test (in excess of  $1 \times 10^{-7}$  torr).

Post emission SEM examination of the MM-10 cathode revealed that pin damage was indeed concentrated at the edges of the "pot-holes", although damage was not limited solely to the edge pins (Figure V-22). Approximately 20 percent of the pins on the cathode were damaged or destroyed, although the mechanism of pin failure was still not clear. Possible failure mechanisms will be discussed later. It was evident, however, that the pot-hole structure had improved emission uniformity slightly, and it seemed likely that the reduced interelectrode spacing had decreased the amount of pin damage. Note that the outline of the emitting area on the cathode can be clearly seen in Figure V-23.

One of the original goals of the project was to grow composites with array densities of  $1 \times 10^6$  pins/cm<sup>2</sup> or less. The impetus behind this was the analysis presented by Levine<sup>11</sup>, indicating that a significant reduction of the array density would produce a considerable increase in field enhancement at the pin tips.

(a)



(b)

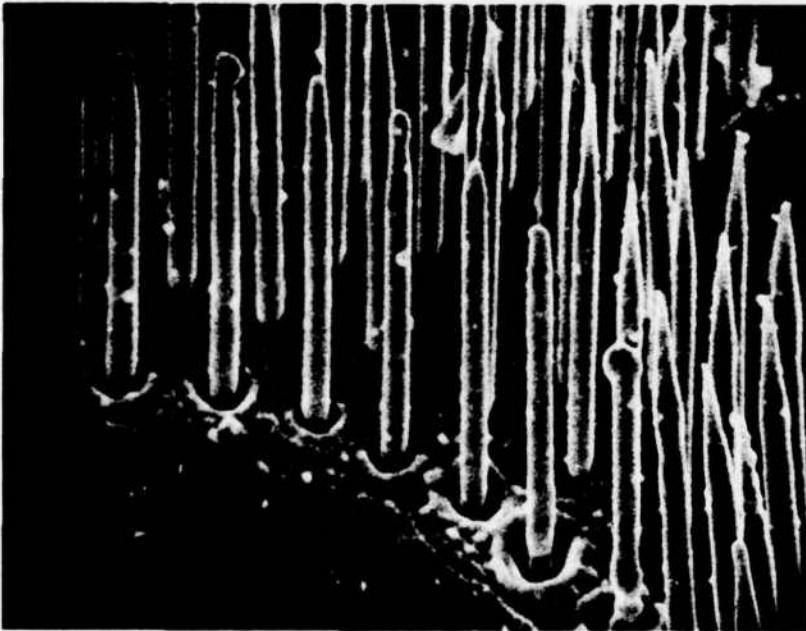


Figure V-22. Pin Damage on Cathode Observed After Testing MM-10, (a) X500, (b) X400.

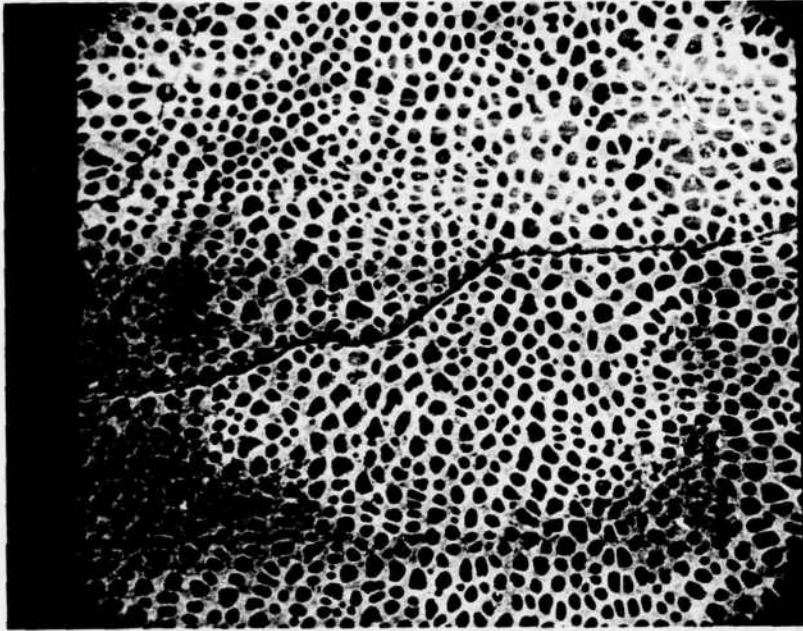


Figure V-23. View of Cathode After Test MM-10, Showing Outline of Active Emitting Area Under UF Anode, X50.

As discussed in Section III, composites with array densities as low as  $1.6 \times 10^6$  were successfully grown in Run LBH-21, and a sample of this material, designated MM-19, was emission tested. Although the material did not react to the pointing etch in the usual manner, etching in the 3:2 etch for one hour produced extremely uniform 10  $\mu\text{m}$  long cylindrical pins (Figure V-24). Based on the early tests with different pin geometries, the cylindrical pins were not expected to be a serious disadvantage. The interelectrode spacing was set as close to 0.001 inch (25  $\mu\text{m}$ ) as possible and high voltage applied to the diode. An initial emission current of 2 nA was measured as low as 800 volts, and was extremely stable. The current was increased fairly rapidly until it reached 5.0 mA (250 mA/cm<sup>2</sup>) @ 1.0 kV after 48 hours.

Thermal expansion of the anode began to become evident at this point (Figure V-13). After 53 hours the current was increased further to 10 mA (0.5 A/cm<sup>2</sup>). The voltage decreased as low as 520 volts for several minutes, when the diode suddenly shorted. When the power was shut off, the anode cooled and the spacing increased enough to remove the short. High voltage was re-applied and the current was increased to 7.5 mA (375 mA/cm<sup>2</sup>). The voltage eventually stabilized at approximately 600 volts, but a F-N plot made at

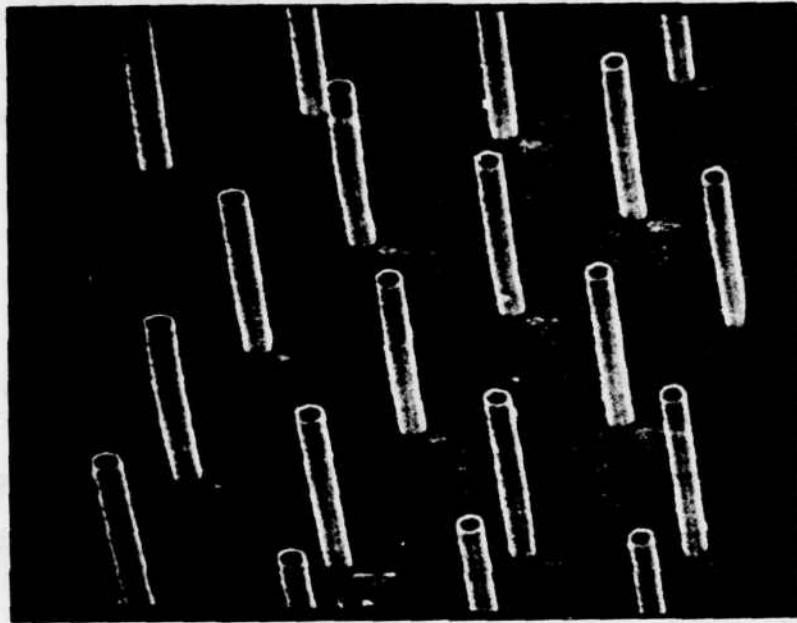


Figure V-24. Appearance of Exposed Pins on Cathode MM-19 Prior to Emission Testing, X3000.

this point showed a 100% increase in slope over the previous plots.

It was obvious that further increases in current would be impossible unless the interelectrode spacing was increased. So, the test fixture was removed from the vacuum system and the spacing was increased to  $\sim 0.005$  inch (125  $\mu\text{m}$ ) without removing the cathode from its mount. Observation of the cathode under the binocular microscope at 30x revealed little, if any, pin damage.

The voltage required to obtain 1 mA (55 mA/cm<sup>2</sup>) was about four times that needed at the closer spacing, and the current was noisier as well. Arcing was first observed, both on the electrometer and ion gauge, at the 4 mA (220 mA/cm<sup>2</sup>) level. It increased in frequency and intensity as the current was increased, with major arcs occurring at 10 to 15 mA (550 to 830 mA/cm<sup>2</sup>). Since the slope of a F-N plot made at the 10 mA level was almost six times that of an earlier one, and since the emission current had begun to decrease for a given applied voltage, the cathode was removed for examination.

The SEM revealed that 90% or more of the pins had been destroyed. The remnants of the pins were all practically identical, consisting of craters, with melted rims, in the oxide matrix (Figure V-25). At

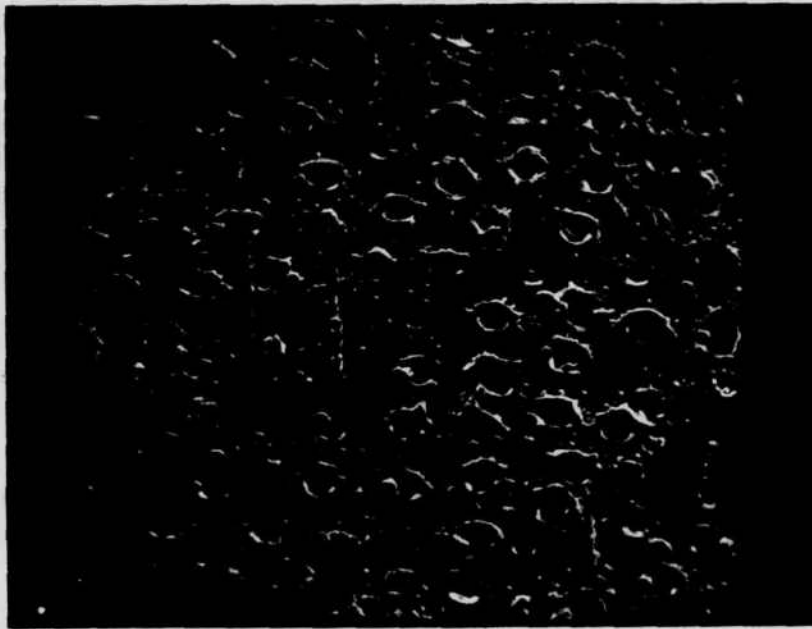


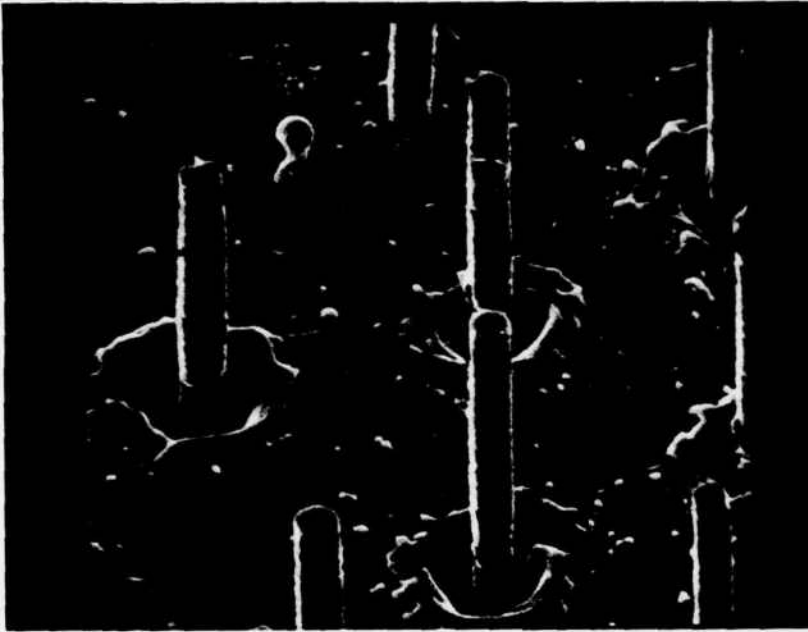
Figure V-25. Post-Emission Damage on Cathode MM-19B,  
Near Center of Active Emitting Area,  
X1500.

the edge of the emission area, pins were observed in various stages of failure (Figure V-26a). Almost without exception, the pins were melted to varying degrees at the base, showing considerable reaction at the  $\text{UO}_2$ -W interface, while the pin tips appeared unaffected (Figure V-26b). In previous tests where melting of the matrix around the pin base was observed, the pin itself showed less reaction with the  $\text{UO}_2$  matrix even when the pin tip was melted.

Neither of the tests of cathodes with rounded pin tips, MM-5 and MM-8, had been very definitive. The interelectrode spacing on MM-5 had been quite large, which probably contributed to its early failure, while MM-8 was terminated prematurely due to high surface conduction on the  $\text{Al}_2\text{O}_3$  spacer. Intuitively, the annealing process should improve pin tip uniformity, and thus emission uniformity, of the tungsten pin arrays.

Two more attempts at annealing the pin tips were only partially successful. Although the pin tips were rounded slightly, the pins were badly contaminated by nickel from the Mo-Ni braze used to attach the composite to the Mo support rod. Designated MM-17 and MM-18, the cathodes were tested anyway, but the results were disappointing, with neither emitter

(a)



(b)

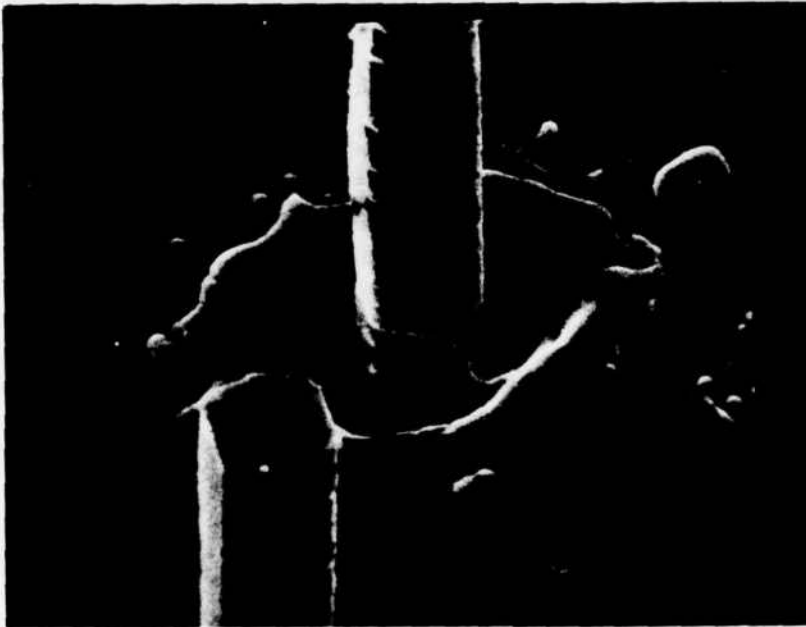


Figure V-26. Typical Pin Damage Observed Near Edge of Active Emitting Area on Cathode MM-19B, (a) X6500, (b) X15000.

producing more than  $0.33 \text{ A/cm}^2$ . It is likely, however, that the nickel contamination contributed to the early failure of many of the pins.

Toward the end of the project, since the cause of non-uniform emission from the arrays had still not been discovered, the decision was made to test one more cathode with annealed pins. The wafer used as the cathode for test MM-31 was from the same run as MM-19, i.e. LBH-21, having a pin density of  $1.6 \times 10^6 \text{ pins/cm}^2$ . To avoid the previous difficulty of the braze material vaporizing and contaminating the pins, the wafer was processed without brazing it to a support. After etching to expose the pins to a height of  $5 \text{ }\mu\text{m}$  (Figure V-27), the wafer was heated in  $\text{H}_2\text{-N}_2$  to a temperature of  $1500^\circ\text{C}$  for 10 minutes. The results of the heat treatment were very encouraging (Figure V-28), producing pins with hemispherical tips having radii equal to that of the pin. The pins were unquestionably the most uniform in size and tip shape of any cathode tested to date. The wafer was attached to an aluminum SEM stub using silver paste and mounted in the water-cooled diode test fixture at a spacing of  $\sim 0.003 \text{ inch}$  ( $75 \text{ }\mu\text{m}$ ).

The voltage necessary to activate the emitter was  $\sim 1.8 \text{ kV}$ , somewhat higher than MM-18, which was set to approximately the same interelectrode spacing.

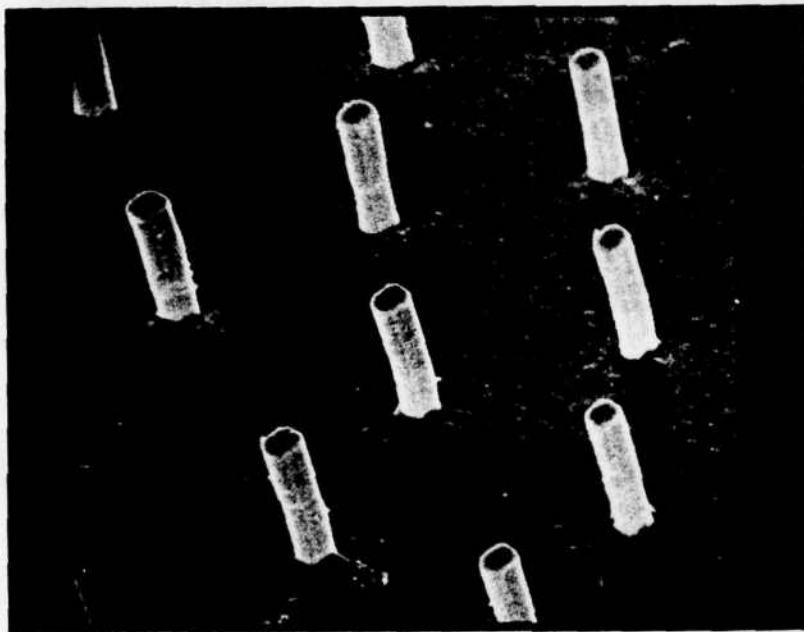
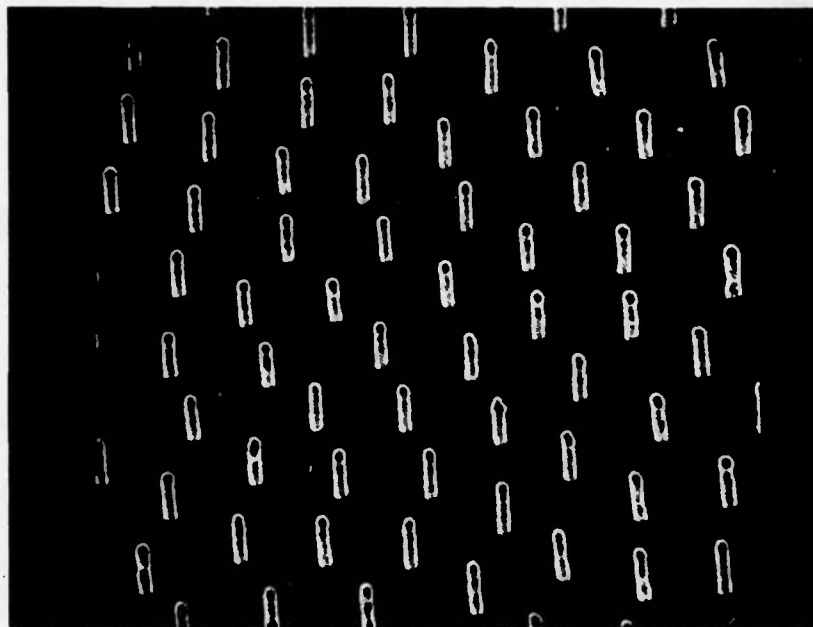


Figure V-27. Exposed Pins of Cathode MM-31  
Prior to High-Temperature Anneal,  
X5000.

(a)



(b)

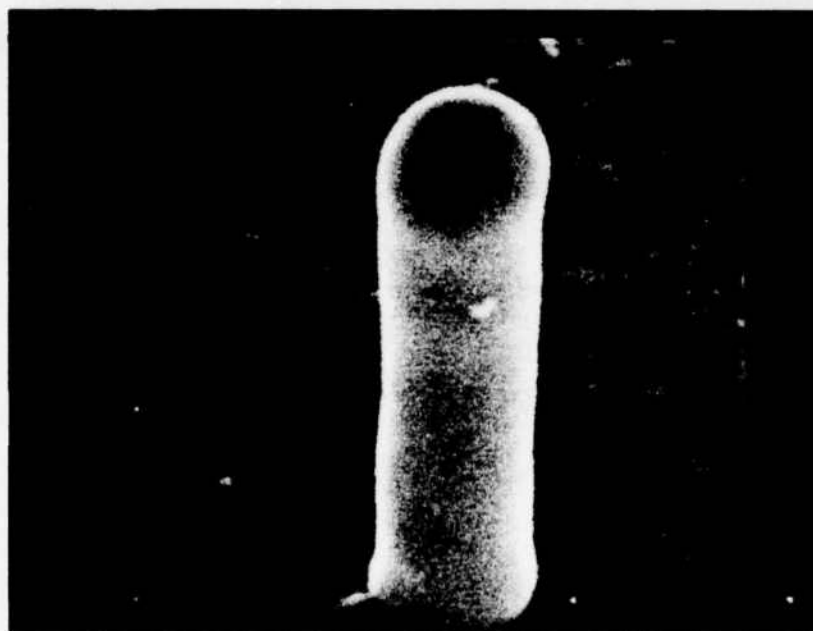


Figure V-28. Appearance of Tungsten Pins on MM-31 After Annealing in  $H_2$  for 15 Minutes @  $1400^{\circ}C$ , (a) X1500, (b) X20000.

This was attributed to the lower field enhancement of the rounded pin tips and was verified by the higher slope of F-N plots made later. Despite a sudden decrease in voltage, apparently due to an arc, the voltage necessary to produce 250  $\mu$ A was still relatively high, at 1.6 kV. Based on the results of previous experiments it was clear that, at this voltage, pin damage would soon begin to occur. So the cathode was removed, examined in the SEM, and replaced in the test fixture at a closer spacing. No trace of any pin damage could be found with the SEM.

With the interelectrode spacing reduced to  $\sim 0.001$  inch (25  $\mu$ m), a stable current of 7  $\mu$ A was measured @ 550 volts. The current was quickly brought back to its previous level of 250  $\mu$ A, this time requiring a voltage of only 840 volts; about half that required at the larger spacing. As the current was increased to 600  $\mu$ A and above, thermal expansion of the anode became evident. At 1.27 mA, the voltage had dropped to 630 volts, and at 2.5 mA it was down to 470 volts (Figure V-13).

It was clear at this point that further increases in current would cause the anode to expand enough to short the diode, just as in test MM-19. The interelectrode spacing for both of the tests was apparently

quite close, although that for MM-19 was probably slightly larger, judging by the percentage change in voltage for an equivalent change in current. Since further current increases were impossible in the cw mode, the decision was made to apply a low-duty-cycle pulse voltage to the cathode. Hopefully, this would prevent anode heating and expansion and permit further current increases.

The pulse circuit diagrammed in Figure V-10 worked remarkably well, producing pulses of 480  $\mu$ A @ 920 volts, with a duty cycle of less than one percent. At an emission current level of 3 mA @ 1.2 kV, and a duty cycle of  $\sim$ 0.2 percent (100  $\mu$ sec pulse width), there was no evidence at all of anode heating. Thus, from the standpoint of maintaining a constant interelectrode spacing, the pulse test could be considered a complete success.

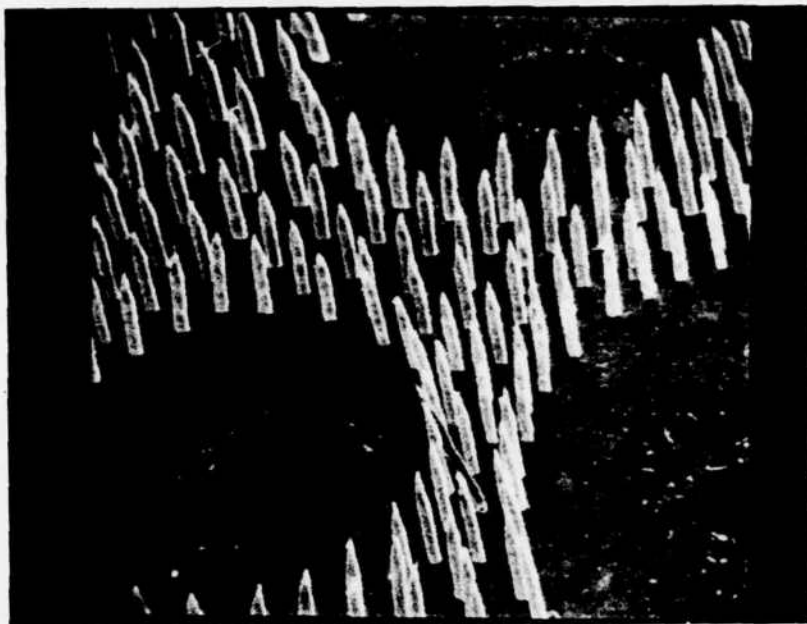
Because of the lower field enhancement of the rounded tips, however, the applied voltage was once more in the range where pin damage normally occurred. This manifested itself very quickly, for the diode shorted during the night, (operating at 3 mA), (165 mA/cm<sup>2</sup>), apparently due to an arc(s). Fortunately, the material causing the short was successfully dislodged without removing the test fixture from the

chamber by simply tapping on the exterior part of the cathode support.

As the current was increased to 4 mA ( $225 \text{ mA/cm}^2$ ) and then to 5 mA ( $275 \text{ mA/cm}^2$ ), more arcing was observed on the oscilloscope. The emitter finally shorted once more and was removed for examination in the SEM. The damage revealed by the SEM was very similar to that which occurred during test MM-19. Most of the pins under the anode (99 percent) were destroyed, leaving melted craters on the surface. With differences in pin height and pin tip diameter of less than  $0.1 \mu\text{m}$  and with a maximum average current per pin of  $\sim 160 \text{ nA}$ , the results lead to the conclusion that either emission uniformity is controlled by differences in pin height and/or pin tip radius much smaller than this, or that some other factor is responsible.

An effort was made to examine the effect of work function on emission by coating an etched sample with platinum, using electron beam evaporation. The cathode was the same one used for test MM-10, the "pot-hole" structure, re-ground and re-etched to expose  $10 \mu\text{m}$ -long pointed pins (Figure V-29). After thorough cleaning in distilled water and methanol, the surface was coated with  $\sim 500 \text{ \AA}$  of a platinum-20% rhodium alloy (Figure V-30).

(a)



(b)

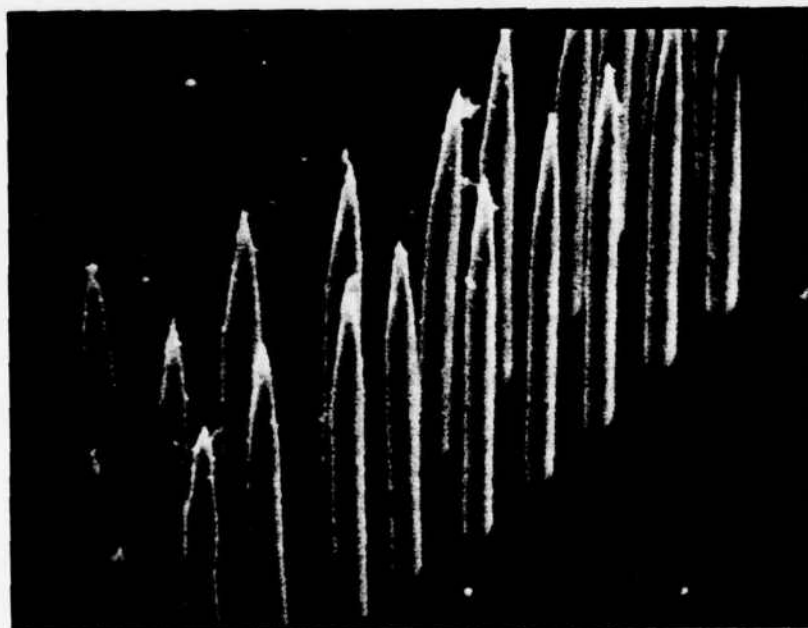
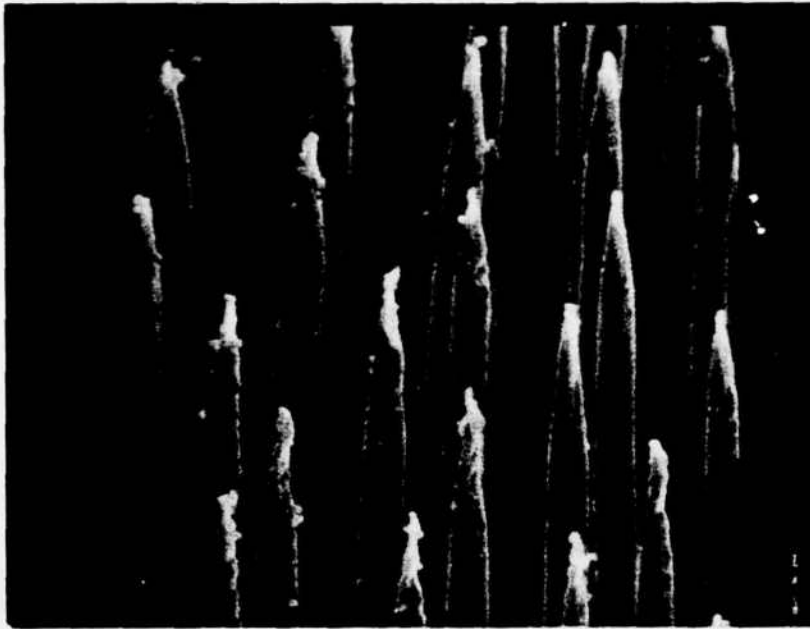


Figure V-29. Exposed Pins on Cathode MM-32 Prior to Coating with Platinum, (a) X2000, (b) X6000.

(a)



(b)

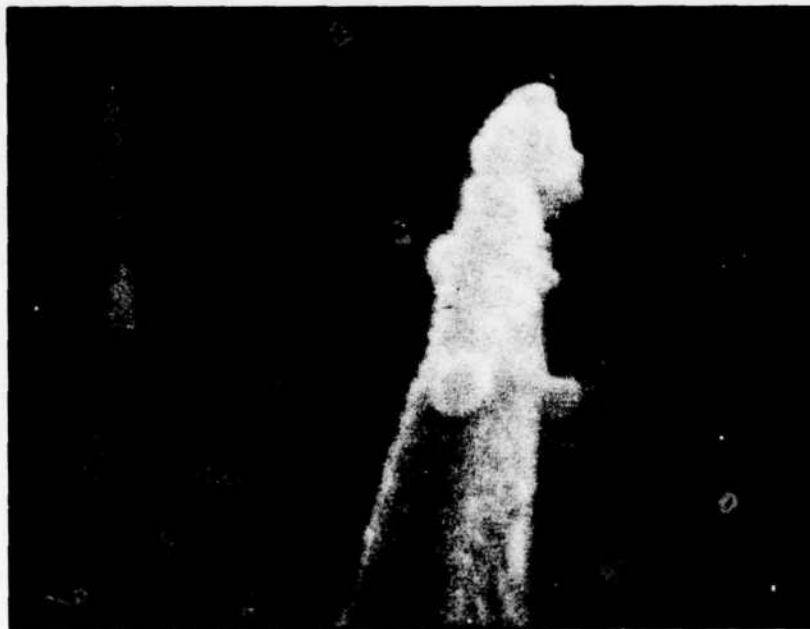


Figure V-30. Pin Tips on Cathode MM-32 After Application of Platinum Coating, (a) X7000, (b) X50,000.

The cathode was tested in the vacuum system shown in Figure V-7, under a 0.060 inch (1.5 mm) diameter UF anode. The anode was 3 inches long, and was attached to the linear motion feedthrough to permit accurate setting of the interelectrode spacing and variation of that spacing if necessary during operation of the diode.

The interelectrode spacing was set initially at  $\sim 0.001$  (25  $\mu\text{m}$ ) inch and voltage applied to the anode. At 700 volts the emitter produced a very noisy 0.1  $\mu\text{A}$  of current. The noise diminished, however, by the time the current had reached 1.5  $\mu\text{A}$  @ 1.27 kV, and stability became excellent. The voltage, however, seemed high for this current and interelectrode spacing.

When the current had been increased to 20  $\mu\text{A}$  @ 1.4 kV, the interelectrode spacing was reduced to  $\sim 0.0005$  inch (12  $\mu\text{m}$ ). This produced a 40 percent drop in applied voltage, to 840 volts, to obtain 20  $\mu\text{A}$  of emission current. Over the next 10 days, the current was gradually increased to 2 mA at 900 volts. Because of the degree of thermal expansion of the anode, each time the current was increased, the interelectrode spacing had to be increased as well to prevent shorting of the diode. When the current was increased to 3 mA, however, the frequency of arcs became much higher and the diode finally shorted.

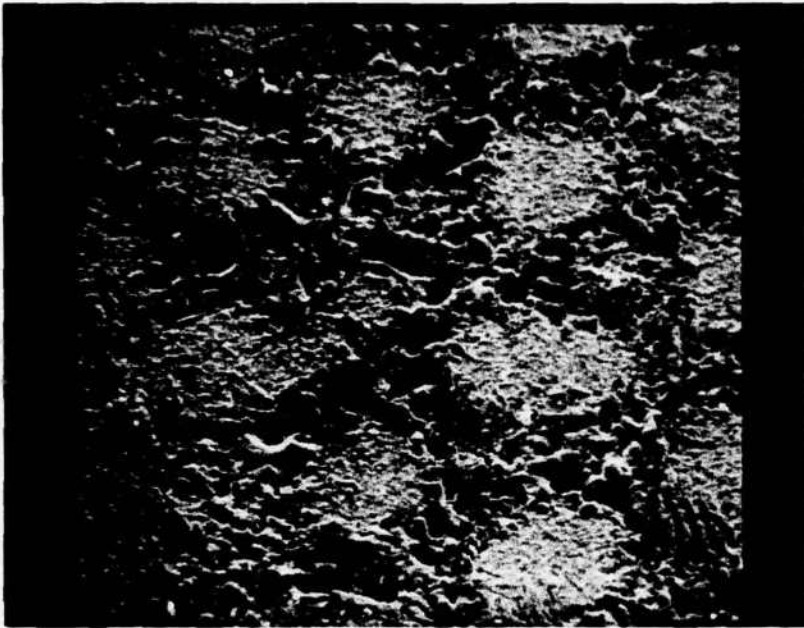
The cathode was removed at this point for SEM examination. It revealed almost complete destruction (~99%) of the pins under the anode (Figure V-31a). Examination of the cathode at the edge of the emission area revealed numerous partially melted pins, some melted at the top, others melted at the base. In the case of those melted at the base, the platinum coating had vaporized from the pin tip and was melted back from the base of the pin (Figure V-31b). In some cases, loss of the platinum was the only evidence that the pin had been emitting. Vaporization of platinum from the base of the pins revealed that, as in MM-10, emission occurred primarily from the pins at the edge of the UO<sub>2</sub> "islands".

#### F. ANALYSIS OF UF ANODE TEST RESULTS

The results of the tests using the 0.060 inch diameter UF anode are summarized in Table V-III. The "Growth Run" numbers serve to identify the ingot from which the composite wafer was cut. Some of the growth runs were made in the course of previous projects, so the numbers may be unfamiliar.

The estimate of macroscopic electric field was obtained by simply dividing the diode voltage at 55 mA/cm<sup>2</sup> by the estimated interelectrode spacing. The

(a)



(b)



Figure V-31. Appearance of Cathode MM-32 After Emission Testing, (a) Near Center of Emitting Area, X600, (b) Near Edge of Emitting Area, X6500.

Table V-III. Summary of Cathode Geometries Used and Results of the Emission Tests with the UF Anode.

TEST NO.	GROWTH RUN NO.	CATHODE GEOMETRY		INTER ELECTRODE SPACING ( $\mu\text{m}$ )	DIODE VOLTAGE (kV) NEEDED TO PRODUCE:		MACROSCOPIC ELECTRIC FIELD $\Phi$ 55 mA/cm <sup>2</sup> (10 <sup>5</sup> V/cm)	TIME OF OPERATION @ 1255 mA/cm <sup>2</sup> (hours)	FIELD ENHANCEMENT FACTOR ( $\beta$ ) (cm <sup>-1</sup> )	MAXIMUM ARRAY CURRENT DENSITY (A/cm <sup>2</sup> )	TOTAL EMITTING AREA (sq cm)	
		ARRAY DENSITY (10 <sup>5</sup> pin/cm <sup>2</sup> )	PIN HEIGHT ( $\mu\text{m}$ )		PIN TIP SHAPE	550 mA/cm <sup>2</sup>						55.0 mA/cm <sup>2</sup>
MM-1	----	9.5	12	Cylindr	300±50	3.3	3.0	3.78	1.3	-----	0.66	-----
MM-3	----	10.7	10	Pointed	125±25	2.4	2.9	2.2	1.8	8.4x10 <sup>5</sup>	0.77	6x10 <sup>-14</sup>
MM-4	----	10.7	17	Cylindr	125±25	2.7	2.4	1.9	1.5	1.1x10 <sup>5</sup>	0.22	1x10 <sup>-13</sup>
MM-5	----	10.7	7	Round**	155±25	2.3	3.0	3.3	2.1	1.1x10 <sup>5</sup>	0.08	2x10 <sup>-14</sup>
MM-6	H-6	20.5	8	Pointed	25±10	0.4	0.45	0.56	2.2	2.4x10 <sup>5</sup>	1.18	2x10 <sup>-11</sup>
MM-7	H-6	20.5	10	Pointed	50±10	0.7	0.9	1.1	2.2	1.8x10 <sup>5</sup>	0.47	4x10 <sup>-13</sup>
MM-8	LBH-5A	8.9	9	Round†	20±10	0.5	0.6	0.7	3.5	4.5x10 <sup>5</sup>	0.14	5x10 <sup>-14</sup>
MM-9	ORNL-136	4.4*	15	Pointed	100±30	0.67	1.1	1.6	1.6	1.7x10 <sup>5</sup>	0.30	1x10 <sup>-12</sup>
MM-10	ORNL-136	4.4*	10-11	Pointed	40±10	0.60	0.5	0.79	2.0	2.2x10 <sup>5</sup>	1.11	5x10 <sup>-11</sup>
MM-17	LBH-5A	9.0	10	Round†	60±10	1.6	2.8	2.0	3.3	7.0x10 <sup>5</sup>	0.05	6x10 <sup>-14</sup>
MM-18	LBH-5A	8.9	9	Round†	75±10	2.42	2.5	2.0	2.7	1.6x10 <sup>5</sup>	0.33	3x10 <sup>-14</sup>
MM-19A	LBH-21	1.6	9	Cylindr	<25	0.69	0.91	0.94	>3.8	1.8x10 <sup>5</sup>	0.55	4x10 <sup>-12</sup>
MM-19B	LBH-21	1.6	9	Cylindr	125±25	0.4	2.84	4.09	3.3	3.0x10 <sup>5</sup>	0.30	7x10 <sup>-13</sup>
MM-31	LBH-21	1.6	5	Round†	<20	0.59	--	1.0†	>5.0	7.7x10 <sup>5</sup> ‡	0.27‡	1x10 <sup>-14</sup>

\* Average density including area of "pot-holes" free of pins.

\*\*Etched to produce cyl. pins and then ion-milled for 10 minutes.

†Etched to produce pointed pins and then heated in H<sub>2</sub>-N<sub>2</sub> for 15 minutes @ 1400°C.

‡Pulse data.

maximum array current density was calculated by dividing the maximum emission current by the anode area.

Although the resulting current density may be conservative by as much as 40%, (since the anode face is not perfectly flat), it is useful as a means of comparison. The field enhancement factor and the total emitting area were calculated from the Fowler-Nordheim plots by the methods discussed earlier.

Comparison of the test results is complicated by the fact that several parameters of cathode geometry were normally changed from one test to another. Nevertheless, despite the difficulty in separating the effects of different parameters, a number of conclusions can be drawn from the trends observed.

#### 1. Pin Tip Shape

The results indicate that sharply pointed pins produce the best emitter performance. The cathodes in tests MM-6 and MM-10 both contained pointed pins and both achieved array current densities of more than one amp/cm<sup>2</sup> with relatively little pin damage. For comparison, note that neither MM-19a nor MM-31 produced as much emission current and both suffered extensive pin damage. Furthermore, the latter two cathodes were both operated at closer interelectrode spacings than either MM-6 or MM-10.

The effect of tip geometry on total emitting area indicates that the pointed pin tips produce an increase in total emitting area. This is somewhat surprising, since one would expect the emitting area to be greater on the rounded or cylindrical pin tips. Of course there is no way of determining whether the increased emitting area for the pointed geometry is due to a greater emitting area per pin or to a greater number of pins emitting. In either case, though, the net result should be a reduction in pin damage and this was indeed observed.

The pin tip shape seemed to have very little effect on the field enhancement factor ( $\beta$ ). Although the pointed pins did have slightly higher values of  $\beta$ , the difference was not nearly as large as equation (11) predicts, assuming the emitting area radius is the same as the pin tip radius.

## 2. Pin Height

The effect of pin height on emitter performance has not yet been established, either in theory or by the present tests. Comparison of tests MM-3 and MM-4 indicates that taller pins may produce slight increases both in  $\beta$  and emitting area. This is particularly significant since the pins on MM-4 were not pointed. On the other hand, there is no indication that the 5  $\mu\text{m}$  pins on MM-31 produced any significant reduction

in the field enhancement. Thus, until more knowledge of the effect of pin height becomes available, there seems to be no reason not to continue using pin heights of 10 to 15  $\mu\text{m}$ , since pins of this length give satisfactory results and can be obtained with reasonably short etch times.

### 3. Array Density

Equation (11) predicts that the value of  $\beta$  will be very sensitive to the pin separation distance,  $a$ . For example, a change in pin spacing from 3  $\mu\text{m}$  to 8  $\mu\text{m}$ , corresponding to a decrease in array density from  $1.0 \times 10^7$  to  $1.6 \times 10^6$  pins/cm<sup>2</sup>, should increase the value of  $\beta$  by a factor of 2.9, assuming an interelectrode spacing of 25  $\mu\text{m}$  and a tip radius of 1000  $\text{\AA}$ . This would produce an increase in emission current density by a factor of  $\sim 10^5$  A/cm<sup>2</sup>.

The predicted improvement in emission performance was not observed in the tests with the low-array density composites. Comparison of tests MM-8 and MM-31, for example, shows a decrease in the value of  $\beta$  of  $\sim 80$  percent for the low-density cathode. However, if one takes into account the larger tip radius of the low-density cathode ( $\sim 0.5 \mu\text{m}$ ), equation (11) predicts a 70 percent decrease in the value of  $\beta$ . Thus the performance of the low-array-density cathode was

degraded by the large pin tip radii and seems to be quite close to that predicted by theory.

Further evidence of the beneficial effect of larger pin separation was observed indirectly in test MM-10. The enhanced emission at the edges of the pot-holes could only be due to the fact that the edge pins had fewer neighboring pins, corresponding to an effective reduction in the array density.

#### 4. Interelectrode Spacing

Together with the pin tip shape, the interelectrode spacing seemed to have the most pronounced effect on emitter performance. A comparison of MM-9 and MM-10 or MM-19A and MM-19B leaves little doubt that reducing the spacing increases both the field enhancement and the emitting area. The increase in  $\beta$  due to decreased interelectrode spacing is predicted by equation (11), and the experimental results are surprisingly close to those predicted by Levine's theory. For example, in the case of MM-9/MM-10, the value of  $\beta$  decreased 21% at the larger spacing. Assuming a  $100 \text{ \AA}$  tip radius for the pointed pins, equation (11) predicts a 23% decrease in  $\beta$ . For the case of MM-19, with  $5000 \text{ \AA}$  pin tip radii, the theory predicts an 84% drop in  $\beta$  when  $d$  is increased from 25 to 125  $\mu\text{m}$ , whereas the actual reduction in  $\beta$ , calculated from the F-N plots, was 74%.

It is interesting to note that the increase in  $\beta$  with decreasing interelectrode spacing, predicted by Levine and observed in these tests, is opposite to the results observed by other workers<sup>13</sup>, using plane parallel tungsten electrodes.

#### 5. Platinum Coating

Test MM-32 left little doubt that uncoated tungsten, even with one or more layers of adsorbed oxygen, is still the preferred material for the field emission tips. With the interelectrode spacing set initially at about 25 microns, 1.3 kV was required to produce 10  $\mu$ A of emission current. This was at least twice the voltage necessary to obtain the same emission from MM-10, which had pins of approximately the same height. The higher voltage required was reflected in the relatively low array current density achieved and the large degree of pin damage on the cathode (Figure V-31a).

The expected result of coating the pins with platinum was to reduce the work function, since oxygen should not be so strongly bound to platinum as it is to tungsten. The slope of the F-N plot for MM-32 was about the same as for the uncoated pins of MM-10 (Table V-III). From this fact one might conclude that the increased field is due both to an increase in work function and a decrease in field

enhancement, since change in only one of these parameters would have affected the value of the slope. The higher work function was probably due to the fact that the pins could not be adequately cleaned prior to applying the platinum coating. It is not surprising that the application of a coating over oxygen-contaminated pins would further increase the work function. The coating may have also significantly lowered the value of  $\beta$  by collecting on the pin tips and increasing their radius (Figure V-30b). Furthermore, it is quite likely that vaporization of platinum from the pins, and its subsequent ionization, contributed to the increase in pin damage over that observed in MM-9 and MM-10.

Based on the results summarized in Table V-III, then, a picture of the optimum emitter geometry begins to take shape: clean tungsten pins, at least 10 to 15  $\mu\text{m}$  tall, with sharply pointed tips; interelectrode spacings of 50  $\mu\text{m}$  or less; and low array densities perhaps with artificially produced edge pins such as are found in the pot-hole structure.

#### G. TESTS OF STYLUS-SHAPED CATHODES

The stylus-shaped cathodes were tested in several types of apparatus. Tests MM-20 and MM-21 were conducted in the water-cooled diode test fixture; MM-24 was tested in a simple, locally constructed gun;

while MM-28 and MM-29 were tested in the RCA Gun described earlier. Each of the tests contributed to an understanding of the operating characteristics of the larger-area arrays. A summary of the results of tests MM-20, -21, and -24 is given in Table V-IV.

#### 1. Diode Geometry

The cathode used for test MM-20 was a wafer from Run LBH-21, copper brazed to a 1/16 inch diameter Mo rod. It was carefully masked with parafin and etched so that only ~30 pins with cylindrical tips were exposed at the apex of the cone. The 8 to 10 pins at the very tip were approximately 12 to 15 microns tall, spaced approximately 8 microns apart (Figure V-32). Each of these pins was carefully indexed and photographed prior to emission testing (Figure V-33). The cathode was tested at an interelectrode spacing of approximately 0.001 inch (25  $\mu\text{m}$ ) under the flat, polished Mo anode.

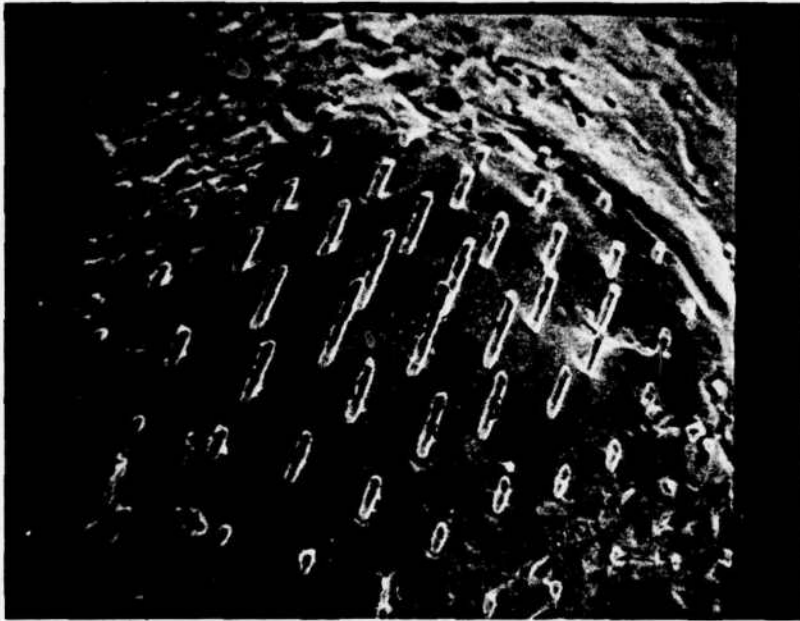
The cathode produced a total current of 17  $\mu\text{A}$  before an apparent arc occurred, as observed by a flick of the electrometer needle. The sample was removed from the vacuum system and examination in the SEM revealed that one of the two tallest center pins had indeed been destroyed (Figure V-34). The fact that pin c was completely vaporized, while all but

Table V-IV. Summary of Stylus Cathode Tests.

Test No.	No. of Pins At Tip	Est. No. of Pins Emitting	Maximum Emission Current ( $\mu\text{A}$ )	Inter-Electrode Spacing* ( $\mu\text{m}$ )	Est. Current Per Pin ( $\mu\text{A}$ )	Field Enhancement Factor ( $\text{cm}^{-1}$ )	Total Emitting Area ( $\text{sq cm}$ )
MM-20	30	9	13.5	25	1.5	$1 \times 10^5$	$2 \times 10^{-15}$
MM-21	7	7	28.0	25	4.0	$4 \times 10^5$	$8 \times 10^{-16}$
MM-24	100	---	100.0	280	---	$9 \times 10^5$	$4 \times 10^{-15}$

\* Tests MM-20 and MM-21 tested with a planar anode. Test MM-24 tested in a gun geometry (Fig. V-38).

(a)

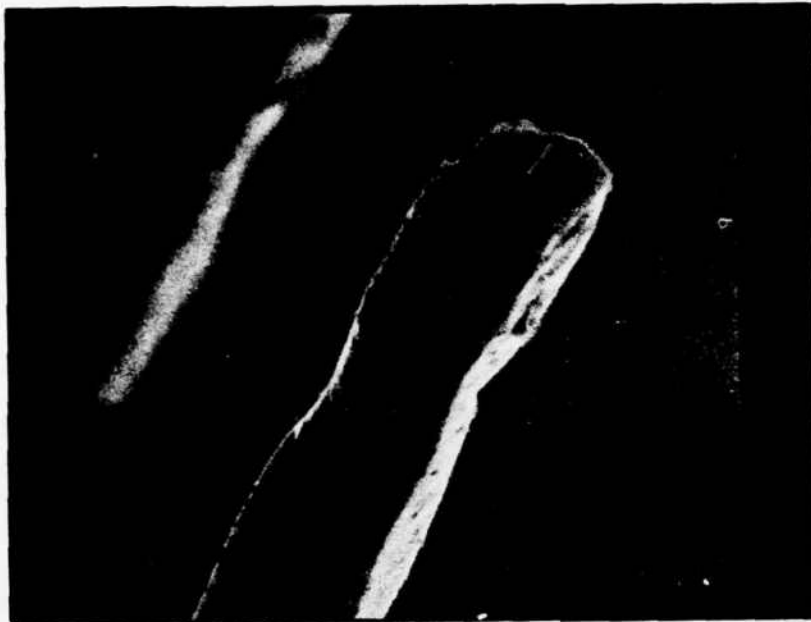


(b)



Figure V-32. View of Exposed Pins at the Tip of the Stylus Cathode Used in Test MM-20, (a) X1500, (b) X11000.

(a)



(b)

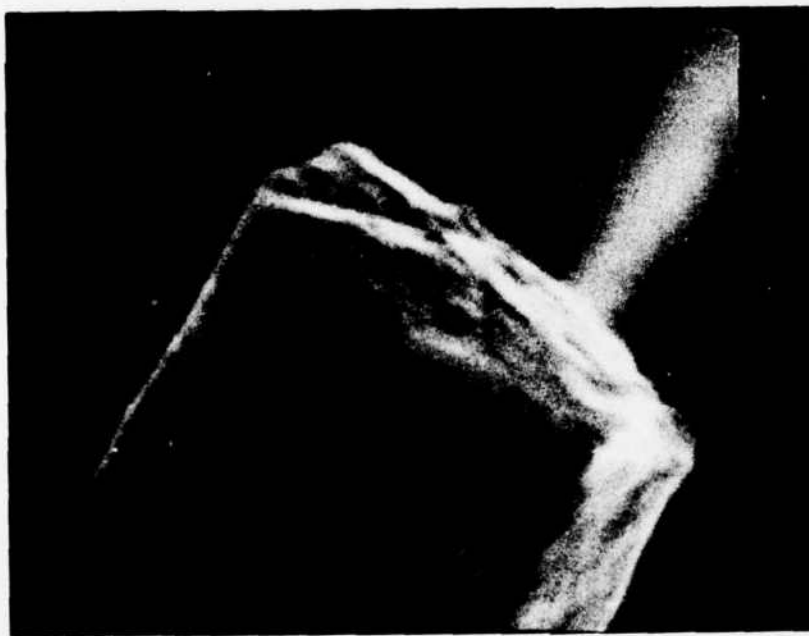


Figure V-33. Appearance of Pin Tips on Cathode MM-20 Prior to Emission Testing, (a) Pin c, X20000, (b) Pin a, X66000.

AD-A148 435

MANUFACTURING METHODS FOR THE PRODUCTION OF FIELD  
EFFECT ELECTRON EMITTERS FROM OXIDE-METAL COMPOSITES  
(U) GEORGIA INST OF TECH ATLANTA A T CHAPMAN DEC 77

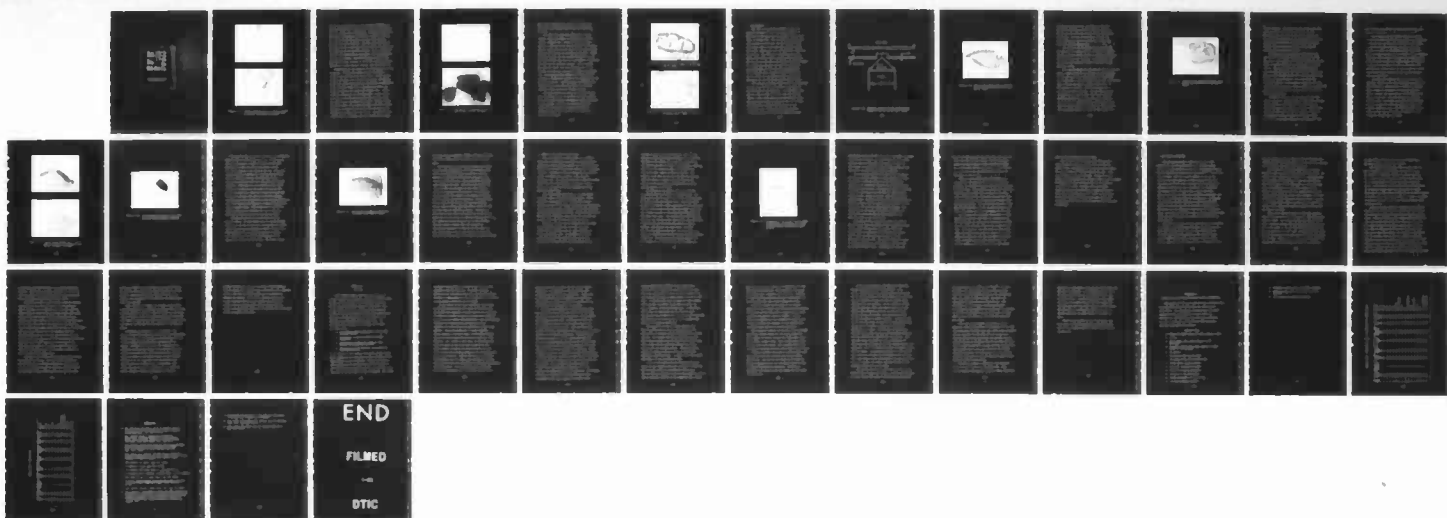
3/3

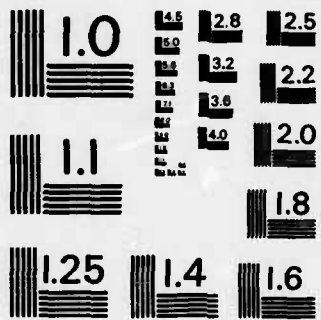
UNCLASSIFIED

DAAH01-75-C-0852

F/G 9/1

NL





MICROCOPY RESOLUTION TEST CHART  
 NATIONAL BUREAU OF STANDARDS-1963-A

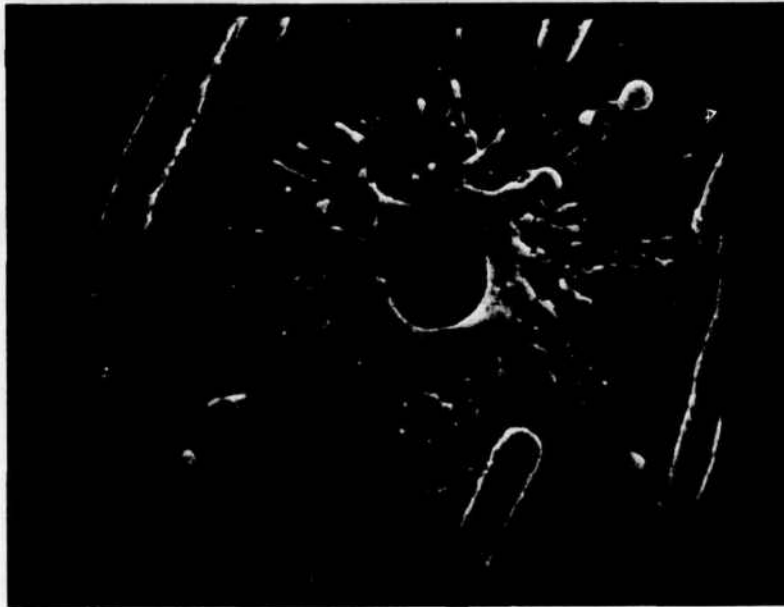
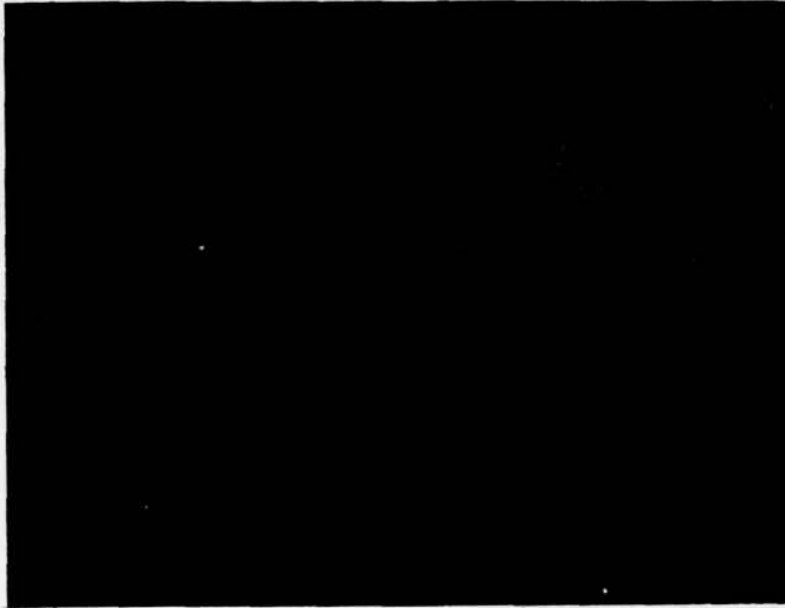


Figure V-34. Damage Produced at Tip of Stylus Cathode in Test MM-20 When Pin c Was Destroyed by an Arc, (a) X1500, (b) X6000.

two of the remaining pins on the tip were undamaged, is strong evidence that arcs are initiated at the individual pin tips rather than at the anode. An anode-initiated arc would have undoubtedly affected most of the pins on the tip, since all of the taller pins fit into a circle of less than 20  $\mu\text{m}$  diameter. The fact that the arc was initiated at pin c may also indicate that it was producing the majority of the emission current. On the other hand, since it was surrounded by tall pins, (and thus shielded) to a greater extent), the emitting area on the tip may have been smaller, causing it to reach a critical current density at a lower emission current (see sub-section I).

Examination of the anode in the metallograph was also revealing. A dark ring, about one mm in diameter, outlined the emission area (Figure 35a). At the center of this ring were 4 or 5 bright oval spots, overlapping each other, which appeared to be the points of impingement of the electron beams from a corresponding number of emitting areas on the stylus tip (Figure 35b). Unfortunately, divergence of the beams made it difficult to say exactly how many emitting pins (or emitting areas on a single pin) the spots represented. However, since one would expect little beam spreading over such a short distance, it seems safe to assume that the spots were produced by no more than 4 or 5 pins. The results thus suggest that the tungsten pins are capable of carrying

(a)



(b)

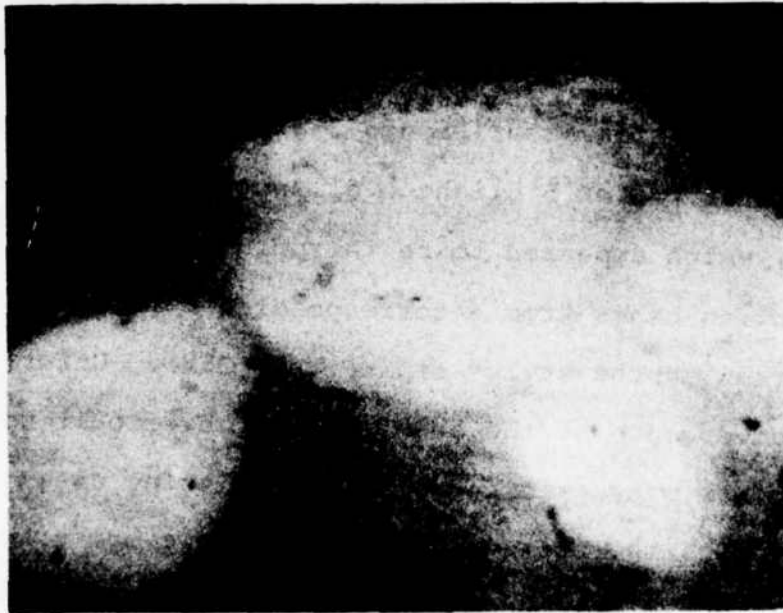


Figure V-35. Post-Emission Appearance of Anode in Test MM-20, (a) X70, (b) X945.

much larger currents than would be indicated by calculating the average current per pin under the UF anode.

Test MM-21 was even more definitive in this respect, since the number of exposed pins was even smaller (Figure V-36). Although seven pins were exposed at the tip of the stylus, the two center pins were at least twice as tall as the others and probably produced the majority of the emission current. Since the total current for the cathode reached 28  $\mu\text{A}$ , it left little doubt that each pin was capable of producing at least 4  $\mu\text{A}$  of emission current. If one assumes that the two center pins were producing all of the current, the emission capacity increases to 14  $\mu\text{A}$  per pin. Post-emission SEM examination of the cathode revealed no discernable change in the appearance of the pins (Figure V-37). Unfortunately, the cathode was dropped and the pins destroyed before it could be replaced in the fixture for further testing.

The most significant result of tests MM-20 and MM-21 was confirmation of the fact that the tungsten pins can produce several microamps of emission current without damage. This was not apparent from the tests with the UF anode, and permitted further interpretation of that test data with regard to emission uniformity.

(a)

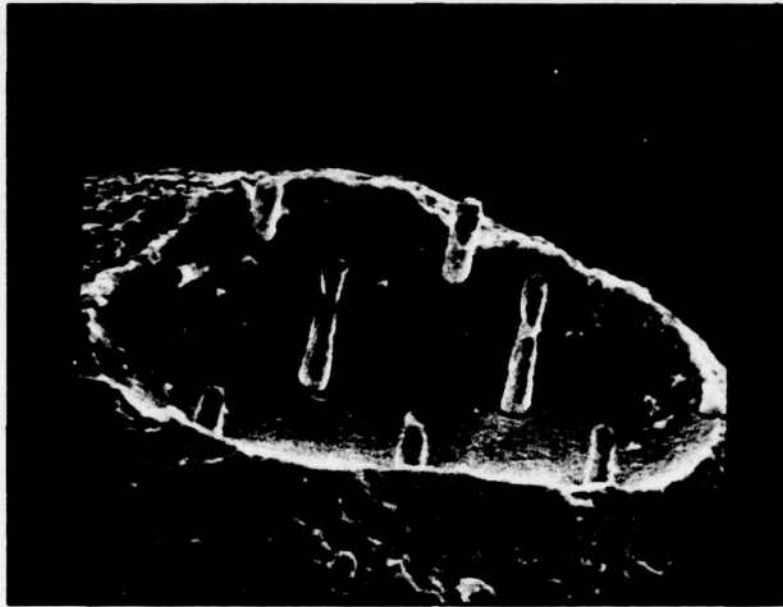


Figure V-36. View of the Exposed Pin at the Tip of the Stylus Cathode Used in Test MM-21, X4000.

(b)

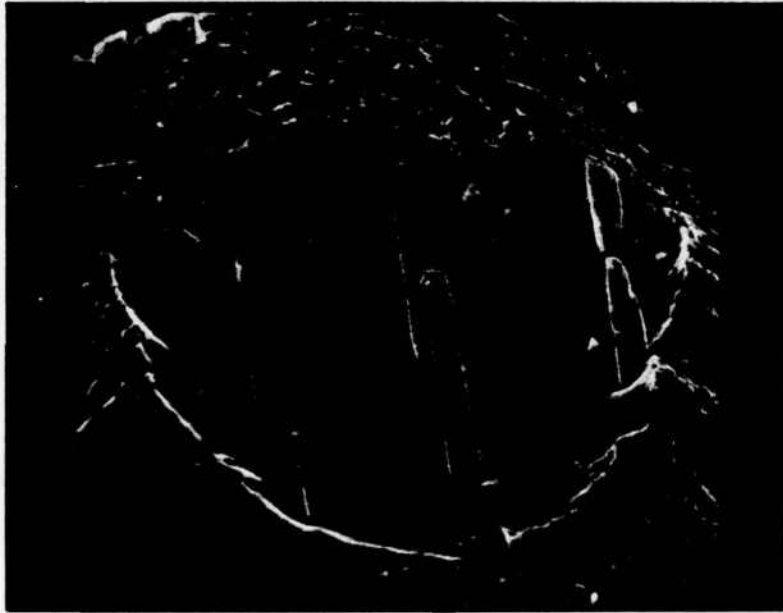


Figure V-37. Post-Emission Appearance of the Pins on Cathode MM-21, X4250.

## 2. Gun Geometry

The tests of the stylus cathodes in the gun geometry produced several interesting results. A schematic of the anode/cathode geometry for MM-24 is shown in Figure V-38. The extractor was constructed from a piece of 0.003 inch (75  $\mu\text{m}$ ) stainless steel shim stock, with a 0.025 inch hole drilled through the center, spot-welded to a 1/8 inch-thick stainless steel plate. The collector, consisting of a flat metal plate located about 1 cm above the extractor, was floated at +300 volts with respect to the extractor. The cathode was the same one used for test MM-20, repolished and re-etched to expose approximately 50 cylindrical pins, ranging in height from 15  $\mu\text{m}$  at the center to 2  $\mu\text{m}$  near the edge, in a shallow depression at the tip of the stylus (Figure V-39).

The cathode produced a total of 100  $\mu\text{A}$  of emission current at 3.8 kV, with about 95% passing through the extractor to the collector. Although there had been no sign of arcs during the test, the cathode ceased to emit (some time during the weekend) after operating for at least 24 hours at the 100  $\mu\text{A}$  level. SEM examination revealed severe damage to the stylus tip, i.e., there were no pins remaining at all and the matrix itself was severely cracked

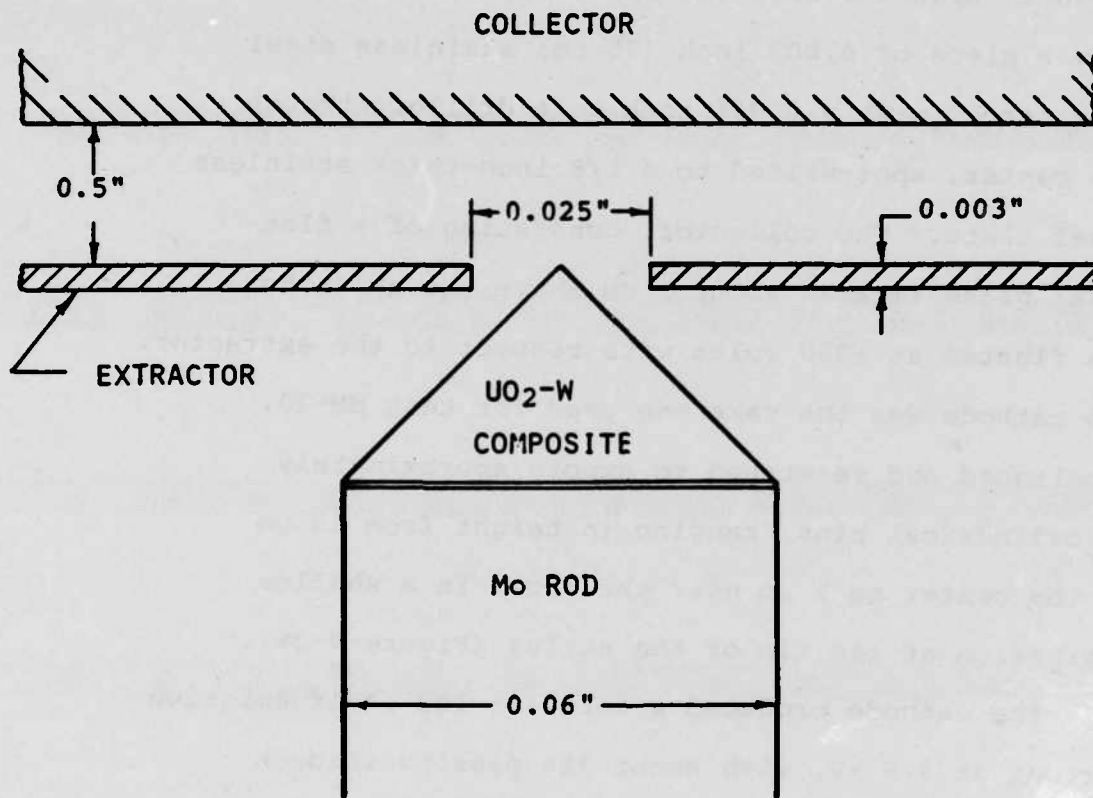


Figure V-38. Schematic Diagram of the Anode/Cathode Geometry Used in the Gun Test, MM-24.

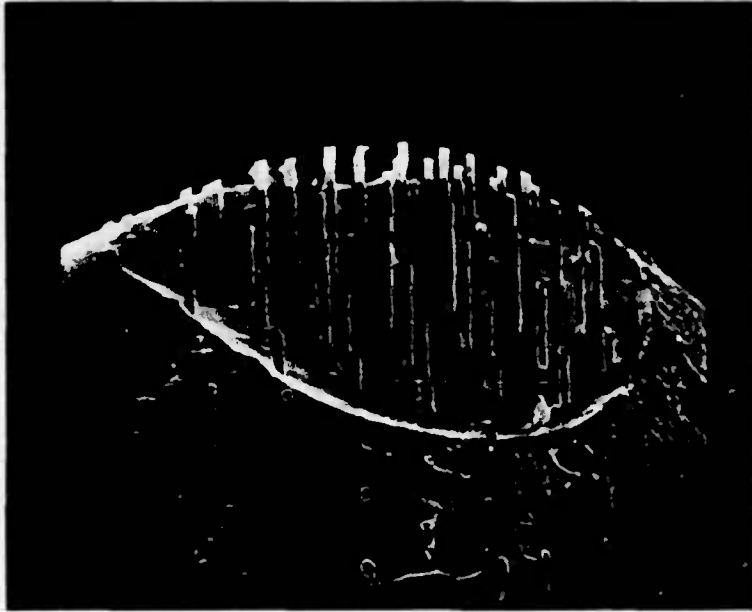


Figure V-39. View of the Exposed Pins at the Tip of the Stylus Cathode Used in Test MM-24, X1100.

and broken (Figure V-40). Breakdown in the BNC connectors had been a problem throughout the test, and at the time this was thought to have caused the pin damage. In view of other data, however, it would appear that the relatively high voltage may have been largely responsible.

The first of the two tests run in the RCA Gun was designed to further explore the effect of anode/cathode geometry on the ability to produce an electron beam from the stylus cathodes. A second objective was to try and produce an image of the beam on the phosphor screen.

The cathode for MM-28 consisted of a  $\text{UO}_2$ -W composite wafer, copper-brazed to a 1/16 inch (1.6 mm) diameter Mo rod and ground to a cone having a  $45^\circ$  half-angle. The cathode was etched to produce 10  $\mu\text{m}$ -long cylindrical pins covering the entire surface of the cone. It was mounted in the gun, as shown in Figure V-5, and secured with a setscrew. The tip was centered as nearly as possible in the 0.023 inch (0.58 mm) diameter aperture of the extractor anode with the sides of the cone approximately 0.002 inches (50  $\mu\text{m}$ ) from the lower surface of the aperture. This placed the tip slightly below the plane of the top surface

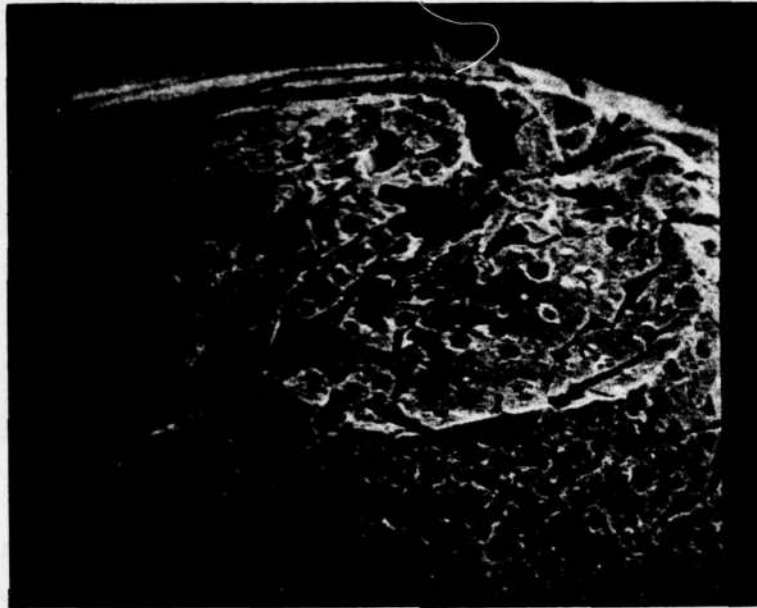


Figure V-40. Post-Emission Appearance of the Stylus  
Tip at the Conclusion of Test MM-24,  
X1000.

of the aperture. The interelectrode spacing was thus 0.011 to 0.012 inch (280 to 305  $\mu\text{m}$ ) at the tip, but less than 0.002 inch (50  $\mu\text{m}$ ) along the circumference of the cone which as in the plane of the lower surface of the aperture. The reason for the close spacing was to try and reduce the high extractor voltage that was needed for MM-24.

When the system pressure had been reduced to the mid- $10^{-8}$  torr range, voltage was applied to the extractor. The voltage was increased until the cathode began to produce emission current of about one  $\mu\text{A}$  at 1.5 kV. The current was then increased gradually over the next 140 hours to 40  $\mu\text{A}$  @ 2.1 kV. The lenses were shorted together during this initial conditioning period, and were floated at +300 volts above the extractor voltage. A microammeter placed in the lens circuit when the emission current reached 60  $\mu\text{A}$  indicated that less than two percent of the current was passing through the aperture.

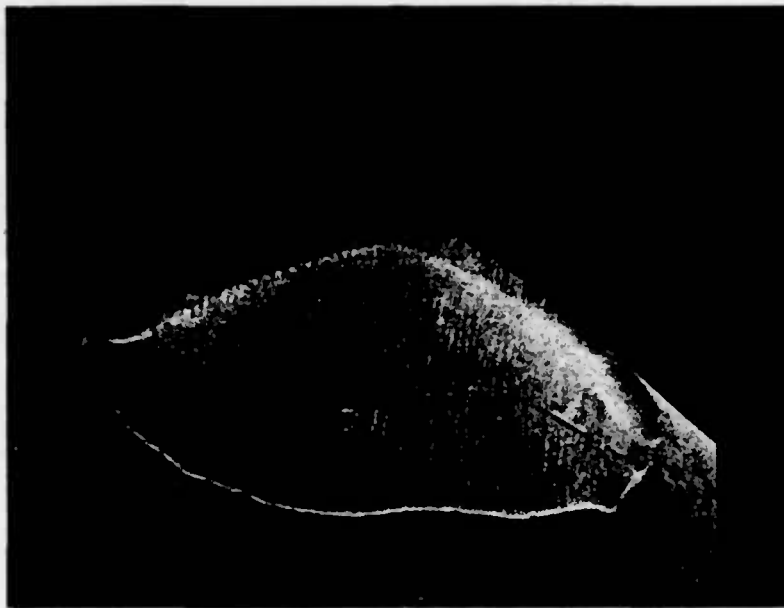
Overnight, however, the ion pump shut off (for reasons unknown). The next morning the system pressure had increased to more than  $10^{-6}$  torr and emission current had decreased slightly to 55  $\mu\text{A}$ . The voltage was turned off, and when the ion pump was restarted the pressure quickly dropped to its former level. When voltage was again applied to the extractor, the

beam current was over 15  $\mu$ A, more than 20 percent of the total current!

After determining the proper voltages to apply to the focusing lenses (these are shown on the schematic in Figure V-5), an image was obtained on the screen. By varying the lens voltages, the image could be focused to a spot or defocused to fill the screen. When the image was enlarged to a circle 2 cm in diameter, individual areas several millimeters in diameter could be observed to flicker and change rapidly in intensity. At one point the entire top half of the image disappeared for several hours; at other times one or more areas would become very bright for several minutes and then fade again.

A second test (MM-29), using a similar cathode geometry (Figure V-41), gave comparable results. The magnified image, (Figure V-42), in which the bright areas seemed to correspond to individual pins or groups of pins, was very similar to that observed in the previous test. The same changes in intensity were apparent, the bright areas sometimes flickering rapidly on and off, sometimes remaining stable for several hours at a time. Both the intensity of the areas and the rate of flickering increased as the extractor voltage was increased.

(a)



(b)

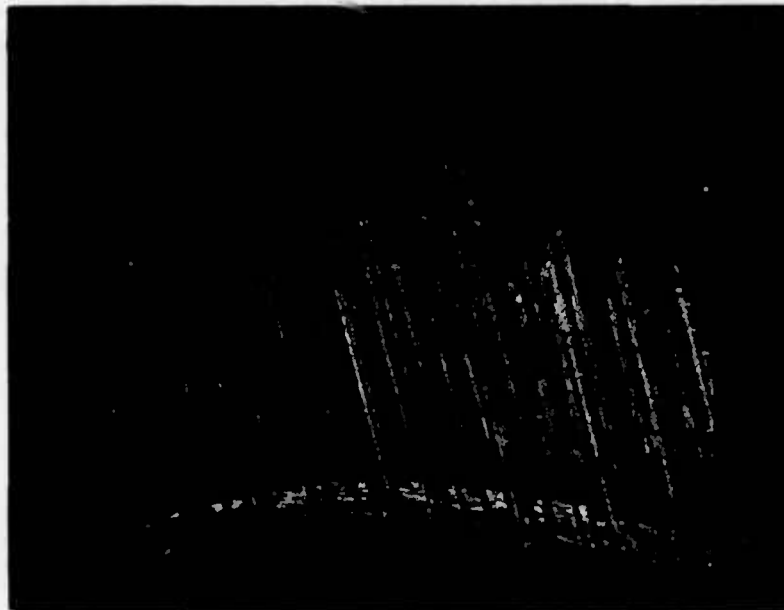


Figure V-41. View of the Exposed Pins at the Tip of the Stylus Cathode Used in Test MM-29, (a) X450, (b) X3250.



**Figure V-42. Image of the Defocused Electron Beam  
on the Phosphor Screen of the RCA  
Gun Used in Tests MM-28 and MM-29.**

As in MM-28, the intensity of the image was inversely proportional to the extractor current. In both cases, this was apparently a result of having exposed pins on the side of the cone which were closer to the edge of the aperture than those at the tip. Since the cathode was being operated in a current-limited mode, when the extractor current increased due to the contribution from the side pins, the extractor voltage decreased. This resulted in a decrease in the field at the tip of the stylus and caused the pins at the tip to stop emitting. When the voltage was turned off for several minutes, the side pins evidently became contaminated by the residual gas in the system, increasing their work function and causing a corresponding decrease in the emission level. This permitted an increase in voltage sufficient to activate the pins at the tip, which contributed primarily to the electron beam.

SEM examination of the two cathodes revealed similar damage. In both cases, most of the pin damage occurred at the tip of the cone, with perhaps 90 percent of the tip pins being destroyed on MM-29 (Figure V-43). Fiber growth at the tip of MM-28 was poor to begin with, and most of the damage there appeared to be mechanical rather than electrical. Pin damage along

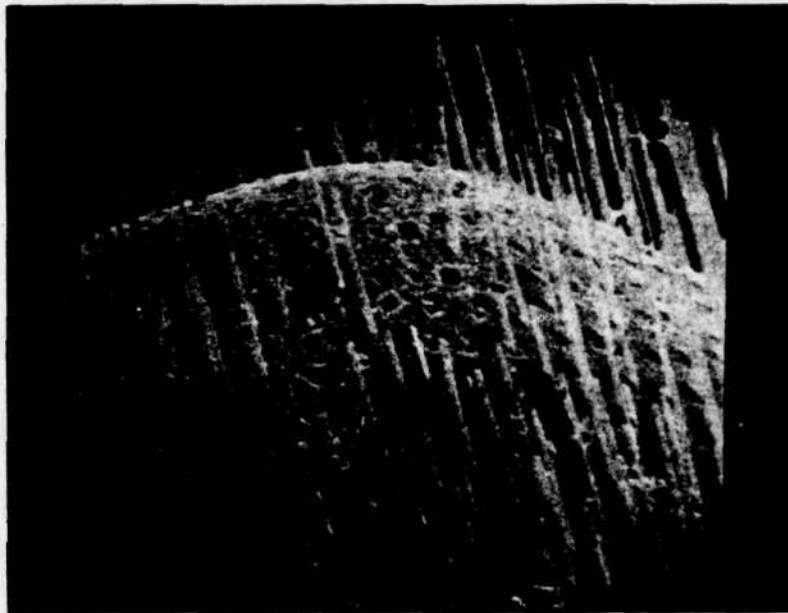


Figure V-43. Post-Emission Damage on the Stylus Tip Used in Test MM-29, X1800.

the sides of both cathodes, however, was much less than expected, although some evidence of arcing could be seen.

The tests with the gun geometry also contributed some important information. Test MM-24 demonstrated that it was relatively easy to construct a field emission cathode which could place the majority of its emission current into a beam, provided a suitable anode geometry was used. The tests with the RCA Gun indicated that the placement of the stylus-shaped cathode in relation to the extractor electrode was fairly critical with regard to the amount of current that would pass through the aperture. The observation of the image of the electron beam on the phosphor screen clearly demonstrated the dynamic nature of the emission from the composite cathodes. Furthermore, since the current flow to the extractor in all of the tests was far too little to cause any heating, and since pin damage was rather severe on all of the cathodes, the test results suggest that ions produced by heating and subsequent out-gassing of the anode are not a significant cause of pin failure, at least for current densities of less than a  $\text{mA}/\text{cm}^2$  of anode surface.

#### H. TESTS IN THE SEMICON VACUUM TUBES

The main objective of the tests in the Semicon tubes was to investigate the problems associated with operating a field emission cathode in a vacuum environment similar to that required by conventional thermionic cathodes. Cathodes of various geometries were tested: cones, truncated cones, chisels, right circular cylinders, etc. All were machined from composite wafers 0.020 inches to 0.040 inches in thickness, copper brazed to 1/16 inch or 1/8 inch diameter Mo or 410 stainless steel rods.

The cathodes were activated in the same manner as those tested in the fixed spacing diode. Buffer resistors were normally used in place of the TLD, starting at 1000 M $\Omega$  for initial activation and decreasing in size, as the current increased, to keep the required power supply voltage below 10 kV. Because of the smaller emitting area available, the current was increased at a slower rate than for the large-area cathodes.

Initially, the aim was to condition the cathodes up to emission currents of 3 to 5 mA, seal the tubes, and then operate them at lower currents to extend the cathode life. An emission current of 3 mA ( $\sim 100$  mA/cm<sup>2</sup>) was achieved with one of the cylindrical cathodes, but an interelectrode arc(s)

damaged it before it could be sealed. Most of the sharply pointed cone-shaped cathodes began to exhibit symptoms of pin damage (rising voltage, arcs, etc.) at emission currents of about one milliamper. However, this is not so surprising when one considers the relatively small number of pins at the tip. For example, if as many as 500 pins are emitting equally (and the number is likely to be much smaller) a current of one milliamper corresponds to an array current density of  $20 \text{ A/cm}^2$ .

The design of the Semicon tubes also limited the maximum emission current to a great extent. At power levels near 2 watts (1 mA @ 2 kV) the anode would be heated bright red (Figure V-44). This heat would produce considerable thermal expansion of the relatively long Mo wires to which the anode was welded, resulting in a steady increase in the interelectrode spacing as the power level rose. The current would then decrease slightly, the voltage would rise further, and eventually a new equilibrium interelectrode spacing would be reached. The greater the power input, the more extreme this effect became until, at 5 or 6 watts, a point was reached where further current increases became impossible. An increase in the voltage caused such an increase in the interelectrode spacing that the



**Figure V-44. Photograph of One of the Semicon Tubes in Operation, Illustrating the Degree of Anode Heating Produced by a Total Emission Current of One Millimapere at 2 kV.**

macroscopic field, and thus the emission current, remained constant or decreased. The higher voltages associated with the spacing increases also spurred the rate of pin damage, as evidenced by more interelectrode arcing and abrupt decreases in the emission current.

An interesting effect noted in some of the tests of the cone-shaped cathodes is worth mentioning. When operating at emission levels of 1 mA or more, the cathodes were frequently observed in the dark to check for interelectrode arcs. Occasionally however, instead of arcing, portions of the cathode tip could be seen glowing bright orange or yellow. This effect was not instantaneous, sometimes lasting 10 or 15 minutes before gradually fading back to the blue glow normally present at or near the anode at higher emission levels. The current would frequently increase by 20 percent or more during these periods and then return to its previous level as the color faded.

After each of the cathodes had been conditioned up to a point where the emission level began to degrade, it was turned off and the tube sealed. This was accomplished by carefully outgassing the tube stem with a torch and then heating the stem until it softened and pinched off. The sealing operation could be accomplished without the pressure in the ion pump going above mid- $10^{-7}$  torr. Unfortunately, only one

of the cathodes operated for more than a few minutes after the tube had been sealed. One of the chisel-shaped cathodes produced several hundred microamps in a sealed tube and was operated for several hours at a time over a ten day period with little or no variation in the current.

There is little doubt that high pressure in the tube was the cause of the failure of the other cathodes, but efforts to reduce the pressure met with little success. These efforts included more thorough outgassing of the stem prior to sealing the tube, higher temperature and longer bake out periods, and inclusion of barium getters which were flashed after the tube was sealed. The one success mentioned above apparently benefited from all of these measures, but there were several failures subsequent to that test.

Discussions with personnel experienced in tube manufacture indicate that bake out temperatures of 450°C or higher are necessary to sufficiently outgas the tube walls and metal parts prior to sealing the tube. Unfortunately, the soft glass of which these tubes were constructed would not permit such a high temperature bake out; and the tube design would not permit rf heating of the metal parts, since the cathode support would expand and press the exposed

pins of the cathode against the anode.

The relative lack of success with the Semicon tubes should not rule out use of field emitters in sealed tubes. The pressure in the sealed Semicon tubes was quite likely  $10^{-4}$  torr or greater to cause such a quick shut-down of the cathodes. Experiments have shown that the cathodes will operate quite well at pressures as high as  $10^{-5}$  torr, and MM-10 ran for 400 hours at  $1 \text{ A/cm}^2$  at  $10^{-7}$  torr. However, even if suitable vacuum processing were available in these particular tubes (to yield pressures of  $10^{-7}$  torr) the inability to maintain constant interelectrode gaps limits the usefulness of the tubes in evaluating the field emission performance.

## I. PIN FAILURE MECHANISM

The available evidence (from post-emission SEM examination and from observation in the SEMICON tubes and the RCA gun) points to a pin failure mechanism similar to that observed by Dyke and his co-workers<sup>14,15</sup> for single-pin emitters. When the current density at one of the tungsten pin tips reached a certain critical level, on the order of  $10^7$ - $10^8$  A/cm<sup>2</sup>, resistive heating caused the temperature of the tip (or a portion of it) to approach the melting point. At this point, though the exact sequence of events is still not completely understood, the tip was apparently disrupted by a vacuum arc. The damage resulting from the arc appeared to range anywhere from fusion of only the pin tip to explosive vaporization of the entire pin and subsequent destruction of neighboring pins. An example of the first case is shown in Figure V-22b, while Figures V-19b and V-33 graphically illustrate the other extreme.

There is also ample evidence that the pins can operate at extremely high temperatures without initiating an arc. Note that several of the tungsten pins illustrated in Figures V-22b became hot enough to melt the UO<sub>2</sub> matrix at the base of the pin (m.p. of UO<sub>2</sub> is  $\sim 2800^\circ\text{C}$ ), while the pin tips are only slightly rounded. In Figure V-31b,

the only change in the pin tips is loss of the platinum coating, while both the  $\text{UO}_2$  matrix and the platinum coating are melted away from the base of the pins.

It is still not absolutely clear why pin damage seemed to vary to such a large extent over the array. Of course in many cases it was impossible to determine from post-emission SEM examination whether the pins melted down individually or were destroyed as a group, perhaps by an arc initiated at a single pin (Figure V-19b). However, installation of the TLD, coupled with reduced interelectrode spacings (hence lower voltages), did seem to reduce the damage caused by individual arcs. Instead of the large melted craters observed in the early tests (Figure V-16), damage was usually limited to melting of the pins or pin tips.

There are a variety of ways in which the emission current density at an individual pin tip might exceed the critical level. For example, for pin tips having  $200 \text{ \AA}$  radii, assuming uniform emission from the apex of the tip to a polar angle,  $\theta$ , of  $30^\circ$ , the effective emitting area per pin would be  $\sim 3 \times 10^{-12} \text{ cm}^2$ . If emission at any given instant was limited to no more than 0.2% of the pins under the UF anode ( $\sim 300$  pins in an array of  $10^7$  pins/cm<sup>2</sup>) the average current per pin would be about 33  $\mu\text{A}$ , and the

current density per pin would exceed  $10^7$  A/cm<sup>2</sup> at an emission current of 10 mA ( $\sim 0.5$  A/cm<sup>2</sup>).

Such non-uniform emission from an array might be due to variations in pin height, pin tip radius, or pin separation distance. However, it seems unlikely that even a combination of these factors could produce such a large degree of current variation across the array. A more likely source of the high current density is an extremely small emitting area on the pin tips. These small emitting areas could be due to microprotrusions or lattice steps, having small effective radii, or perhaps to emission through "holes" in an adsorbed oxygen layer on the pin tips.

Another possible source of reduced emitting area is the distortion of the field at the pin tip, due both to the presence of neighboring pins and to use of a planar anode. These two factors might cause a concentration of the field at the apex of the tip, resulting in a much more rapid decrease in emission current as a function of  $\theta$  than is observed for single pin geometries with concentric spherical anodes. For example, if the value of  $\theta$  in equation (12) is  $10^\circ$ , the effective emitting area for a tip with a 200 Å radius is only  $\sim 4 \times 10^{-13}$  cm<sup>2</sup>, requiring only 4 μA per pin to produce a critical current density. However, at a total current of 10 mA, this would still mean that only 2500 pins, or about one percent

of the pins under the UF anode, were producing emission current. (Note that an emission current of 4  $\mu\text{A}$  per pin from the cathode in Test MM-6 would have been equivalent to a macroscopic current density of  $80 \text{ A/cm}^2$ .)

Calculations based on the V-I data tended to support the hypothesis that the emitting areas were extremely small. However, it is unlikely that they were small as those listed in Table V-III; such small values would mean current densities several orders of magnitude greater than the critical level of  $10^7$ - $10^8 \text{ A/cm}^2$  mentioned earlier. On the other hand, even if the largest of the emitting areas listed is increased by a factor of 100, to  $5 \times 10^{-9} \text{ cm}^2$ , then at a total current of 10 mA (assuming that the maximum current per pin is 4  $\mu\text{A}$ ), the emitting area per pin would still be only  $2 \times 10^{-12} \text{ cm}^2$  and the current density would be  $2 \times 10^6 \text{ A/cm}^2$ , very near the critical level. Note, too, that most of the values calculated for the total emitting area were one to two orders of magnitude less than the example used above.

There was also evidence of non-uniform emission from the tungsten pin arrays. The most obvious indication was the fact that no cathode produced an average current per pin of greater than 250 nA (and most were much less), yet test MM-21 clearly demonstrated that each pin could

produce at least 4  $\mu\text{A}$  of emission current with no damage. The changing intensity of the images observed in the RCA gun also suggested considerable variation in emission current over the surface of the cathode, over relatively short time periods.

Thus, though more fundamental studies in the field emission microscope will probably be necessary to determine the exact nature of emission from the arrays, it was quite likely a combination of non-uniform emission and extremely small emitting area per pin which was ultimately responsible for most of the cathode failures observed in the emission tests.

Regardless of the cause(s) of pin failure, the results of the tests left little doubt that the combination of sharply pointed pins and small interelectrode spacings ( $\sim 50 \mu\text{m}$ ) greatly reduced the rate and degree of pin damage. In tests MM-6 and MM-10, this combination of parameters produced the largest total emitting area, the highest field enhancement (with one exception), and the least pin damage of any cathode tested in the UF anode. Although it is not surprising that the pointed pins would produce an increase in field enhancement, the reason for the larger total emitting area is still not clear. However, whether the increase was due to a

greater emitting area per pin or to more uniform emission from the array, the net result was a decrease in the required voltage; and this was almost certainly instrumental in reducing pin damage. If the total emitting area can be further increased by using even smaller interelectrode spacings and by producing more uniform (though sharply pointed) pin geometries, then current densities of  $10-50 \text{ A/cm}^2$  should be readily attainable.

## SECTION VI

### SUMMARY

The following summary describes the significant accomplishments of the research program, "Manufacturing Methods for the Production of Field Effect Electron Emitters from Oxide-Metal Composite Materials." The primary objective of this contract was to establish procedures for the production of melt grown oxide-metal composites and the evaluation of the field emission performance of prototype cathode structures. To accomplish this objective the research was divided into four tasks:

- 1) Procurement and Characterization of  $UO_2$  and Tungsten Powders
- 2) Development of Optimum Composite Growth Procedures
- 3) Development of Machining, Brazing, and Etching Techniques for Emitters
- 4) Evaluation of Field Emission Performance of Prototype Emitters.

At the outset of this program, the growth of the oxide-metal composites was restricted to sizes yielding ingots approximately 16 mm in diameter. Through the careful characterization of the urania powders and control of the solidification parameters the size of the ingots was increased to 25 and then to 32 mm in diameter. The steps

utilized in making the transition to the larger  $\text{UO}_2$ -W composite sizes are outlined. A variety of braze materials were evaluated during this contract and lastly, a number of improvements in the field emission performance of the cathode structures are described.

In the growth of the  $\text{UO}_2$ -W composites, the control of the oxygen-to-uranium (O/U) ratio of the oxide was the single most important variable because the solubility of tungsten in molten urania is stoichiometry dependent<sup>4</sup>. Consequently the powder characterization study was primarily concerned with establishing and maintaining the necessary O/U ratio during the preparation of the  $\text{UO}_2$ -W samples. Since the transition to larger diameter ingots required a sintering step, stoichiometry control during the solid state densification process was also required. As a result of this work, it was established that the reduction and controlled oxidation of the urania powders (yielding O/U ratios between 2.04 and 2.07) formed ideal starting materials for the preparation of the  $\text{UO}_2$ -W pellets. Some of the problems associated with measuring the O/U ratios were reviewed and storage conditions suitable for maintaining controlled stoichiometry were established. Powder properties were related to the sintering behavior and, in general, nuclear grade

urania powders were suitable for the growth of the composites. Two samples of tungsten powder were evaluated and both performed adequately. During the solidification process the tungsten was completely dissolved in the molten oxide and no remanent of the initial particle characteristics remained.

Since the major objective of this contract work was to establish a routine and reproducible technique for the growth of the  $UO_2$ -W composites, a major effort was expended to this area. Procedures suitable for the routine production of  $UO_2$ -W ingots weighing up to 500 grams were established. With the large size samples a starting composition of  $UO_{2.05 \pm 0.02} + 6 \text{ w/o W}$  yielded ideal composite geometries. Sintered pellet densities between 9.5 and 10.5 gm/cc were required prior to internal melting because of the densification and alteration of the liquid-solid geometry occurring during the melting and solidification process. Since tungsten solubility is dependent on oxide stoichiometry a growth atmosphere consisting of CO-1 v/o  $CO_2$  resulting in an O/U ratio of molten urania of  $\sim 2.03$  was shown to be optimum. Using solidification rates between 2 and 4 cm/hr uniform fiber densities of 5 to 15 million per square centimeter were obtained. An attempt was made to minimize the cracking characteristics displayed by the  $UO_2$ -W composites; however, only

limited success was achieved. A few experiments performed during the last of the program showed that very slow growth rates (0.5 to 1.5 cm/hr) resulted in a significant decrease in fiber density ( $1.5$  to  $5 \times 10^6$  /  $\text{cm}^2$ ). In addition the crack geometry in these samples often yielded "flaw-free" wafer samples almost the entire diameter of the solidified zone. A flow sheet describing the fabrication of the sintered  $\text{UO}_2$ -W pellets and the procedures for the routine unidirectional solidification of  $\text{UO}_2$ -W ingots 25 mm in diameter and weighing 250 grams is presented.

The objective of the machining, brazing and etching studies was to develop techniques for the fabrication of suitable cathode structures for emission testing. The initial fabrication step was to slice wafer-shaped samples from the melted  $\text{UO}_2$ -W ingots using conventional ceramic machining methods, i.e. with diamond saws and grinding wheels. Rather intricate shapes for emission testing including stylus-type geometries were fabricated. A stylus with a tip radius less than 5  $\mu\text{m}$  was successfully made.

Prior to this study most of the previous  $\text{UO}_2$ -W field emitter cathode structures consisted of composite wafers copper brazed to a molybdenum support pin. The poor thermal expansion match of these materials often led to extensive cracking in the composite and a search

for a substrate-braze combination compatible with the composite was undertaken. Wetting studies indicated that nickel was a candidate braze material. A number of braze-substrate combinations were investigated and the most successful are briefly summarized below.

Composite wafers nickel-brazed to an alumina substrate formed a sound, well bonded sandwich structure and appeared potentially useful in applications where a mosaic of composite chips are needed. A nickel braze to a tungsten pin was successfully formed using a technique where the tungsten pin was lowered into the molten metal during the brazing operation.

The expansion behavior of the 400 series stainless steels are ideally suited for the  $UO_2$ -W composites and a number of emitter samples were fabricated using 410 SS with a copper braze. Most of the other metals, such as cobalt and titania, were discarded because of a variety of problems arising during these brazing tests.

Chemical etchants developed in previous work were employed to point the tungsten pins during cathode fabrication. Ion milling was tested as an alternate method to shape the pin tips and found useful to form a series of exposed pin geometries. The milling parameters and resulting pin tip shapes are described in Section IV.

Prior to this program, most emission tests had been performed with large planar anodes. As a result, emission from the cathodes was edge-dominated and little was known of the actual macroscopic current density (emission current per unit of cathode area) capability of the cathodes. At the beginning of the current contract, tests were made with an anode (UF anode) which produced a uniform electric field at the surface of the cathode, thus permitting a more accurate estimate of current density. A number of the tests with this anode to determine optimum cathode/pin geometry are described in detail and the results summarized in a table. The results indicated that sharply pointed pins and small interelectrode spacings ( $\sim 50 \mu\text{m}$ ) produced the best emitter performance. Two cathodes which contained the above combination of parameters each achieved an emission current density in excess of  $1 \text{ A/cm}^2$  and showed the least pin damage of any cathode tested. Calculations based on V-I data showed that these two cathodes had the highest total emitting area, the highest field enhancement (with one exception) and, as a result, the lowest required voltage of all cathodes tested with the UF anode.

Tests with the UF anode also suggested that array density had a second-order effect on emitter performance, at least within the range of array densities available

for these tests ( $1.6 \times 10^6 - 2 \times 10^7 \text{ cm}^{-2}$ ). However, results of two of the tests revealed that emission from the pins was enhanced if some of the neighboring pins were absent or were removed. The effect of pin height on performance was inconclusive. Surprisingly, various attempts to improve emission performance by heat treating or ion-milling the cathodes to improve the uniformity of pin height and tip shape resulted in lower total emitting areas and increased pin damage.

Tests with stylus-shaped cathodes in a diode geometry, with as few as 7 to 20 etched pins at the tip, indicated that individual pins had a much higher emission current capacity, on the order of 4-14  $\mu\text{A}$  per pin, than was indicated by calculating the maximum average current per pin in the tests with the UF anode (250 nA). Tests of similar cathodes in a gun geometry successfully demonstrated that, with proper selection of cathode/extractor geometry, the majority of the field emitted electrons would pass through the extractor aperture and could be focussed into a beam.

Efforts to produce an operating field emission diode in a sealed tube are also discussed. Only limited success was achieved using the tubes, primarily

because of a tube design which did not allow sufficient bake out and degasing. The consequence was that the necessary vacuum could not be maintained after the tube was sealed. A further deficiency in the tubes (which were originally designed to test thermionic cathodes) was that long anode supporting wires caused drastic changes in interelectrode spacing, due to thermal expansion, at power levels of one watt or more.

Based on the results of all of the tests, the most likely pin failure mechanism is described and some of the possible causes of premature pin failure are reviewed.

## APPENDIX A

### Compilation of the $UO_2$ -W Composite Growth Experiments

The results of the  $UO_2$ -W unidirectional solidification runs performed during this program are tabulated in Table VII-I. For convenience, selected data from this compilation has been compared in small tables in Section III. The following list of numbered comments is used in Table VII-I to facilitate describing the specific experiments and results.

#### Comment Codes

1. Upper and lower susceptors used (spacing in mm)
2. Banded
3. Good Growth (avg. fiber density in  $10^6$  pins/cm<sup>2</sup>)
4. Irregular growth (avg. fiber density of good areas in  $10^6$  pins/cm<sup>2</sup>)
5. No growth
6. Two molten zones established
7. No stable molten zone established
8. "Blue" phase ( $U_xWO_3$ ) present
9. O/U high, sintered with LBH-5
10. Sintered in  $H_2/N_2$  atmosphere
11. Sintered in  $CO_2$  atmosphere
12. Growth atmosphere CO-0.5 v/o  $CO_2$
13. 1.5 inch diameter pellets

14. Susceptor raised slowly to prevent cracking
15. Expansion gaps (size in mm) cut to lessen cracking
16. Circumferential cracking occurred

Table VII-I. Results of UO<sub>2</sub>-W Solidification Experiments.

Run LBH-	Starting O/U	Composition Wt. % W	Control O/U	Sample Density(g/cc) green	Sample Density(g/cc) fired	Growth Rate (cm/hr)	Power kv	Settings A	Comments
1	2.04	6	2.01	4.5	9.1	2.47	5.6	0.85	1(25),2
2	2.04	6	2.01	4.7	9.9	2.24	5.7	0.85	1(25),2
3	2.07	6	2.01	4.7	9.2	3.40	3.7	0.70	3(7),6
4	2.07	6	2.01	4.7	9.3	2.77	4.6	0.92	3(10),6
5	2.20	12	2.09	4.3	9.0	2.74	4.0	0.95	5,7,8
5A	2.07	6	2.09	4.6	9.2	2.80	4.7	0.95	3(12),8,9
6	2.07	6	2.01	4.6	9.4	2.87	4.8	0.95	3(25),8,15(0.03x5)
7	2.07	4	2.01	3.8	8.8	6.00	4.7	0.95	4(30)
8A	2.07	6	2.01	4.2	8.0	2.67	4.6	0.95	5,7
8B	2.07	6	2.01	4.4	8.3	2.67	4.8	0.95	4(Not Determined)7
8C	2.07	6	2.01	4.6	8.6	3.20	4.5	0.95	3(3),6
9	2.07	6	2.01	4.6	8.5	2.95	5.1	1.00	3(10),8,15(1x3)
10A	2.07	6	2.01	4.7	8.5	2.67	5.2	1.00	4(30),8
10B	2.07	4	2.01	4.6	8.4	2.74	5.1	1.00	4(6)
11	2.07	6	2.01	4.6	10.1	3.18	5.5	1.05	3(Not Determined)13
12	2.07	6	2.01	4.6	10.1	3.33	5.8	1.10	3(Not Determined)13

Table VII-I. (continued)

Run LBH-	Starting O/U	Composition Ht. % H	Control O/U	Sample Density(g/cc) green	Sample Density(g/cc) fired	Growth Rate (cm/hr)	Power kV	Settings A	Comments
13	2.07	6	2.01	4.5	9.4	3.50	5.0	1.00	3(8)
14	2.07	6	2.01	4.7	9.6	2.00	6.0	0.90	1(25),2
15A	2.07	6	2.01	4.7	9.6	3.00	5.0	1.00	3(12)
15B	2.07	6	2.01	4.7	9.5	3.00	4.7	1.00	3(10),14
16	2.07	6	2.00	4.7	8.7	2.31	5.0	1.00	5,10
17	2.07	6	2.01	4.6	9.9	3.14	5.3	0.59	1(36),2
18	2.07	6	2.01	4.7	9.8	2.22	4.8	1.00	3(Not Determined)
19	2.07	6	2.10	4.7	9.2	2.00	4.6	1.00	3(Not Determined)11
20	2.07	6	2.01	4.8	10.3	1.50	5.2	1.00	3(5),12,16
21	2.07	6	2.01	4.7	9.8	0.50	5.0	1.00	3(1,6),16

### REFERENCES

1. A.T. Chapman, G.W. Clark, and D.E. Hendrix, "UO<sub>2</sub>-W Cermets Produced by Unidirectional Solidification," J. Am. Cer. Soc., (53) 60-61 (1970).
2. A.T. Chapman et al., "Melt-Grown Oxide-Metal Composites," Technical Reports 1-6, sponsored by ARPA, Contract Numbers DAAH01-70-C-1157 and DAAH01-71-C-1046, ARPA Order Number 1637, 1971-1973.
3. A.T. Chapman, "Phase Relations for Cubic UO<sub>2+x</sub> Between 1000°C and 2900°C," Paper Presented at the Amer. Cer. Soc. 29th Pacific Coast Regional Meeting, Oct., Nov., 1976.
4. R.E. Latta, R.E. Fryxell, "Determination of Solidus-Liquidus Temperatures in the UO<sub>2+x</sub> System (-0.50 x 0.20)," Journal of Nuclear Materials (35) 195-210 (1970).
5. E.W. Mueller, Z. Phys., 108, 668 (1938).
6. R. Haefer, Z. Phys. 116, 604 (1940).
7. J.A. Becker, Bell Syst. Tech. J., 30, 907 (1951).
8. M. Drechsler and E. Henkel, Z. Angew. Phys., 6, 341 (1954).
9. W.P. Dyke, et al., J. Appl. Phys., 24, 570 (1953).
10. R. Gomer, Field Emission and Field Ionization, Harvard University Press, Cambridge, Mass., 1961, Chapter 2, p. 45.
11. J.D. Levine, RCA Rev. (Radio Corp. Am.), 32, 144 (1971).
12. W.L. Ohlinger, "The Effect of Diode and Array Geometrical Parameters on Performance of High Field Electron Emitters Formed From Unidirectionally Solidified Uranium Dioxide-Tungsten Composites", Ph.D. Dissertation, School of Ceramic Engineering, Georgia Institute of Technology, August, 1977.

13. D. Alpert, D.A. Lee, E.M. Lyman, and H.E. Tomaschke,  
J. of Vac. Sci. & Tech., 1, 35 (1964).
14. W.P. Dyke, J.K. Trolan, E.E. Martin, and J.P. Barbour,  
Phys. Rev., 91, 1043 (1953).
15. W.W. Dolan, W.P. Dyke, and J.K. Trolan, Phys. Rev.,  
91, 1054 (1953).

**END**

**FILMED**

1-85

**DTIC**